

SAPIENZA Università di Roma

PhD dissertation in Earth Sciences

SSD: GEO/04

**Remote sensing applications for the
assessment of the geomorphic
response of fluvial systems to the
Holocene Climate Changes**

PhD candidate:
Giulia Iacobucci

Supervisor:
Prof. Francesco Troiani

XXXIII ciclo

Department of Earth Sciences
15th March 2021



SAPIENZA
UNIVERSITÀ DI ROMA

Revised by:

Prof. Domenico Capolongo

Dipartimento di Scienze della Terra e Geoambientali

Università degli Studi di Bari "Aldo Moro"

Bari (Italy)

Prof. Jorge Pedro Galve Arnedo

Departamento de Geodinámica

Universidad de Granada

Granada (Spain)

Statement of Copyright

The copyright to the material within this thesis belongs to the author. No quotation or data from it should be published without the author's prior consent and any information derived from it should be acknowledged.

© Giulia Iacobucci. All rights reserved.
Author's email: giulia.iacobucci@uniroma1.it

Index

Abstract	3
Plain language summary	5
Graphical abstract	6
List of figures	7
List of tables	10
Forewords	11
1. Introduction	13
2. Holocene (“rapid”) Climate Changes	15
2.1 Fluvial response to the Holocene Climate Changes (HCC)	17
2.2 The Early River Civilizations	20
3. The Lower Mesopotamian Plain	24
3.1 Geological setting	25
3.2 Holocene and present climate of the MP	28
3.3 Geomorphology of the MP	33
4. Materials	40
4.1 Landsat 8	40
4.2 COSMO-SkyMed Product (©ASI - Agenzia Spaziale Italiana)	42
4.3 ALOS DEM	47
4.4 ASTER DEM	49
5. Methods	51
5.1 Topographic analysis of the micro-relief	52
5.2 Multispectral satellite imagery analysis	55
5.3 DEM generation from COSMO-SkyMed© SPOT imagery	60
6. Results	64
6.1 The avulsion processes	66
6.1.1 Preliminary inspection and topographic analysis of the micro-relief	67
6.1.2 Multispectral satellite imagery analysis	72
6.2 Geomorphological mapping at Tell Zurghul archaeological site	80
7. Discussion	86
7.1 Fluvial avulsion processes in lowland areas	86
7.2 Geomorphology of the area at Tell Zurghul archaeological site	89
8. Conclusions	92
9. Implications	94
Acknowledgements	95
Appendix	96

Holocene Climate Changes in the Mediterranean area: an example of traditional, field-based study in the northern Apennines.....	96
References.....	100

Abstract

The general goal of this thesis is the identification and description of the geomorphological responses of the fluvial system to the Holocene Climate Changes, proposing a multi-sensor remote sensing approach. In particular, the specific aim of this work is the improvement of the present knowledge on the Holocene and historical morphodynamics of the Lower Mesopotamian waterscape, especially on the paleo-hydrology of the ancient Tigris-Euphrates fluvial system, focusing on the specific process in the dynamics of the waterscapes which plays a key role in the drainage network evolution in lowland areas. Crevasse splays represent significant geomorphological features for understanding the fluvial morphodynamics in lowland areas where avulsion processes prevail.

The southern Mesopotamian Plain is the area where the ancient State of Lagash developed between the prehistoric Ubaid Period (c. 5200 - c. 3500 BC) and the late Parthian era (247 BC - AD 244), representing an ideal case study, where the Italian Archaeological Mission has been recently carried on extensive field-works at Tell Zurghul archaeological site. Here, an interdisciplinary approach, combining field surveys and geomorphological mapping through remote sensing techniques, has been applied for analysing the function and role of the waterscape on the early civilization. Indeed, the geomorphological analysis through a remote sensing approach and the archaeological surveys are both essential for the reconstruction of a complex environmental system, where landforms due to different morphogenetic processes occur, related to the presence of a wide fluvial-deltaic paleo-system and early human societies. The main aim of the focus on this archaeological site is to contribute to the reconstruction of the surrounding waterscape and know more about waterscape-human interactions during the Holocene.

The question of human-waterscape relationship worldwide has been and still is a central topic in geomorphological, environmental, and archaeological research. During the Holocene, the Tigris-Euphrates river system, in the lower sector of the Mesopotamian Plain (Iraq), has been characterized by complex morphodynamics in response to both climate fluctuations and extensive construction of artificial canals, dug since the first human settlements belonging to the Early River Valley Civilizations. The Lower Mesopotamian Plain (LMP) coincides with the southern Tigris and Euphrates deltaic plain, developed starting since the mid Holocene. During the early Holocene, the sea-level rise caused a general and rapid northward shifting of the Persian Gulf shoreline: the maximum marine ingression reached the area where the present towns of Nasiriyah and Al-Amara are located about 6000 yrs BP; after which the widespread progradation of the Tigris and Euphrates delta system accounted for the southward shoreline regression up to the present position.

The development of a typical bird-foot delta guaranteed an amount of water indispensable for agriculture, cattle, settlements, and transport. Indeed, the high mobility of the channels and the frequent occurrence of avulsion processes (i.e., levees break and related crevasse splays formation) are the main features typically connected to a multi-channel system, guarantying the water supply through seasonal floods. In the area, the water management during the mid Holocene, digging an extensive network of canals and building several dams, can either improve the socio-economic conditions of a settlement or cause the end of another one.

Within a wide floodplain characterized by very low elevation ranges such as the LMP, a remote sensing, multi-sensor approach is a suitable method for identifying the main geomorphological features related to the fluvial avulsion processes, describing the associated morphogenetic processes. Optical and multispectral Landsat 8 satellite images have been processed for computing NDVI and Clay Ratio indices, as well as to extract the Regions of Interest (ROIs) focused on the main features that made up a crevasse splay (i.e., crevasse channel, crevasse levee and crevasse deposit). The spectral signatures from active and abandoned crevasse splays have been extracted and compared among

them, adopting four different methods of Supervised Classification. The analysis of the crevasse splays has been integrated with the investigation of the micro-topography leading to recognize the crevasse channels and levees, the upward convexity of the crevasse deposits and the distal or proximal position of the parent channel; the re-classification of different DEM sources, such as the optical AW3D30 and GDEM2 datasets with ground resolution of 1 arcsec (i.e., 30 m cell⁻¹), leads to highlighting the “above-floodplain” topographic configuration of these landforms.

The analysis here performed leads to investigating the entire Lower Mesopotamian Plain through both large and medium scale geomorphological investigation, identifying active and abandoned channels, discerning between active and abandoned avulsion processes and distinguishing crevasse channels, levees, and deposits. In like manner, human features are recognized, allowing the evaluation of human-environmental interactions.

Plain language summary

The area of the Mesopotamia is well-known as the cradle of the Early River Valley Civilizations during the Holocene (the current geological epoch began about 10,000 years ago), where the first human communities settled and arose on the banks of two amongst the world longest rivers: the Tigris and Euphrates. These two rivers are attractive locations for the early societies where a steady supply of drinking water and for growing crops, an easy way of communication and transport are potential resources. The relevant role of these rivers was so important that the systems of government were based on water management through flood control and irrigation. Thus, the digging of canals and the building of dams are essential for the socio-economic development and the political hegemony over a wide territory.

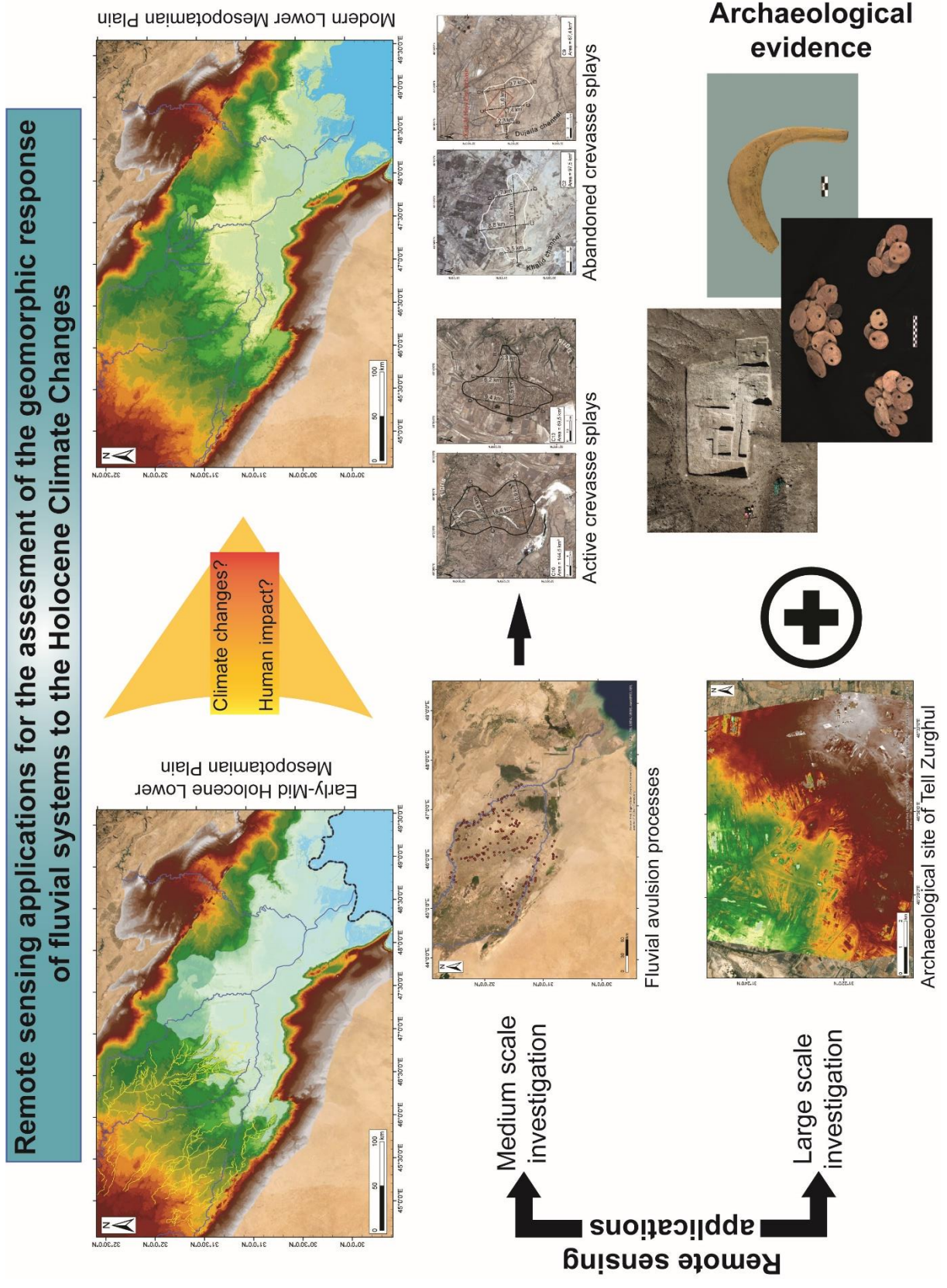
The Mesopotamian river landscape has been deeply influenced by climatic changes during the Holocene, which had an effect on the water supply, the shape and sinuosity of the watercourses, the occurrence of floods and river channels mobility (for example, the abandonment of a river channel for forming a new one), in addition to the influence on the human activities. Indeed, the occurrence of droughts caused an extensive water crisis, which triggered famines, epidemics, and warfare up to decline of entire societies. The study of the fluvial processes, either the still active at present days and the relict ones, along the Tigris and Euphrates Rivers and their recognition and mapping are potentially useful for archaeological surveys, the reconstruction of the Holocene environment and the study of the human-landscape interaction.

In the light of the wide extension of the southern sector of the Mesopotamia Plain of about several hundreds of thousands of square kilometres, the satellite imagery represents a potential method for investigating the area working from remote desks. Indeed, different kinds of images have been selected and processed for extracting information about the vegetation, the mineralogy of the deposits and the activity of specific fluvial landforms. Moreover, the availability of global digital altimetric datasets in a format named Digital Elevation Model (DEM) are helpful for visualizing and elaborating the elevation data of the area, to recognize possible fluvial landforms and processes and for the study of the anthropic features.

The investigation of a wide area like the southern sector of Mesopotamian Plain exclusively through the processing of several satellite data have been integrated with field data obtained at the archaeological site of Tell Zurghul (southern Iraq) by the Italian Archaeological Mission founded by the Sapienza University of Rome. Focusing on this archaeological site, the human-environmental interactions have been better evaluated also considering the effects of the Holocene climatic changes on the fluvial landscape.

The enhance of the knowledge about the human- and climatic-induced modifications over the environment is straightforwardly fundamental for understanding the resilience of the ancient societies, suggesting what our modern societies should do for preventing water shortage, agricultural crisis and climate migration.

Graphical abstract



List of figures

Figure 1 - The Iraqi territory subdivided into its main tectonic zones, modified from Sissakian 2013 (Figure A), and the study area corresponding to the LMP, detailed in Figure B with a satellite nadiral view from TerraColor satellite imagery.	26
Figure 2 - WorldClim 2.1 climate data for 1970-2000 with spatial resolution of 30 seconds (~1 km ²) and climate diagrams of Najaf, Nasiriyah and Shaibah (i.e., Basrah) from the Worldwide Bioclimatic Classification System (from Rivas-Martinez and Rivas-Saenz, 2017).	30
Figure 3 - The Mid-Holocene (about 6000 years ago) reconstructions according to the Beijing Climate Centre Climate System Model (BCC-CSM1.1) in figures A-B and the Community Climate System Model (CCSM4) in figures C-D, available on WorldClim 1.4 downscaled paleo-climate. The reconstructed mean annual precipitation (A-C) and the mean annual temperature (B-D) are quite similar between the BCC-CSM1.1 and CCSM4, as well as the reconstructed mean annual precipitation and temperature in figure 2.	32
Figure 4 - The fringed alluvial fans of the MP. A) The Northern alluvial fans: 1.Ramadi Fan; 2.Al-Fatha Fan; 3.Al-Adhaim Fan; 4.Diyala Fan. B) The coalescent alluvial fans of the Eastern sector. C) The southernmost alluvial fans: 5.Al-Slaibat Fan; 6.Al-Batin Fan; 7.Dibdibba Fan. D) The western Karbala-Najaf Fan.	34
Figure 5 - A) The oxbow lakes of the Tigris between Bagdad and Numaniya. B) The anastomosing pattern of the Euphrates and its main distributary, the Shatt al-Hilla. C) The abandoned course of the Euphrates north of Hammar Lake, pointed out by black arrows. D) The Tigris' distributaries, the active Shatt al-Gharraf and the traces of the abandoned Dujaila.	37
Figure 6 - The Ahwar area of the LMP.	38
Figure 7 - The dendritic tidal creeks of the southern tidal flat.	39
Figure 8 - The tiles of Landsat 8 available for the LMP. The tiles are identified by their Path-Row code in the table, specifying the acquisition date for the wettest and driest period.	42
Figure 9 - The tiles of COSMO-SkyMed© furnished by ASI. The tiles are identified by their file-naming convention. The blue and pink tiles are the ascending couple, while the yellow and green tiles are the descending ones.	46
Figure 10 - The downloaded AW3D30 tiles for covering the LMP. Each tile is identified by its latitude-longitudinal name.	49
Figure 11 - The selected tiles of GDEM2 for covering the LMP area, identified by their latitude-longitude name.	50
Figure 12 - The adopted methodological scheme (workflow and software) for the analysis conducted in this project.	52
Figure 13 - The mosaicked DEMs AW3D30 and GDEM2, with the colour-coded re-classification. Specifically, both of DEMs are classified 1-m interval between 0 and 10 m a.s.l., 2-m interval between 10 and 30 m a.s.l., 5-m interval between 30-50 m a.s.l., 10-m interval between 50 and 100 m a.s.l. and 50-m interval between 100 and 200 m a.s.l. Both of DEMs are clipped following the 200 and 250 m contour line.	54
Figure 14 - A) The conceptual cross section sketches of an active and abandoned channel, comparing the double-convexity and the single-convexity, respectively. B) The conceptual sketch of a typical fan-shaped crevasse splay due to a levee break at the outer zone of a river belt. The along-dip crevasse sub-division adopted in this study is	

reported laterally. Direction and terminology for the altimetric profiles are XX' = along-dip direction, YY' = cross direction. 55

Figure 15 - Satellite nadiral view of the LMP from TerraColor satellite imagery with the distribution of the active and abandoned crevasse splays recognized in the investigated area during the visual inspection. The active crevasse C10 along the Tigris and the abandoned crevasse C2 along the Euphrates paleobranh are indicated by black arrows, while the entire dataset of the crevasse splays is reported below, highlighting the sample crevasses described in Chapter 6. 58

Figure 16 - Example for producer and user accuracy (sensu Banko 1998) for a typical landforms association of a crevasse splay. 60

Figure 17 - The interferogram before (left) and after (right) the Goldenstein Phase Filtering (from Braun, 2020). 62

Figure 18 - The difference between the wrapped phase and the unwrapped phase (from Braun, 2020). 62

Figure 19 - A) TerraColor example of abandoned channel (pointed out by black arrows). B) The reconstruction of the abandoned multi-channel fluvial system which mainly characterized the early Holocene landscape of the LMP. 65

Figure 20 - The reconstructed morphology of the Persian Gulf shoreline during the maximum marine ingression at 6000 yrs BP. 66

Figure 21 - The location of the selected crevasse splays C10, C13, C9 and C2. 67

Figure 22 - Example of active (C10 and C13) and abandoned (C2 and C9) crevasse splays recognized in the area. The traces of altimetric profiles shown in Figures 23 and 24 are reported: AA' = along-dip profiles, BB' = cross-direction profiles of the proximal sector, CC' = cross-direction profiles of the middle sector, DD' = cross-direction profiles of the distal sector. 68

Figure 23 - Altimetric profiles based on the elevation data of both AW3D30 (blue line) and GDEM2 (red line) datasets. Moving averaged values range from 10 up to 20 m. Location of the profile traces is reported in Figure 22. A) Altimetric profiles for the crevasse C10; B) Altimetric profiles for the crevasse C13. 70

Figure 24 - Altimetric profiles based on the elevation data of both AW3D30 (blue line) and GDEM2 (red line) datasets. Moving averaged values range from 8 up to 20 m. Location of the profile traces is reported in Figure 22. A) Altimetric profiles for the crevasse C2; B) Altimetric profiles for the crevasse C9. 71

Figure 25 - Spatial distribution of NDVI, during the wettest period, for the active (C10, C13) and the abandoned (C2, C9) crevasse splays. 73

Figure 26 - Spatial distribution of the CR, during the wettest period, for the active (C10, C13) and the abandoned (C2, C9) crevasse splays. 74

Figure 27 - Classified active crevasse splays (C10, C13) using four classification methods. For the Mahalanobis and Minimum Distance, the wettest period is shown, while for the Maximum Likelihood and SAM is the driest period. 78

Figure 28 - Classified abandoned crevasse splays (C2, C9) using four classification methods. For the Mahalanobis and Minimum Distance, the wettest period is shown, while for the Maximum Likelihood and SAM is the driest period. 79

Figure 29 - Localization of the reconstructed area surrounding the archaeological sites of Lagash and Tell Zurghul. The red rectangle is detailed in Figures 30 and 31 while the grey rectangle is detailed in Figure 33. 80

Figure 30 - The map of fluvial (principally channels and avulsions, both active and abandoned) and aeolian processes of the Shatt al-Gharraf and Dujaila floodplains, in addition to the anthropic features. 81

Figure 31 - The spatial distribution of clay minerals (CR) and vegetation (NDVI), both computed for the wettest period. The areas with the highest values of CR and NDVI correspond to the croplands. 82

Figure 32 - Altimetric profiles based on the elevation data of AW3D30 dataset. Moving averaged values is 20 m. Location of the profile traces is reported in Figure 29. A) The active channel of profile BB' where the baguette levees configuration occurs, pointed out by black arrows. 83

Figure 33 - The CSK-DEM of the Tell Zurghul area, where the recognized fluvial processes and human features are essentially channels and canals. 84

Figure 34 - Altimetric profiles based on the elevation data of CSK-DEM dataset. Moving averaged values is 40 m. Location of the profile traces is reported in Figure 29. 85

Figure 35 - The re-mapping of active (C10 and C13) and abandoned (C2 and C9) crevasse for highlighting the hierarchy of the flood event. 87

Figure 36 - Along-dip conceptual altimetric profiles of typical active and abandoned crevasse splays as inferred from this research. Crevasse splay section terminology according to Figure 14B. 88

Figure 37 - The idealised transversal cross section of the intermediate valley sector in a hypothetical northern Marche river. The deposits are coded as as=minor fill terraces, fs=in-growing meandering, ia=inclined alluvial sheets, rs=rock-cut strath terraces, Fb=aggradation of braided facies in full-glacial condition (from Nesci et al., 2012). 97

Figure 38 - The San Michele al Fiume area where the cores described and dated by Dall'Aglio et al. (2012) have been drilled and the cross section transversal to the trunk valley. 98

Figure 39 - The outcrop of the fossil forest of Valcesano where the stratigraphic structures of the Fb and Fs facies are appreciable. 99

List of tables

Table 1 - <i>The aspects, and their limitations, of a fluvial system that can be considered for reconstructing the fluvial response to a climate input (sensu Macklin et al., 2012).</i>	20
Table 2 - <i>The spectral bands of the Landsat 8 sensors, OLI and TIRS, compared to the ones of Landsat 7 ETM+.</i> 41	
Table 3 - <i>The standard file-naming convention for Landsat 8 Level 1 product.</i>	42
Table 4 - <i>The four acquisition mode's specifications available for the COSMO-SkyMed® SAR. T = transmit, R = receive, H = horizontal, V = vertical.</i>	43
Table 5 - <i>The standard file-naming convention for COSMO-SkyMed® products.</i>	45
Table 6 - <i>The main features of ALOS remote-sensing instruments.</i>	48
Table 7 - <i>The parameters of ASTER's subsystems (VNIR, SWIR and TIR).</i>	50
Table 8 - <i>The most accurate thresholds for each classification method.</i>	60
Table 9 - <i>Accuracy of each ROIs derived from the different classification methods applied in this thesis.</i>	75

Forewords

Before you lies the dissertation “Remote sensing applications for the assessment of the geomorphic response of fluvial systems to the Holocene Climate Changes”, that has been written as completion to the Ph.D. project in Physical Geography and Geomorphology, at the Department of Earth Sciences (*XXXIII ciclo*) of the Sapienza University of Rome. Each aspect of my Ph.D. project, from the study area, investigation methods and materials to the obtained results and their discussion, are written to fulfil the graduation requirements of the Ph.D. program in Earth Sciences. Specifically, some chapters are based on the main outputs collected in the following research papers:

- Iacobucci, G.; Troiani, F.; Milli, S.; Mazzanti, P.; Piacentini, D.; Zocchi, M.; Nadali, D. Combining Satellite Multispectral Imagery and Topographic Data for the Detection and Mapping of Fluvial Avulsion Processes in Lowland Areas. *Remote Sensing*. **2020**, *12*, 2243;
- Iacobucci, G.; Nadali, D.; Troiani, F.; Zocchi, M. The Shape of Water: How landscape and environment affected and changed the morphology of Tell Zurghul in the Ancient State of Lagash. *In prep.*

Moreover, preliminary results attempted during the Ph.D. program have been reported in several national and international meetings, like EGU and INQUA Congress.

My Ph.D. project started in October 2017, when I undertook a scholarship, and lasted three years, during which my Supervisor Prof. Francesco Troiani has been always available for tutoring and resolving any doubt. Several courses, seminars and training activities were attended, both in Italy and in Germany at the Institute of Geography of the Leipzig University, under the supervision of Ph.D. Hans von Suchodoletz. Especially the first two years have been dedicated to the courses proposed by the Department of Earth Sciences of the Sapienza University and workshops at the departments of Earth Sciences of Pisa and Roma Tre universities, focusing on MATLAB, geostatistical analysis and palaeoenvironmental-palaeoclimatic reconstructions. Moreover, I have taken part in two Ph.D. fieldtrips: Stromboli - Campi Flegrei in May 2018 and Ethiopia in February 2019.

During these three years, the collaboration with Prof. Davide Nadali, co-director of the Italian Archaeological Expedition to Nigin - Tell Zurghul, has given to this project a multidisciplinary approach, where geomorphological and archaeological evidences and perspectives perfectly integrated each other. This Archaeological Mission has been founded by the Sapienza University of Rome, winning several “Grandi Scavi” projects since 2016, and by the Italian Ministry of Education and University, winning a PRIN in 2018 (*Progetti di Ricerca di Interesse Nazionale*). Moreover, the collaboration with Ph.D. Daniela Piacentini (Department of Pure and Applied Sciences of the University of Urbino “Carlo Bo”) leaded to improving the geomorphological reconstruction of the fluvial environment at Ostra archaeological site, in the valley sector of Misa River (Northern Italian Apennines). Last but not least, the co-tutoring of different thesis, both MSc and BSc, offers the opportunity of working on different case study, applying remote sensing techniques and geostatistical analysis.

The central topic of my Ph.D. project is the identification of the geomorphological responses of the fluvial systems to the Holocene (“Rapid”) Climate Changes, considering a wide, barren floodplain where two of the most known rivers flow: the Lower Mesopotamian Plain (Iraq). Here, fluvial-deltaic processes of the Tigris-Euphrates river system prevail, and the relevant management of the water resources lead to evaluating the human impact over the natural drainage network. Furthermore, an innovative remote-sensing approach has been adopted for identifying the fluvial responses through the multispectral analysis and the elaboration of the elevation datasets from different satellite missions. In order to present the traditional field-based study for the identification of the fluvial response to rapid climate changes, a second case study has been selected in the Mediterranean area, along the trunk valley of the Cesano River (Northern Italian Apennines). Here, a well-exposed cut-and-

fill sequence represents a unique archive for studying the current post-glacial morphodynamics experienced by the fluvial system. While the remote sensing approach adopted in this thesis has been more effective in the barren landscape of the Mesopotamian Plain and the concerning results will be discussed in the following chapters, the Italian area cannot be considered sufficiently completed, since the field work has been interrupted during the pandemic emergency due to the Coronavirus, and its bibliographic review, with only some new appraisals, has been considered exclusively in the Appendix.

Thus, the structure of this dissertation is as follows:

- *Chapter 1*: the introduction to the main issue of this thesis and its specific aims.
- *Chapter 2*: the Holocene (“Rapid”) Climate Changes, their recognition, and their relevant role in the fluvial morphodynamics, the development of the early human societies along the World’s longest rivers.
- *Chapter 3*: the study area of the Mesopotamian Plain, its geological and geomorphological settings, the present and Holocene climate conditions characterizing the area.
- *Chapter 4*: the detailed description of each satellite mission and their specific product details adopted for the remote investigation of the Lower Mesopotamian Plain.
- *Chapter 5*: the description of the methods for analysing and elaborating the optical, multispectral and elevation data, distinguishing among the preliminary visual inspection, the multispectral analysis, and the topographic analysis of the micro-relief.
- *Chapter 6*: the obtained results considering two different scale of investigation, the medium scale for the avulsion processes of the entire Lower Mesopotamian Plain and the large-scale for the geomorphological mapping of the archaeological site of Tell Zurghul.
- *Chapter 7*: the discussion of the results, highlighting the potential application of the integration between multispectral analysis and topographic analysis of the micro-relief for discerning the state of activity of the avulsion processes and emphasizing the limit of the same method combination for the large-scale investigation.
- *Chapter 8*: the summary of the main conclusions derived from both the medium and the large-scale investigation.
- *Chapter 9*: the prospective applications of this method combination for a multidisciplinary research, for enhancing the knowledge about the climate change and the resilience of our society.
- *Appendix*: the Mediterranean case study of the Cesano River as a prospective example of the limits of a study exclusively based on field-works for the identification of the fluvial systems response to rapid climate changes and for distinguishing the dynamic response due to human activities during the Holocene and historical times.

I hope you enjoy your reading!

Rome, October 14, 2020

Giulia Iacobucci

1. Introduction

Rivers are an essential component of the landscape and have been always considered by human population as an association of several resources, such as a continuous renewable water supply, a potential source of energy, food and transport, and a rapid removal system for useless substances. Anyway, rivers also represent a potential risk to human population because of floods, droughts, pollution, and erosion (Knighton, 1998). In spite of this dual aspect of the rivers, they play a key role in political, social, and economic policy of several countries, where frequently the highest percentage of the population lives in the floodplain areas.

The rivers can be considered as open systems, where energy and matter exchange with the external environment; indeed, the latter is the sum of several factors, among which the climate is of leading significance in this thesis, especially considering the last 10,000 years (i.e., the Holocene). After the end of the last glaciation about 12,000 years ago, the climates and the environmental conditions began to be similar to the modern ones. Moreover, the impact of human beings on the environment increased progressively through the transformation from hunting-fishing-gathering communities to city-dweller (Roberts, 2014).

Among the world's different environments, the floodplains have been the most altered by human activity during the Holocene, a period over which relevant cultural and environmental changes have occurred (Roberts, 2014; El Bastawesy et al., 2020), offering a challenge for geomorphologists and archaeologists in order to define both the human impact on the environment and the consequences of the environmental changes on humans living along rivers. The evidence of the Holocene high-frequency, low-magnitude climate fluctuations, also known as Holocene Climate Changes, is well demonstrated by several proxy data such as lake and marine records, speleothems, ice-cores, and tree-rings. Nonetheless, the effects of these events on the landscape are still object of research and are so far to be unravelled, especially along floodplains where the fluvial processes prevail.

The general goal of this thesis is to contribute to the studies of the geomorphological response of the fluvial systems to the Holocene Climate Changes, whereas the specific aims can be summarized through the following questions:

- i. How did the Lower Mesopotamian fluvial morphodynamic adjust to the Holocene Climate Changes?
- ii. Can we recognize the state of activity of the avulsion processes through a complete remote sensing approach over a wide study area?
- iii. Taking into account the sample area of the archaeological site of Tell Zurghul, how the Holocene Climate Changes impact on ancient societies and what is the human response?

The exclusive focus of this thesis on the study of the fluvial processes in a wide floodplain within the Lower Mesopotamian Plain is essentially due to four main reasons:

- a) The floodplains, as well as other environments like marshlands and sand dunes, potentially preserves an excellent archaeological record (Brown, 1997), which most likely can be used as proxy for reconstructing the past environmental conditions;
- b) Over the Holocene, the human impact on the fluvial processes has increased progressively (Roberts, 2014); since the Lower Mesopotamian Plain is part of the Fertile Crescent known as the cradle of civilization, this area is extremely suitable for evaluating the human-climatic-environment interactions;

- c) The Lower Mesopotamian fluvial system has been repeatedly modified by a wide range of autogenic, allogenic, and human-made processes (Jotheri, 2016), which activate new watercourses and de-activate the older ones, modify the channel courses and their pattern;
- d) Considering that two-thirds of the Iraqi population lives in the Mesopotamian floodplain, these continuous changes on river morphodynamics frequently have caused, and still bring about, several problems related to floods, desiccation, soil salinization and desertification, increasing their concerning risks; thus, the Lower Mesopotamian Plain represents an ideal study area where the knowledge about effects of the past climate changes on the fluvial system and directly/indirectly on the early human societies may provide information for better comprehending the effects of ongoing climate change on the modern societies.

Moreover, the multidisciplinary approach adopted for the study of the sample study area at the Tell Zurghul archaeological site leads to integrating the archaeological and geomorphological data for reconstructing the landscape where this city flourished. The collaboration with the Italian Archaeological Mission at Tell Zurghul founded by the Sapienza University of Rome deals with the analysis of the function and the role of water within a complex environmental system encompassing both natural watercourses and anthropic canals that make up the waterscape of the Lower Mesopotamian Plain.

Taking into account the ongoing increase of Holocene research since the 1980s and the endorsing multidisciplinary approach through archaeological and geological methods, the reconstruction of the global environmental changes has sparked interest also of the remote sensing techniques, inasmuch since the first climate satellite launched in 1959 (i.e., Vanguard II of NASA), the satellite missions increased exponentially up nowadays, collecting more or less 100 terabytes per day of climatic data (Pierce, 2020; Mohny, 2020). Satellite remote sensing and in situ measurements are crucial for improving our knowledge of the global climate system dynamics and its impact over both the environment and the human societies, following one of the main geological principle known as “the present is the key of the past” of Charles Lyell (1830-1833). Remote sensing information from different Earth Observation missions has been adopted for several Earth sciences studies and applications, deriving land change information to quantify and model physical processes occurred on Earth surface, as well as to monitor land cover and land use. Along multiple temporal scales, remote sensing datasets provide useful information on longer-term changes, for example comparing the same landform over the years. Thanks to the recent improvements in remote sensing technologies, multiple remotely sensed data products are quickly available, leading to collect and compare several data types from a wide geographical area like the Lower Mesopotamian Plain. Indeed, the exclusive use of either DEMs or multispectral data is inappropriate and lacking for the study of the fluvial morphodynamic of a wide floodplain characterized by very low elevation ranges such as the Lower Mesopotamian Plain. Thus, a multi-sensor approach leads to comparing and cross-validate the outputs derived from the topographic analysis of the micro-relief and the multispectral analysis.

2. Holocene (“rapid”) Climate Changes

The climate of the Earth had always changed and still modifies, showing variations both temporally and spatially (Mock, 2006). Indeed, most of the climate variable continuously changing and so the intervals with low variability must be considered as exceptions rather than the normality (Bertlein, 2006). The time range of climate’s variability shows different temporal scales, reflecting the nature of the external and internal forcing of climate system itself (Bertlein, 2006). For example, in a shorter timeframe of every other year or so, climatic changes due to ENSO (*El Niño*) events, are thought to affect regions throughout the globe; while in much longer timeframes, like tens of thousands of years, drastic climatic changes occurred, leading to relevant environmental changes (Mock, 2006).

During the 50s and 60s, the most significant input in Quaternary palaeoclimatology derived from the early studies on oxygen-isotope records of deep-sea sediments (e.g. Urey, 1948; Epstein and Mayeda, 1953; Emiliani, 1966; Shakelton, 1967). The isotope records lead to accepting the Milankovitch theory of climate change, furnishing a model for the global climate changes and their effects on ice volume and eustatic sea level (Blum and Törnqvist, 2000).

Climatic variations are characterized by hierarchical controls and responses, where the highest level is occupied by the external controls of climate system, proceeding through global, hemispheric, continental, and regional scales, up to the local variations at the lowest level. Each level of the hierarchy rules the variations of the components at lower levels. For example, in a timespan of 10^4 to 10^6 years, ice sheets are controlled by orbital variations in insolation, whereas at shorter time scales (10^4 to 10^3 years), ice sheets can directly influence the global temperatures and atmospheric circulation (Bertlein, 2006).

The evidence of climate and sea-level change, geomorphological and hydrological processes, vegetational developments, and faunal migrations are well preserved by Holocene stratigraphic records, leading to being studied at high temporal resolution (Walker et al., 2012). Moreover, the Holocene Climate Changes (hereafter HCC) highly impacted on early human societies, which grew and developed during the last, current interglacial, providing further evidence of climate fluctuations through archaeological records (Kaniewski et al., 2013). Thanks to the typical multi-disciplinary approaches adopted for reconstructing the Holocene environmental changes, both archaeological and geological records testify the occurrence of climate fluctuations on multi-centennial to millennial time-scales and rapid shifts (Kaniewski et al., 2013; Kadlec et al., 2015; Weiss, 2016; Sadori et al., 2016; Holmgren et al., 2016; Benjamin et al., 2017; Xiao et al., 2019; Bini et al., 2019; Zhang et al., 2020; Zhao et al., 2020). Anyway, it is inaccurate considering that the HCC always lead to societal collapse. Indeed, many studies evidence that favourable climate generally contributes to reasonable societal development, while severe climate changes do not necessarily lead to the opposite (Holmgren et al., 2016). Human societies have always been adapting to a fluctuating climate and environmental conditions developing different strategies, whose success is due to the magnitude, amplitude, and duration of the climate change. The Middle East, as well as the Mediterranean region and all the areas where the Early River Valley civilizations developed (i.e. Huang He and Indus rivers), are the suitable areas where information about human and environmental history is well preserved, leading to unveiling the interactions between climate, environment and humans over different time scales (Macklin and Lewin, 2015; Holmgren et al., 2016; Bolikhovskaya et al., 2018; Rice et al., 2020).

Multi-century scale changes between cold and warm (or dry and wet) after the Last Glacial Maximum seem to be cyclical, with periods of about 2000-2800 and 1200-1500 years, comparable to the Late Pleistocene Dansgaard–Oeschger events (Denton and Karlén, 1973; Bond et al., 1997, 2001;

Wanner et al., 2008). Bond et al. (2001) identified eight evident shifts in ocean surface hydrography during the last 12 ka years, after that known as Bond Events. These events are recorded as southward and eastward expansion of drift ice in the Nordic and Labrador Seas, already known as Heinrich events (Heinrich, 1988). The occurrence of these ice-rafted detritus is mainly linked to the massive discharges of icebergs from Hudson Strait (Goldstein and Hemming, 2003), most likely due to the decrease of solar irradiance. The variance in solar activity implies a relevant magnitude of these events which must be recorded worldwide (Bond et al., 2001). Indeed, data from previous studies highlighted cooling events, like in Scandinavia, Greenland, and Netherlands, perfectly matching with the Bond events (Bond et al., 2001). Despite the causal mechanism of these events is still an open question for the international scientific community, the rapid climate changes emphasize the interconnected dynamics among atmosphere, cryosphere, and ocean system (Blum and Törnqvist, 2000). However, a global change in atmospheric circulation, for example, is frequently split into various regional responses, significantly different from the global trend (COHMAP Project Members, 1988; Blum and Törnqvist, 2000), making more difficult the identification of the climate events' causes.

The Sub-commission on Quaternary Stratigraphy (SQS) of the International Commission on Stratigraphy (ICS) established the INTIMATE group (INTEgration of Ice-core, MARine and TERrestrial records of the Last Termination), for formally subdividing the Holocene (Walker et al., 2012). The last 11,7 ka years have been divided into three stages, named *Greenlandian*, *Northgrippian* and *Meghalayan*, officially ratified by the International Union of Geological Sciences (IUGS) on 14th June 2018 (Walker et al., 2012; Walker et al., 2018). Anyway, the first subdivision of the Holocene was proposed by Mangerud et al. (1974), who defined three biozones through the radiocarbon dating of the palynological data. However, this vegetation-based subdivision is applicable only to a local or regional scale because the vegetation response to the climate change is temporally shifted (Björck et al., 1998; Wanner et al., 2008; Walker et al., 2018).

The great preservation of the Holocene successions leads to studying the last tens of thousands of years with a relevant temporal resolution, improving the reconstruction of the long-term climatic and environmental trends of this epoch. Therefore, each stage has been linked to Global Boundary Stratotype Section and Point (GSSP), one in the NGRIP1 Greenland ice core and the other one in a speleothem of Mawmluh Cave (India) (Walker et al., 2012; Walker et al., 2018).

The Early-Middle Holocene boundary (i.e. the Greenlandian upper limit) corresponds to the 8.2 ka event, a short-lived cooling episode detected by numerous proxy data, not only in Greenland and North Atlantic Ocean. It is linked to the decrease of North Atlantic Deepwater formation and the northward heat transport because of the melting of Laurentide Ice sheet (Kleiven et al., 2008; Walker et al., 2012). The South Atlantic pollen and geochemical data report an increase of precipitation, most likely due to the strengthening of the South Atlantic westerlies or the increase of the sea surface temperature (Ljung et al., 2008; Walker et al., 2012). Moreover, the 8.2 ka event has been recorded by both settled and hunter-gatherer communities of north Africa, south Europe and Near East, where the increased aridification occurred due to the cooling of North Atlantic surface water (González-Sampériz et al., 2009; Mercuri et al., 2011; Walker et al., 2012).

The Middle-Late Holocene limit (i.e. the Northgrippian upper boundary) is linked to the 4.2 ka event, known as Megadrought Event mostly occurred in the mid/low latitude with a decadal-century scale (Walker et al., 2012; Weiss, 2016). The forcing mechanism behind the widespread 4.2 ka event is less clear than the 8.2 ka event, and different hypothesis has been proposed. One of these is the southward shift of the Inter-Tropical Convergence Zone (ITCZ) leading to the aridification of low latitude areas and the strengthening of westerlies over the North Atlantic which increase the precipitation and the development of North American glaciers. The cooling of the Pacific deep water

triggered the modern El Niño Southern Oscillation (ENSO), which weakened the Asian monsoon and increased the aridity of the Pacific and Asian regions (Fisher et al., 2008; Walker et al., 2012; Weiss, 2016; Li et al., 2018; Bini et al., 2019; Xiao et al. 2019). As during the 8.2 ka event, the effects of the Megadrought Event on the human societies are well represented by worldwide geochemical, stratigraphical, vegetation and archaeological records. Some of them are pollen, diatom and speleothem data of the North America where the aridity condition is recorded as well as in the Mediterranean, Middle East, Red Sea and Arabian Peninsula proxy data (Cullen and deMenocal, 2000; Magri and Parra, 2002; Di Rita and Magri, 2009; Roberts et al., 2011; Walker et al., 2012; Wiener, 2014; Weiss, 2016; Walker et al., 2018). Also, the tropical and sub-tropical areas of Africa and South America shows an increase of drought during the Middle-Late Holocene, as shown by lake sequences and the Kilimanjaro and Peru ice-core records (Thompson et al., 2002; Russell et al., 2003; Davis & Thompson, 2006; Walker et al., 2012). In other areas, the increasing aridity coincides with the increase of flood events like in China, or the strengthening of the summer monsoon like in Taiwan (Huang et al., 2011; Yang et al., 2011; Walker et al., 2012), while the southern ocean waters and Antarctica show a decrease of temperature. Similarly, the cooling and the increased moisture in the Yukon testify the widespread development of mountain glaciers (Fisher et al., 2008; Menounos et al., 2008; Walker et al., 2012). The same moist climate is recorded by the north European peat sequences (i.e. Great Britain, Ireland, and Sweden), as well as other proxy data from neighbouring areas (Walker et al., 2012; Walker et al., 2018).

The robust amount of proxy records collected worldwide highlights the relevant variability of the Megadrought Event, whose effects are relevant also for the most developed and complex societies. Indeed, the abandonment of rain-fed regions, habitat-tracking to riverine refugia, and the collapse of innovative societies are archaeologically evident across Spain, Greece, Palestine, Egypt, Mesopotamia, the Indus Valley and the Tibetan Plateau, while the Yangtze and Huang He River societies ended (Weiss, 2014; D'Alpoim Guedes et al., 2016; Blanco-Gonzalez et al., 2018; Guo et al., 2018; Walker et al., 2018).

2.1 Fluvial response to the Holocene Climate Changes (HCC)

The interest in the reconstruction of ancient fluvial environments has been recently reawakened because of the growing concern of the scientific community on climate changes (Knighton, 1998).

The identification of the HCC at centennial- to millennial-scale through the environmental and landscape changes offer a challengeable opportunity for geomorphologist, especially for understanding how such rapid climate changes modified boundary conditions and influenced erosional and depositional processes. Among the geomorphological systems, the rivers can be considered as entities extremely sensitive to changes on environmental conditions due to climate (Knighton, 1998; Törnqvist, 2006). Holocene climatic changes are different from region to region, although the morphodynamics and the hydrology of river systems are equally various (Macklin and Lewin, 2015).

Fluvial processes frequently leave landforms and deposits on the subaerial landscape, as well as on submerged continental shelves, where their deposits are widely recognized (Blum, 2006), forming the so-called fluvial archives. Fluvial archives are important for recording land conditions during the geological history and they can be considered as repositories of the terrestrial fauna and flora, including early human artefacts (Bridgland et al., 2014). Each landform and sedimentary record are due to different geomorphological regimes with the specific depositional environment, preserving information about the evolution of landscape and surface processes due to climate change, sea-level change, and active tectonics (Roberts, 2014; Blum, 2006). Thus, fluvial landforms and deposits are indispensable for reconstructing past hydrological framework, considering different time scales and

allogenic factors such as tectonic, eustatism and human influences (Macklin et al., 2012). Anyway, the fluvial archives are not straight climatic records like marine or ice cores, but their geomorphic-sedimentological proxy data unveil environmental changes focusing on a more regional scale, being more representative for a detailed reconstruction of a specific area (Zielhofer et al., 2008). Moreover, fluvial archives are greatly sensitive to the human impact, preserving past human-environment interaction (Faust et al., 2004; Zielhofer et al., 2008; von Suchodoletz et al., 2015; von Suchodoletz and Faust, 2018; Chauhan et al., 2017; Jotheri et al., 2018; Zhao et al., 2020).

Penck and Brückner (1909) were the first to recognize the cyclical occurrence of glacial-interglacial periods, inferring four periods during the Pleistocene with a long glacial and interglacial period and a short transition between them. Penck and Brückner's (1909) model linked the glacial period to the fluvial aggradation, while the fluvial incision occurs during the interglacial period. Anyway, Lamothe (1918) and Fisk (1944) proposed a completely opposite model, where the fluvial aggradation is linked to the interglacial, whereas the fluvial incision mainly occurred during the glacial period. The complete disagreement among these models is essentially due to the dualism between 'continental interior' and 'continental margin', which involve the upstream or downstream controls depending on the location of the study area (Blum and Törnqvist, 2000). The three main allogenic factors that controlled fluvial systems such as climate change, base-level change (i.e. sea-level change) and tectonic input are also distinguished between upstream and downstream controls. For example, climate change is mainly classified as an upstream control while the sea-level change is a downstream one, opening the debate about their downstream/upstream extension (Törnqvist, 2006).

Fluvial systems developed three main responses to these allogenic factors: i) changing discharge regime, ii) changing fluvial pattern, iii) changing longitudinal profiles through aggradation or incision (Törnqvist, 2006, Blum and Törnqvist, 2000, Macklin et al., 2012). The modification of discharge regime and fluvial pattern are the most direct response to a climate input, altering hydraulic geometric parameters (i.e. channel width, depth, and sinuosity) and the spatial distribution of erosional and depositional landforms (Törnqvist, 2006; Blum, 2006). The first studies about the impact over hydraulic geometry date back to the 1960s, like Schumm's general model (Schumm, 1965) for the fluvial response to climate change, where i) spatial and temporal scale, ii) convergent responses due to different external forcing, iii) divergent responses due to similar external forcing, iv) different fluvial sensitivity due to different thresholds for change, and v) complex responses due to internal complexity must be considered for describing the fluvial response to a climate change as geographically circumscribed, nondeterministic and nonlinear (Blum and Törnqvist, 2000). Indeed, rapid climate change most likely modifies the boundary conditions of a fluvial system, whose response is frequently spatially non-uniform.

The non-uniform fluvial response is the main reason for a complicated interpretation of fluvial archives, but other four factors must be considered. The first one is the concurrence of non-climatic factors, such as human land use, river management, base-level oscillation and tectonic activity, which recognition and discerning are not always so evident and most frequently their effects co-exist and superimpose in space and time. Secondly, the hierarchical organization of fluvial systems allows to develop equilibrium landforms and to adjust channel size and shape related to discharge and sediment supply. When sediment fluxes and river flows are modified, the river may laterally shift, favouring the formation of cut-off channels where past channel dimensions and post-cut-off sedimentation are preserved. However, lateral migration and cut-off are also triggered by extreme events such as floods. Considering extended rivers and basins, their low lateral shift allows developing widespread flood basins, as well as avulsion processes and floodouts, which provide the most complete sedimentary record. Anyway, for largest rivers, the sedimentation may be restricted in deltaic and offshore

environments, furnishing the best record of climate fluctuation. Discerning allogenic and autogenic controls on river response is not so straightforward, especially relating to short-term, highly frequent episodes (i.e. 100 years or less). Indeed, some autogenic changes are mainly unidirectional, showing a change in the boundary conditions within the basin and among the nested catchments.

The third one is the equivocal recognition of climate change through clear hydrological, sedimentological, and morphological river changes. Frequently, flood events are larger and more frequent during climate change. Anyway, it is mistaken considering active\quiescent periods regarding the occurrence and the intensity of flood events, as evidence of the climate change. The concept of climate change as river morphodynamics is better defined as statistical trends and data averages over decadal to sub-epoch timescale.

Lastly, linear and non-linear response of the river system is crucial for reconstructing past environmental conditions. For example, between grain size and flow parameters, there are linear relationships, useful for estimating past river discharge, but it must be considered that scattered data and thresholds involve non-linear response. Thus, the linear response within limits and thresholds must be taken into account to prevent lacking environmental reconstruction (Macklin et al., 2012 and reference therein).

The development of the Oxygen Isotope stratigraphy and ^{14}C dating lead to inferring a chronological framework for climate changes (Blum, 2006). Indeed, the fluvial sequences frequently have a reliable biostratigraphy, that with the occurrence of archaeological artefacts, enables the dating of fluvial archives. Different geochronological techniques can be applied such as radiocarbon, Uranium-series dating of carbonate and amino-acid dating of molluscan fossils; but the luminescence dating is the most widely adopted for clastic/minerogenic fluvial sediments (Bridgland and Westaway, 2014).

If the dating of fluvial sequences is essential for a chronologically restricted reconstruction, the back-testing and forecasts are other two useful approaches for determining river channel and floodplain responses to a climate change. For this purpose, different aspects, despite their limitations, can be contemplated to identify the impact of a climate change, such as the ones illustrated in **Table 1** (Macklin et al., 2012).

Table 1 - *The aspects, and their limitations, of a fluvial system that can be considered for reconstructing the fluvial response to a climate input (sensu Macklin et al., 2012).*

Aspects	Limitations
Empirical relationships between paleochannel dimensions (width-depth-sinuosity) and bankfull discharge	<ul style="list-style-type: none"> • The deterministic estimation of channel components is unpredictable • Bank stability factors contribute to the channel dimensions
Threshold changes in channel pattern and sedimentation style	<ul style="list-style-type: none"> • Unmeasurable factors for sharp hydraulic distinction • Few knew about the time, lags and pathways for these transformations
Sediment size and discharge magnitude	<ul style="list-style-type: none"> • Partially known • Broad empirical relationships are adopted for coarse sediments where a wide range of transportable sediment size is available • Datable record of flood deposits is considered for the finest sediments.
Rates of activity in terms of lateral channel shifting and vertical flood-unit deposition	<ul style="list-style-type: none"> • Lateral accretion is poorly dated • Rates of sedimentation in strongly influenced by soil erosion and human activity
Cut-and-fill terraces as evidence of fluctuations in sediment supply and local sediment transporting capacity	<ul style="list-style-type: none"> • Impossible discerning between allogenic and autogenic mechanisms, as well as the upstream and downstream controls

2.2 The Early River Civilizations

The Quaternary fluvial records unravel the increasing influence of the global cooling on the environment, modifying the landscape through the erosional isostatic uplift, the incision, and the formation of river terraces. Instead, the Holocene fluvial environments record the intensifying role of early human societies, which modified both the catchments and the slopes through deforestation, farming, industries, and mineral mining (Bridgland et al., 2014; El Bastawesy et al., 2020bas).

The HCC are quite different among latitudes, as well as the fluvial and environmental dynamics, but their effects on human societies are not always equal and predictable. The multi-centennial episodes of “flood-rich” and “flood-poor” principally impacted five kinds of flooding and settlement scenarios, corresponding to different geomorphological units, defined by Macklin and Lewin (2015) as i) alluvial fans and aprons, ii) laterally mobile rivers, iii) rivers with well-developed levees and floodplain, iv) rivers characterized by avulsions and floodouts and v) large river feeding wetlands. All these geomorphological units are the ideal areas where the early human societies arose and developed, but their resilience to the HCC essentially depended on which kind of modifications they dealt with, that are potentially manageable and incremental from year to year, catastrophic or chronic when disadvantageous conditions were unexpected or extended over many decades, respectively (Macklin and Lewin, 2015). For the Early River Civilizations, common adverse conditions were the changing in magnitude and frequency of floods, recurring droughts and drastic river channel modifications, which can trigger an environmental crisis and societal collapse. For example, the so-called Megadrought Event caused the interruption of the Mediterranean westerlies and the Indian Summer Monsoon, whose effects are perfectly recorded by areas where detailed and numerous archaeological evidence are still preserved (i.e. the Mediterranean, the Levant, Egypt, Turkey and

Mesopotamia) (Macklin and Lewin, 2015; Weiss, 2016). Between 4.2 and 3.9 ka, different societies based on cereal-agriculture and with several political-economic organizations collapsed synchronously, as testified by intensive regional settlement surveys, high-resolution radiocarbon dating for abrupt abandonment of villages and cities, epigraphic and radiocarbon data of the collapses (Weiss, 2016).

The Early River Civilizations developed near the greatest rivers of the Earth, such as the Huang He, Indus, Nile and Tigris-Euphrates rivers. Despite these rivers are in rather dry environments, the flourishing of agriculture and the development of organized societies and urban culture were strongly connected with the natural inundation or managed irrigation. Thus, changes in the hydromorphic regime frequently caused a societal and political crisis, leading to civil wars and settlement abandonments (Butzer, 2012; Macklin and Lewin, 2015). Indeed, the Indus Civilization abandoned some villages because of long-lasting drought, as well as the inhabitants of Nile in Nubia, where the reduction of river flow with channel network contraction or retraction occurred during the Late Holocene, or like the Huang He and Yangtze rivers' populations where floods became disruptive and unmanageable, or the Mesopotamian societies where soil salinization prevented farming and pastoralism (Cullen et al., 2000; Stauwbasser et al., 2003; Giosan et al., 2012; Kidder and Liu, 2012; Macklin et al., 2013; Macklin and Lewin, 2015; Weiss, 2016, Sarkar et al., 2016; Manning et al., 2017; Li et al., 2018; Xiao et al., 2019; Zhao et al., 2020).

The agriculture potential of these greatest rivers was also guaranteed by large-scale soil and water manipulation, leading to the development of hydraulic irrigation systems. Irrigation agriculture is sensitively dependent on "perfect" flood: higher flood could destroy settlements and granaries, whereas lower flood could cause poor crop, food shortage and famine. The Lower Mesopotamian Plain is one of the areas where the irrigation agriculture and the organised society occur as early as the Lower Holocene, transforming completely the environment through the digging of canals, the preservation of the irrigation system and the avoiding channel siltation. The rather common occurrence of natural and human-induced avulsions led to developing a wide distributary channel system, where most of the channels and the canals, fed by the Tigris and the Euphrates, never reached the Persian Gulf, flowing into a flat alluvial marshland area. Thus, besides the occurrence of enough floods, the second main problem of this area is the salinization, which reduces the crop yields and prevents the cultivation (Roberts, 2014).

Since the 2000s, several studies have demonstrated the significant influence of the HCC on river morphodynamics, especially modifying the discharge regime, flood frequency and magnitude (Tebbens et al., 1999; Huisink, 2000; Macklin and Lewin, 2003; Jain and Tandon, 2003; Miller et al., 2004; Macklin et al., 2010; Zielhofer et al., 2010). Thus, the arid and semi-arid areas were extremely sensitive to small differences in annual flood level. Despite the important differences among the Early River Civilizations, all of them arose on aggrading alluvial environments, which can be distinguished through the flow and the sediments carried and deposited on-site. The difference among channel patterns leads to developing specific form associations, defining peculiar flooding and settlement scenarios, where natural morphological changes are normal. Anyway, human activities have frequently modified these waterscapes through flow diversions, channel shrinkages, bank and levee stabilizations, sometimes increasing the vulnerability of the settlements and agriculture (Macklin and Lewin, 2015).

The most common hydromorphic environmental changes, whereby the Early River Civilizations had to deal with, are distinguished between *acute* (i.e., extreme floods, droughts, channel shift) and *chronic* (i.e., channel siltation, soil salinization, stream incision, water-related disease). Especially the acute changes were often triggered by human activities and in specific environments, such as fans and

mobile rivers, the distinction between climate-driven change and natural autogenic modification is far from straightforward. Anyway, the most relevant problem for the Early River Civilizations was the channel abandonment due to channel contraction and retraction, after an abrupt and permanent flow reduction (Morozova, 2005; Macklin et al., 2013; Macklin and Lewin, 2015). This commonly caused the abandonment of the riverine settlements, playing a key role in the decline or the survival of the first human societies.

During the Holocene, the occurrence of various minor changes in temperature (i.e. lower than 2-3° C) leads to the replacing of flora and fauna species, affecting the human societies dependent upon them. These small temperature changes markedly affected the length of the growing season for some species, offering a challenge for the researcher to understand how the HCC affected the early human societies (Anderson, et al., 2007).

The climatic changes not always triggered negative consequences for the early human communities. For example, Kuper and Kröpelin (2006) proposed linkage between the Mid-Holocene climatic desiccation and environmental deterioration of Eastern Sahara and the rise of the pharaonic civilization of the Nile. During the Last Glacial Maximum up to the end of the Pleistocene, the Sahara Desert is wider than today (i.e., 400 km farther southward than today), forcing the human settlements exclusively along the Nile valley. At 8500 B.C.E. the arrival of the monsoon rains replaced the hyper-arid desertic environments with the savannah-like ones, favouring the westward migration of the Nile settlers, which abandoned the Nile valley became too moist and hazardous during the early Holocene humid optimum. At 5300 B.C.E. the retreat of the monsoon rains caused the beginning of the drying of the Egyptian Sahara, triggering three main societal choices: i) some communities moved southward into the Sudanese Sahara for tracking the savannah-like habitat, ii) other settlers refuge in local ecological niches adopting nomadism, iii) other populations moved to the Nile valley where they developed an intensive irrigation-based food production, leading to the onset of the pharaonic civilization when the full desert conditions spread all over Egypt at about 3500 B.C.E (Kuper and Kropelin, 2006; Roberts, 2020). Therefore, the human population can expand despite, as well as because of, climatic changes, thanks to technical and societal adaptive strategies and the re-invention capacity, which play a more important key-role than the societal resilience. Accordingly, climatic adversities prompted innovations and adaptations, acting as a stimulus (Roberts, 2020).

Remote sensing technology makes possible for scientists to measure the health of Earth with the advantages of collecting a lot of kinds of information over a wide area, allowing repetitive acquisitions which are fundamental in dynamic environments like rivers, deltas and coasts. The variety of scales and resolutions allows the analysis and the interpretation of the images through several methods, specific for a given application or purpose. Remote sensing images provide new quantitative data useful to characterize Late Quaternary floodplains; for example, the topographic data of a DEM allows an unprecedented mapping of the entire floodplain landforms and architectural characteristics (Syvitski et al., 2012). Moreover, the high-temporal resolution of satellite data is essential for collecting measurements of the flood events, when the sediment transport and the pattern changes frequently occur (Syvitski et al., 2012).

Nevertheless, an exclusively remote sensing application involves several disadvantages, among which these two are the most relevant for this thesis: i) the introduction of human error in the analysis and interpretation of data, ii) the extracted information may be uncomplete and temporary. Whence the specific aims of this dissertation are focused on the potential application and limitations of a remote sensing approach, including the effects of the Holocene Climate Changes and the human response:

- i. The adjustment of the Lower Mesopotamian fluvial morphodynamic to the Holocene Climate Changes;
- ii. The feasibility of a complete remote sensing approach for recognizing the state of activity of the avulsion processes over a wide study area;
- iii. The feasibility of integrating remote sensing data and archaeological evidences for defining the human response to the Holocene Climate Changes, considering the sample area of the archaeological site of Tell Zurghul.

3. The Lower Mesopotamian Plain

Since Ancient Greece, the area between the Euphrates and Tigris rivers has been always known as “Mesopotamia” or “land between two rivers”, where 10,000 years ago the first agricultural practice began, where over the centuries various empires dominated and where the earliest political systems with despotic administrative hierarchies and rulers developed (Morozova, 2005; Kennet and Kennet, 2006; Garzanti et al., 2016; Engel and Brückner, 2018). It generally includes Iraq, the northeastern part of Syria, the southeastern area of Turkey and the lowlands of the southwestern zone of Iran (Jotheri, 2016).

The Tigris-Euphrates floodplain was populated by the early farming communities especially thanks to material advantages such as the irrigated area (Morozova, 2005). Indeed, the complex system of river channels and canals not only favouring agricultural yields but also offer an incomparable network of waterways for transporting and redistributing any sort of goods (Algaze, 2001; Morozova, 2005; Jotheri, 2016). Anyway, the agricultural type developed in this area is rather different between the northern and the southern sector, where a rain-fed vs channel-fed agriculture prevails respectively, due to the different climate conditions (Jotheri, 2016).

The Mesopotamian Plain (MP) is a wide lowland of about 116,000 square km (Yacoub, 2011) which is completely included in one of the World’s greatest watershed. Indeed, the Tigris-Euphrates Basin is about 880,000 square km, occupying six countries (46% of Iraq, 22% of Turkey, 19% of Iran, 11% of Syria, 1.9% of Saudi Arabia, 0.03% of Jordan) and extending from the Turkish Taurus Mountains up to the Persian Gulf (Bozkurt and Sen, 2013). Thanks to the presence of the Tigris and Euphrates rivers, the MP has also known for its fertility, as well as the Canaan Lebanon and the Nile Valley, which forms the so-called Fertile Crescent and where most of the population are settled, relying completely on water resource and transforming the landscape in a mosaic of irrigated fields (Morozova, 2005; Wilkinson et al., 2014; Wilkinson et al., 2015; Jotheri, 2016; Lawrence et al., 2016; Palmisano et al., 2019; Palmisano et al., 2021).

Both rivers rise out in the Turkish Taurus Mountains; specifically, the Euphrates is formed by the confluence of the Kara Su and Murat rivers, while the Tigris originates from the Lake Hazar and receives the contribution of several eastern tributaries along its way, reaching about 2800 and 1850 km of length respectively (Garzanti et al., 2016; Jotheri et al., 2018; Engel and Brückner, 2018).

The highest river discharge occurs during the spring season, while at the end of summer the discharge drops down; in particular, the interannual discharge variability ranges from $1.9\text{--}6.3 \times 10^{10} \text{ m}^3$ for the Tigris, and $1.0\text{--}3.6 \times 10^{10} \text{ m}^3$ for the Euphrates, according to the measurements collected between 1924 and 1946, during the relatively unaltered streamflow (Aqrawi, 2001; Engel and Brückner, 2018). Indeed, both rivers have a strongly seasonal discharge due to the mountainous headwaters, where a Mediterranean climate with hot dry summers and cold wet winters occurs, while the mean annual precipitation decreases southward where an arid to semiarid climate prevails (Garzanti et al., 2016; Jotheri et al., 2018; Engel and Brückner, 2018).

The MP can be sub-divided in five distinct physiographic regions: i) the northern and the north-eastern mountainous region, ii) the foothills, iii) the western desert, iv) the central Jazīra region (the Upper Mesopotamian Plain or UMP) and v) the southern lowlands (the Lower Mesopotamian Plain or LMP) (Engel and Brückner, 2018).

The LMP coincides with the southern part of the MP, between the latitude of $32^{\circ}30'00''$ N and $29^{\circ}50'00''$ N and the longitude of $44^{\circ}00'00''$ E and $49^{\circ}30'00''$ E (**Figure 1**). Here, different sub-environments such as freshwater lakes, brackish water lakes, saline lakes and their surrounding

marshes (locally called *Ahwar*), anastomosing and meandering rivers, distributary channels, irrigation canals, levees above the floodplain up to 3-4 meters and crevasse splays occur (Aqrawi, 1995; Jotheri, 2016; Engel and Brückner, 2018), shaping the landscape so much that is better defined as waterscape. Not surprisingly, the *Ahwar* is protected by UNESCO since 2016, as a refuge of biodiversity and the relict landscape of the Mesopotamian cities and where one of the world's largest inland delta system develops (<https://whc.unesco.org/en/list/1481/>). Moreover, the areas without alluvial influence, due to channel migration or channel siltation, are characterized by arid landforms like sand dunes, deflation basins and salt flats (Yacoub, 2011; Engel and Brückner, 2018)

3.1 Geological setting

The Iraqi territory can be distinguished into four main tectonic zones based on the type and the age of the rocks, on their thickness and their structural evolution:

- Inner Platform,
- Outer Platform,
- Zagros Suture Zone,
- Shalair Zone.

The Inner and the Outer platforms belong to the Arabian Plate, which is in subduction under the Eurasian (Iranian) Plate, while the last two zones coincide with the northeastern sector of the Arabian Plate (i.e., Iraq). The collision generated a foreland basin mainly in the Outer Platform, where other four zones are recognized: i) Imbricate Zone, ii) High Folded Zone, iii) Low Folded Zone (which make up the Zagros fold-and-thrust Belt) and the iv) Mesopotamian Foredeep (**Figure 1**) (Fouad, 2010; Sissakian, 2013).

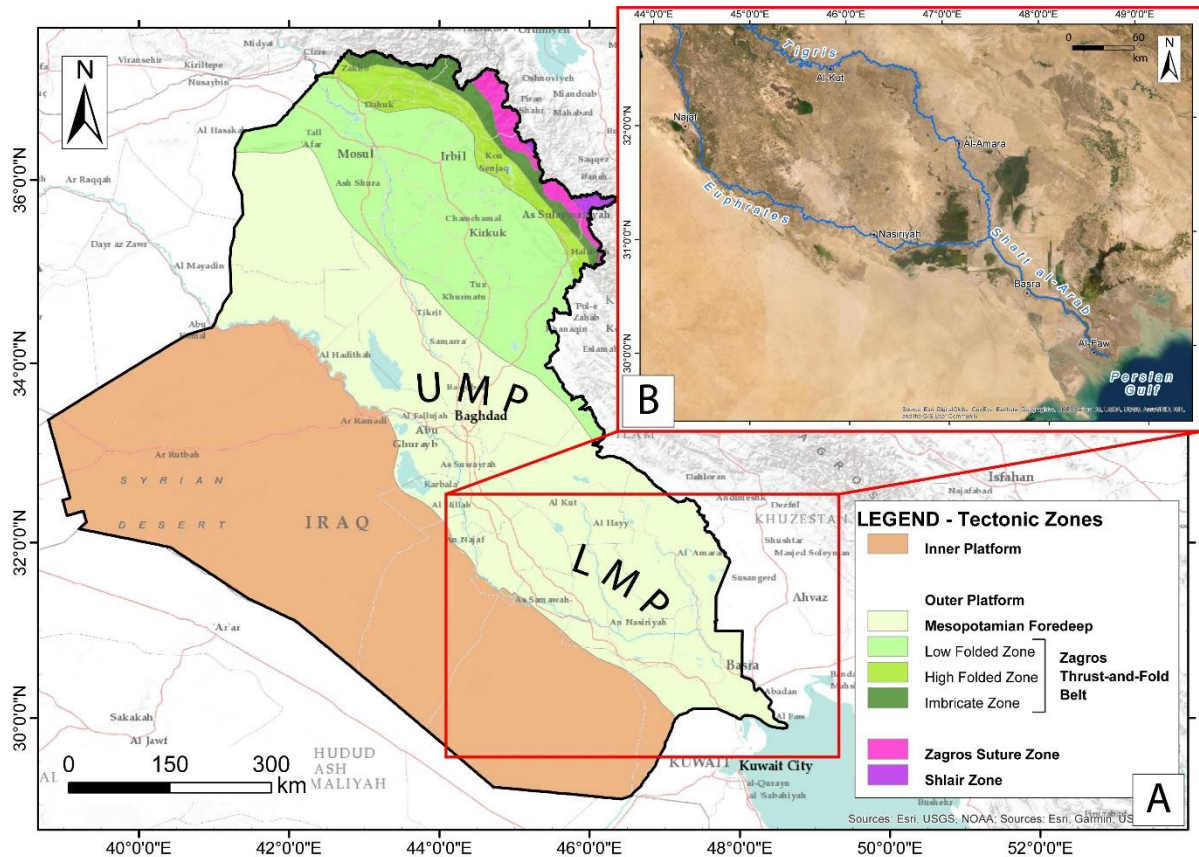


Figure 1 - The Iraqi territory subdivided into its main tectonic zones, modified from Sissakian 2013 (Figure A), and the study area corresponding to the LMP, detailed in Figure B with a satellite nadir view from TerraColor satellite imagery.

The Inner Platform is the sector with the lowest tectonic deformations and coincides with the Iraqi Southern and Western Deserts. The Quaternary deposits are not well developed, except for the Pleistocene fluvial terraces of the Euphrates River, the Holocene floodplain deposits of the Euphrates River and the aeolian deposits of the eastern margin (Sissakian, 2013).

Instead, the most tectonically-deformed sector is in the northeastern area of the Outer Platform, where the west-verging thrust-and-fold belt of the Zagros Mountains has been developed since the late Cretaceous, when the Late Alpine Orogeny started because of the collision between the Arabian Plate and the Iranian Plate. The southwestward decrease of the deformation intensity leads to reducing the amplitude of the anticlines (Sepehr and Cosgrove, 2004; Sissakian, 2013).

The Mesopotamian Foredeep includes the LMP, the UMP, the northernmost area known as Jazira Plain and the Persian Gulf, extending totally from the northeastern area of Syria up to the Straits of Hormuz (Evans, 2011; Sissakian, 2013; Garzanti et al., 2016). Most of the Mesopotamian foreland's sediments derives from the erosion of the Anatolia-Zagros composite orogen, perfectly reflecting the lithology of the source area, and scarcely altered by the chemical weathering of the arid climate (Garzanti et al., 2016). The area is lesser tectonically disturbed, compared to the Zagros thrust-and-fold belt, and rather flat with the height decreases from the northwest to the southeast, where reaches zero elevation in the tidal plane of the Persian Gulf (Sissakian, 2013).

The Tigris and Euphrates Rivers drain axially the MP, the central and the southern parts of the Mesopotamian Foredeep where a thick alluvial sequence is deposited mainly during the Quaternary, which maximum thickness of about 180 m is reached near Basrah (Sissakian, 2013; Jotheri, 2016; Milli and Forte, 2019). As reported by Aqrawi (2001), one of the main factors controlling the facies distribution in any basin is the climate, as well as the sea-level changes, sedimentation rates and

tectonism. Indeed, the sediments that compose the stratigraphic sequence of the whole MP are principally the Pleistocene-Holocene infill fluvial, deltaic and lacustrine deposits, mainly of the Tigris and Euphrates rivers, in addition to the estuarine, marine and aeolian sediments deposited during the Holocene, showing a wide range of environments that are prevalently made up of sand, silt, loam and clay (Yacoub, 2011; Milli and Forte, 2019). During the late Pleistocene and Holocene, the morphodynamics of the LMP has been strongly influenced by climate change of different intensity and duration, as well as by Holocene sea level oscillations. In particular, the early-mid Holocene sea-level rise produced a general inland, northward migration of the Persian Gulf shoreline to which followed, during late Holocene, a continuous seaward migration of the shoreline due to the Tigris and Euphrates delta progradation, in addition to a slight sea-level fall of about 2-3 m (Lambeck, 1996; Kennett and Kennett, 2006).

The Quaternary stratigraphy can be subdivided into three main units, based on their age: i) Pleistocene Unit, ii) Late Pleistocene - Early Holocene Unit, iii) Mid - Late Holocene Unit (Yacoub, 2011; Milli and Forte, 2019). The Pleistocene Unit is composed by fluvial and alluvial fan deposits made of gravels and sandy gravels alongside the marginal sector of the MP, sands, silt, and silty clay in the central part of the plain. Pluvial and inter-pluvial phases, corresponding to the glacial and interglacial phases, are well preserved in addition to several subaerial unconformity surfaces due to the glacioeustatic sea-level oscillations, as supposed by Milli and Forte (2019).

The Holocene stratigraphic succession is composed by a 15-20 m thick terrigenous sediment sequence made up of sandy layers intercalated with silt and mud, which testify the above-mentioned range of environments (Aqrawi, 2001; Yacoub, 2011; Milli and Forte, 2019). The Holocene sediments can be sub-divided into five different units: the Units 1, 2 and 3 are Lower-Middle Holocene in age, while the Units 4 and 5 are Upper Holocene in age.

- i. *Unit 1* is the ancient marsh/lacustrine silty sand, rich in organic matter. This Unit predominantly occurs in the central MP, merging laterally into the fluvial-plain deposits eastward and the playa evaporitic deposits westward (Aqrawi, 2001; Milli and Forte, 2019);
- ii. *Unit 2* is quite like *Unit 1*, but the gypsum, the authigenic dolomite and the palygorskite are abundant and clearly show the prevailing of the lacustrine environment during arid climate (Aqrawi, 2001);
- iii. *Unit 3* (known as *Hammar Formation*) represents the estuarine brackish/marine environment, characterised by a transgressive surface, which age varies between Lower (in the area of Al-Faw and Abadan) and Middle Holocene in the proximity of Nasiriyah and Al-Amara. Its thickness varies between 5-12 m and different environments can be identified: the transgressive sub-unit 3a is composed of shelly deposits and authigenic brackish water dolomite; the upper sub-unit 3b is made of grey marine clayey silts rich in foraminifera and ostracods; the sub-unit 3c represents the coastal marsh/intertidal environment with silty clay, while the last sub-unit 3d preserves sabkha characteristics with gypsum evaporite well preserved especially in the western sector of the plain (Aqrawi, 2001; Milli and Forte, 2019). The last two sub-unit clearly point out marine regression (Aqrawi, 2001); as well as the occurrence of mixing freshwater and marine fauna suggests the marine ingression during the Mid Holocene (Milli and Forte, 2019). More in detail, during the late Pleistocene - early Holocene, a wide fluvial system prevails in the area, while the sea-level was below the present one as much as about -120 m, thus the Persian Gulf shoreline at that time was southward than the modern one and was rapidly and continuing moving northwards (Lambeck, 1996; Anderson et al., 2007). The Ur-Shatt River is an incised canyon reaching the head of the Oman Gulf, formed by the last glaciation downcutting in the sea lowstand

condition and now completely submerged. From the peak of the last glaciation until about 14,000 yrs BP, the Gulf was completely in sub-aerial condition. After that, it was flooded with an estimated rate of about 10-11 mm/yr until about 9000 yr BP (i.e., about 1000 m/yr for the landward migration of the shoreline) (Teller et al., 2000; Anderson et al., 2007; Milli and Forte, 2019). Since 9000 yr BP to 7000 yr BP, the inland ingression rate decrease, reaching a value of about 3 mm/yr (Milli and Forte, 2019). During the mid-Holocene, specifically at 6000 yrs BP, the shoreline was at the maximum inland ingression, located between the modern cities of Nasiriyah and Amarah (Kennett and Kennett, 2006; Milli and Forte, 2019 and references therein); consequently, during the shoreline transgression, tides flooded the existing valleys, the depositional environment shifted from fluvial to estuarine shallow-marine-lagoon where a tidal plane developed (Bogemans et al., 2017a; Bogemans et al., 2017b; Milli and Forte, 2019). Particularly, in agreement with Lambeck (1996), during the maximum inland ingression, sea-level was higher than the present-day of about 2-3 m in the area of Al-Faw. The marine transgression occurred in a wetter climate condition, while the successive semi-arid climate shifting likely favoured the formation of supratidal flat like sabkhas (Aqrawi, 2001). The estuarine environment lasted until the fluvial progradation restarted due to a “bird-foot” delta formation, producing a relative sea-level regression, up to the present-day position (Bogemans et al., 2017a; Bogemans et al., 2017b). The exact position of the maximum inland shoreline ingression at 6000 yrs BP is still discussed as well as the timing of its mid-late Holocene southward migration. Nonetheless, in agreement with Jotheri et al. (2018), the marine transgression never reached the Uruk area (about 300 km far from the present shoreline).

- iv. During the late Holocene, the continental sedimentation prevailed: the deposition of *Unit 4* occurred with the fluvial/lacustrine plain mud (i.e., clayey silt and silty clay deposits). This unit is deposited during the seaward progradation of the Tigris-Euphrates delta system, which was rapid between 6000 and 4000 yrs BP, due to the wetter climate conditions, whereas it slowed significantly between 4000 and 3000 yrs BP because of the increase in aridity (Aqrawi, 2001; Kennet and Kennet, 2006; Milli and Forte, 2019).
- v. Finally, *Unit 5* is composed of three cyclical layers (i.e., clayey silt of brackish/marine deposits with foraminifera and ostracods, clayey silt with mollusc shells, and organic-rich sandy silt), corresponding to the brackish shallow water environment, successively infilled by fluvial sediments of Tigris and Euphrates rivers and lastly filled by aeolian sediments. Their radiocarbon dates point out the relative youth of Unit 5, approximately of about 2500 yrs BP (Aqrawi, 2001; Milli and Forte, 2019).

Each before described unit is the result of specific depositional environments and diagenetic processes, which shift between them is mainly linked to the changes in climatic conditions (Aqrawi, 2001). Indeed, after the last glaciation arid and semiarid conditions prevailed almost for the Early Holocene, as pointed out by the gypsum formation within the calcareous fluvial mud. During the mid-Holocene marine ingression, the climate shifted towards wetter conditions and they persisted until about 5000 – 4000 yrs BP, when more severe aridity occurred and still preserves (Aqrawi, 2001; Kennet and Kennet, 2006).

3.2 Holocene and present climate of the MP

The climate of the Tigris-Euphrates Basin is principally influenced by the large-scale circulation patterns, teleconnections and regional topography (Bozkurt and Sen, 2013). The highlands of these

rivers correspond to the Taurus Mountains and the Anatolian Highlands, where the winter rainfall from eastward propagating mid-latitude cyclones are captured by this orography. About 650 mm/yr of precipitations fall over Turkey, with the highest value along the eastern coast of the Black Sea (i.e., 2000 mm/yr) and the lowest value in the central Anatolian region (i.e., 350 mm/yr) (Cullen and deMenocal, 2000).

These Turkish rainfalls are mainly generated by the mid-latitude cyclones in the Atlantic Ocean and the eastern Mediterranean seas (Cullen et al., 2002). The Atlantic Ocean is influenced by a large-scale anomaly that influences the variability of the local atmospheric circulation: the North Atlantic Oscillation (NAO). The NAO is the main responsible for the variance in sea-level pressure and the rainfalls and temperature variability in Europe and the Mediterranean area. Since the NAO is extremely regional, an NAO index has been defined based on the surface sea-level pressure difference between the Subtropical (Azores) High and the Subpolar (Icelandic) Low (Cullen et al., 2002; <https://www.ncdc.noaa.gov/teleconnections/nao/>). When the Icelandic Low (IL) is lower than normal, the Azores High (AH) is higher than normal, and this enhances the pressure gradient, resulting in a positive NAO (+NAO). The negative NAO (-NAO) reflects the opposite pattern. During the +NAO, the winds and the winter storms are stronger, increasing the temperatures of northern Europe, Scandinavia and the east coast of North America, while in Greenland, the southern Europe and up to the Middle East the temperatures decrease, and drier conditions occur. Opposite patterns of temperature and precipitation occur during the -NAO (Cullen et al., 2002; <https://www.ncdc.noaa.gov/teleconnections/nao/>). As supposed by Mann (2002), the interdecadal-centennial scale variability of the NAO may play a key role in the Holocene climate variability of the Middle East. The NAO controls the Atlantic heat and moisture fluxes into the Mediterranean region, where the winter cyclones that feed the Middle East rainfalls and river runoff develop; thus, NAO-related changes in Atlantic westerly heat/moisture transport and Atlantic/Mediterranean sub-surface temperature can modify the Middle Eastern climate (Cullen et al., 2002).

The MP is located within the subtropical high-pressure belt, where an arid to semiarid climate prevails with strong seasonality in both precipitation and temperature (**Figure 2**). The Mediterranean winter rainfalls reach the UMP and, minimally, the LMP mainly during the winter season; instead, the Subtropical High replaces the moist westerlies during the summer season, inducing hot and dry conditions, in addition to a persistent northwest wind known as *Shamal* (Cullen et al., 2000; Engel and Brückner, 2018). Besides, this high pressure frequently induces severe dust storms and heat waves (Kennet and Kennet, 2007). The mean annual rainfalls in the UMP ranges from 400 to 150 mm/yr, while in the LMP the annual rainfalls decrease to 140 mm/yr (Engel and Brückner, 2018).

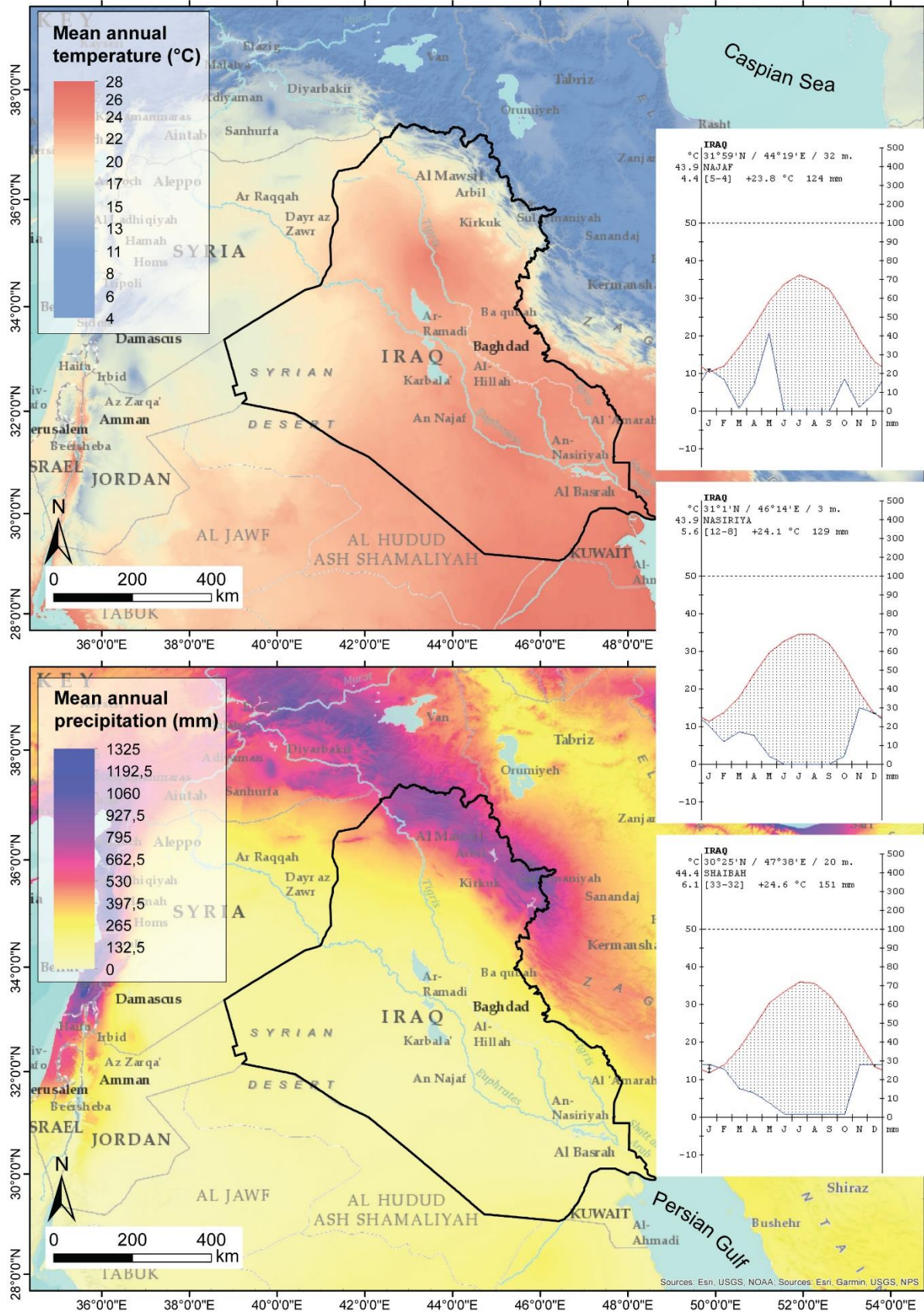


Figure 2 - WorldClim 2.1 climate data for 1970-2000 with spatial resolution of 30 seconds (~1 km²) and climate diagrams of Najaf, Nasiriyah and Shaibah (i.e., Basrah) from the Worldwide Bioclimatic Classification System (from Rivas-Martinez and Rivas-Saenz, 2017).

Besides the considerable number of geo-bio-archives in the north and west Mesopotamia heartland, such as the marine records of the eastern Mediterranean and northern Red Seas, and the Mirabad and Zeribar lake records in the Zagros Mountains (e.g., Stevens et al., 2001; Wick et al., 2003; Wasylkova et al., 2006; Stevens et al., 2006; Jones and Roberts, 2008; Bar-Matthews et al., 2011; Engel et al., 2012; Zanchetta et al., 2014; Talebi et al., 2016; Andrews et al., 2020), their proxy data are not suitable for reconstructing the LMP climate conditions during the Holocene (Engel and Brückner, 2018).

Anyway, a key site for determining the Late Pleistocene - Holocene climate evolution in the eastern Mediterranean and Near East is the Lake Van (eastern Taurus Mountains), which climatic regimes can be approximated to the Mesopotamian ones and which sensibility to climatic fluctuations is strongly connected to changes in the jet stream and the subtropical high-pressure belt. Lake Van's data show high $\delta^{18}\text{O}$ values during the Younger Dryas and the earliest Holocene, meaning the occurrence of very arid conditions up to around 10,500 cal. BP. Since the Early Holocene, the moisture availability gradually increased, most likely due to three main factors, such as the African Summer Monsoon eastward penetration, the winter-spring tropical plumes crossing the Red Sea or the Mediterranean winter rains (Enzel et al., 2015; Gaugnin et al., 2016; Engel and Brückner, 2018). Wetter conditions began during the Early to Mid-Holocene transition, leading to a climatic optimum among 6,200 - 4,000 cal. BP, as well-recorded by Lake Van and also confirmed with a slight shift by Soreq Cave (8,500 - 7,000 yrs BP) and Jeita Cave (9,200-6,500 yrs BP) (Bar-Matthews et al., 1999; Verheyden et al., 2008; Zanchetta et al., 2014; Engel and Brückner, 2018) (**Figure 3**). Indeed, a Holocene thermal optimum is recorded by many regions around 9.0 - 5.5 ka BP (Roberts, 2014). An even more significantly drier conditions occurred around 4,200 - 4,000 cal. BP, reflecting the climatic desiccation between 6.5 and 4.5 ka BP that created the modern Saharan, Arabian and Thar deserts (Wick et al., 2003; Roberts, 2014; Engel and Brückner, 2018) and suggesting the suppression of the monsoonal circulation system which controls tropical rainfall and the decline of the winter Mediterranean rains (Roberts, 2014).

3.3 Geomorphology of the MP

The MP can be considered as a wide aggradational geomorphological unit, where depositional landforms of fluvial, lacustrine and aeolian morphogenesis prevail, whereas estuarine and marine landforms are frequent in the southeasternmost sector of the plain. The topography is rather flat with an undetectable gradient from northwest to the southwest (i.e., about 1 m/20 km), despite the micro-relief due to levees, archaeological mounds or aeolian sand dunes occur randomly (Yacoub, 2011; Sissakian et al., 2020 a).

The Tigris and the Euphrates built up the plain mainly during the Holocene, favouring channel processes which formed levees above the floodplain, meanders, scrollbars, oxbow lakes, crevasse splays, distributary channels and marshes (Jotheri, 2016). Within the MP, the Euphrates has no tributaries whereas the left bank of the Tigris is fed by perennial and seasonal tributaries that originate in the Zagros Mountains, such as Adhaim, Diyala, Badra, Djangalah and Tib rivers (Aqrawi et al., 2006; Bozkurt and Sen, 2013). Thus, the fluvial landforms are the most common in the area, where the strong seasonality of the Tigris-Euphrates' streamflow and the relative sea-level fluctuation of the Persian Gulf mainly drive the morphoevolution of the plain (Verhoven, 1998; Morozova, 2005, Engel and Brückner, 2018).

In addition to the extremely variable streamflow, the main rivers, as well as the numerous distributaries, are subjected to changes in their pattern and behaviour due to different factors such as channel gradient and confinement, grain size and sediment supply, riverside vegetation and human impacts (Schumm, 1981; Blum and Törnqvist, 2000; Jotheri, 2016). Indeed, the UMP is largely characterized by broad terraces, marginal alluvial fans and sandy-gravel floodplains as Pleistocene relict deposits, while in the LMP the meandering Tigris and the anastomosing Euphrates develop a sandy-clay floodplain, leaving the central plain rather abandoned. In the central LMP, the Euphrates-Tigris-Karun system developed a wide fluvio-lacustrine deltaic complex during the Holocene, which is today covered by shallow fresh-brackish water lakes and marshes, locally called *Ahwar* (Aqrawi et al., 2006; Yacoub, 2011; Engel and Brückner, 2018). The Tigris and Euphrates, joining about 170 km inland from the present-day shoreline of the Persian Gulf, form the Shatt al-Arab River, which creates the Shatt al-Arab/Karun estuary system and a tidal flat width 1-2 km (Aqrawi et al., 2006; Yacoub, 2011; Al-Ameri and Briant, 2019).

Considering the marginal sectors of the MP, the first geomorphological unit is represented by the alluvial fans. The northern sector of the UMP is occupied by four widespread alluvial fans, which areal extension varies by several thousand kilometres. Al-Fatha Fan is the northernmost ones, extending from Al-Fatha up to Al-Falluja and reaching the north of Baghdad. Its sediments can be distinguished into two main lithological units: the lowermost is mostly gravel and conglomerate, while the uppermost is mainly composed by gypcrete and gypsiferous clastics (Sissakian et al., 2020 b). The surface is broadly undulated, where deranged depressions and shallow valleys frequently occur, reflecting the high porosity of the alluvial fan (Yacoub, 2011). Al-Adhaim Fan is a large alluvial fan built up by the Al-Adhaim River, which deposited fine sand, silt and lenses of fine conglomerate in the lowermost layer, whereas the uppermost deposit is composed by gypcrete. The Diyala River deposited the alluvial fan of the same name, which stratigraphy is quite similar to the Al-Adhaim ones. Finally, the Ramadi Fan is one of the Western Alluvial Fan System of the MP, deposited by the Euphrates River prevailing the longitudinal development because of the topography. As for the other fans, the stratigraphic units are quite similar (**Figure 4A**) (Sissakian et al., 2020 b). The Eastern sectors of the UMP and partially LMP are fringed by several coalescent alluvial fans, alongside the foothill slopes

between Mandali and Al-Amara, forming a continuous belt of bajada. Their dimensions are extremely variable between a few kilometres up to hundreds of square kilometres (**Figure 4B**) (Yacoub, 2011; Sissakian et al., 2020 b). Finally, the western and south-western sector of the LMP is also fringed by several alluvial fans, such as Karbala-Najaf Fan, Dibdibba Fan, Al-Slaibat Fans and Al-Batin Fan, whose catchment area is in the Western Desert. The Western and Southern Alluvial Fans System is somewhere buried beneath the MP deposits and is developed along the Euphrates Boundary Fault, where the gradient considerably drops, revealing the key role of tectonism in its development (**Figure 4C,D**) (Aqrawi et al., 2006; Yacoub, 2011; Sissakian et al., 2020 a, b).

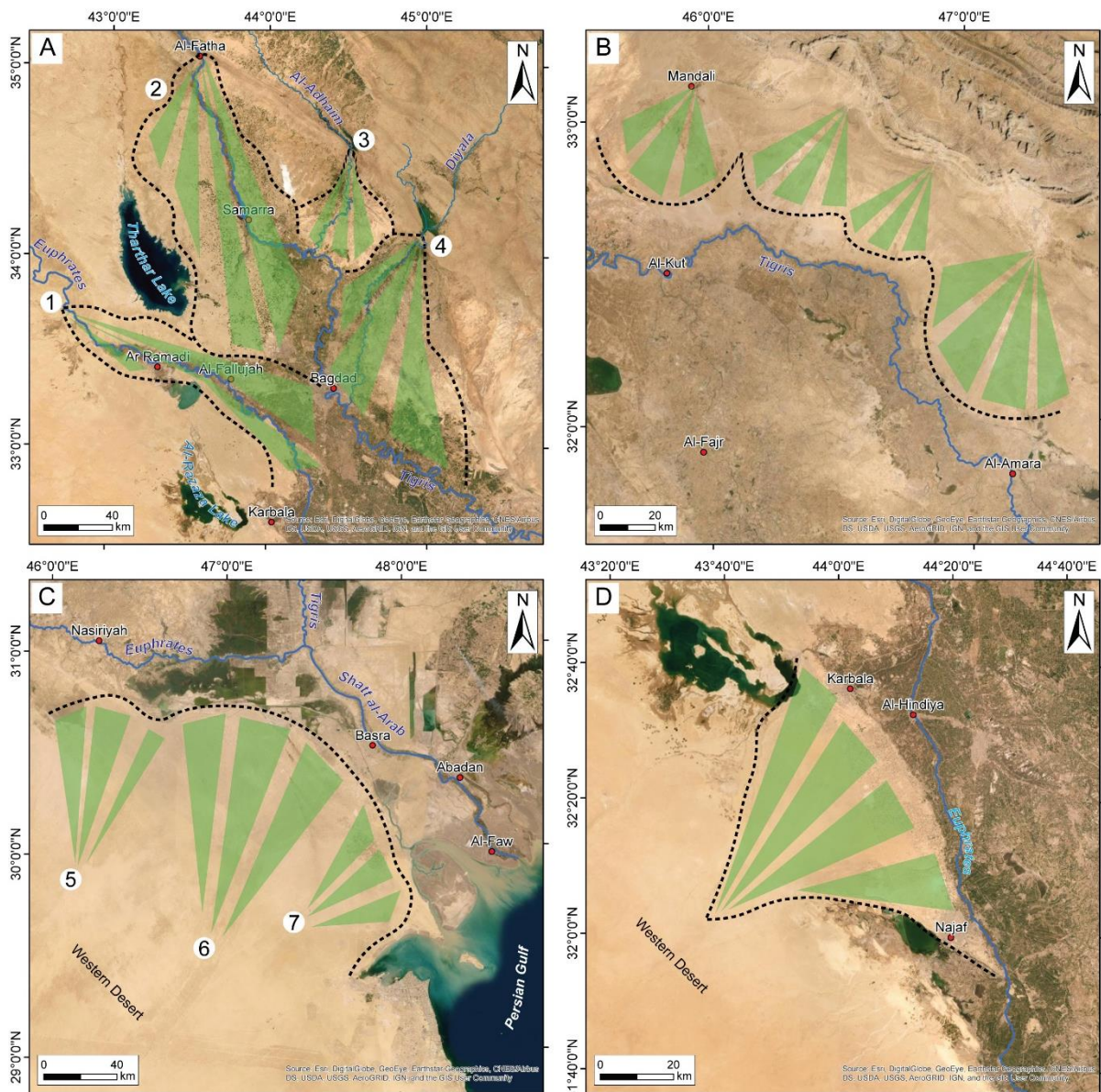


Figure 4 - The fringed alluvial fans of the MP. A) The Northern alluvial fans: 1.Ramadi Fan; 2.Al-Fatha Fan; 3.Al-Adhaim Fan; 4.Diyala Fan. B) The coalescent alluvial fans of the Eastern sector. C) The southernmost alluvial fans: 5.Al-Slaibat Fan; 6.Al-Batin Fan; 7.Dibdibba Fan. D) The western Karbala-Najaf Fan.

The floodplains of the major rivers like Euphrates, Tigris, Shatt al-Arab and the eastern foothill rivers are the main morphological unit in the MP. Thus, most of the study area can be classified as a floodplain, despite the historical anthropogenic interference over watercourses as well as the flood management since the second half of the 20th century strongly interfered with the natural conditions (Altinbilek, 2004; Rost, 2017; Rateb et al., 2021). Each floodplain is continuously constructed and

eroded, preserving three main kinds of landforms: the channel deposit (i.e., meandering belt, levees, scrollbars), the overbank deposit (i.e., crevasse splays and backswamps) and the transitional deposit such as channel fill (Allen, 1965; Verhoven, 1998; Yacoub, 2011).

Indeed, one of the most frequent fluvial processes in the MP are the avulsion processes, which consists of an abrupt shift of the whole channel belt from one location to another, favouring the formation of a new watercourse (Allen, 1965; Bridge and Leeder, 1979; Jones and Schumm, 1999; Bridge, 2003; Slingerland and Smith, 2004; Bridge and Demicco, 2008; <https://www.nationalgeographic.org/encyclopedia/overbank-deposits/>). This process mainly occurs during flood events and requires the bed of the new course being topographically lower than the old channel belt (Bridge, 2003, Bridge and Demicco, 2008). This implies a supra-elevation of the older channel belt above the floodplain, a condition that requires net aggradation of the channel for a long period of time (Leeder, 2011). As the inception of the avulsion process requires an energetic water flow, it is quite logical to consider this process connected with the widening of a channel on a crevasse splay, although the intersection of the main channel with an existing channel can favour avulsion (Bridge and Demicco, 2008). So, crevasse processes and deposits and their associate landforms represent important geomorphological features for understanding the fluvial morphodynamics in lowland areas and provide evidence for the mechanism of avulsion (Smith et al., 1989; Smith and Pérez-Arlucea, 1994; Bristow et al., 1999; Slingerland and Smith, 2004; Buehler et al., 2011; Hajek and Wolinsky, 2012; Bernal et al., 2013; Kleinhans et al., 2013; Yuill et al., 2016). A crevasse splay typically shows a lobate sediment accumulation area, fan-shaped in plan with an upward convexity and contain a system of a distributive multi-channel system (Goudie, 2004; Aslan, 2006). The fluvial avulsion begins and develops when flooding waters break through a high-topographic levee at the time of peak flood discharge or when the bankfull discharge overtops the levees. The sediment deposition occurs when the flow decelerates, passing from confined to unconfined conditions (i.e., from distributive crevasse channels in the proximal sector to lobe deposits in the middle and distal sectors), or when the flooding water enters a standing waterbody (Miall, 2006; Yuill et al., 2016; Burns et al., 2017; Van Toorenenburg et al., 2018). The crevasse splay deposits usually consist of very fine to medium-grained sands. These deposits are coarser and thicker in the proximal portion, where sharp and erosional-based structureless or medium-scale cross-bedding (dune) sand units occur (channel-bar and channel-fill deposits). Finer and thinner deposits occur in the middle and distal sectors, where cross-laminated sand (essentially climbing-ripples strata) with load structures pass downcurrent to structureless finer sand and silt deposits, and finally to the floodbasin mudstone (Bridge, 2003; Bridge and Demicco 2008; Burns et al., 2017; Gulliford et al., 2017). Generally, these deposits are vertically organized, forming coarsening to fining upward successions that reflect the increase and the decrease of flood energy during deposition. The variation of grain-size both parallel and perpendicular to flow direction (i.e., across strike and down dip) is attributed to the decrement of floodwater energy, which is in turn related to flow expansion away from the crevasse channel (Burns et al., 2017; Gulliford et al., 2017). All these processes develop during the life cycle of a crevasse splay (Van Toorenenburg et al., 2018) in which the floodplain gradient plays a relevant role. It acts, in fact, as the base level for the crevasse channels, adjusting towards a graded equilibrium profile. Therefore, at the beginning of the cycle, the outflow of floodwater promotes erosion near the proximal sector and deposition in the middle and distal sectors of the crevasse splay (Van Toorenenburg et al., 2018). The continued erosion in the crevasse proximal suggests that this sector essentially represents a by-passing zone, that becomes a depositional zone during the waning stage of flooding. When the return flow of floodwater allows sediment deposition into the crevasse channels (backfilling), a decrease of the floodplainward gradient occurs, deactivating the crevasse splay (Van Toorenenburg et al., 2018). All these data evidence that a

crevasse splay is a composite body, made up of stacked vertically and laterally single splays deposited by single flooding events and organized with a typical progradational trend (Van Toorenenburg et al., 2018; Gulliford et al., 2017). These composite bodies are generally 3-4 m thick, up to 10 km long and 5 km wide, and may reach several square kilometres (Miall, 2006; Burns et al., 2017; Gulliford et al., 2017), depending generally on sediment grain-size and floodplain-drainage conditions (Van Toorenenburg et al., 2018; Millard et al., 2017, Nienhuis et al., 2018). Crevasse splays are particularly important landforms of the anastomosed fluvial environment, as their formation represents an intermediate step in the avulsion of the main channels into new positions on the floodplain (Yuill et al., 2016; Van Toorenenburg et al., 2018; Nienhuis et al., 2018). The floodplain sectors surrounding crevasse splays were the zones where the earliest human settlements established and developed. An outstanding example is the Mesopotamian Plain (hereafter MP) where, thanks to the fluvial avulsion process and the development of the associated landforms, the Akkadian civilization found the ideal conditions for introducing the first agricultural techniques (Roberts, 2014).

In the UMP, the Euphrates floodplain is entrenched between two erosional scarps, with a width of 8-10 km. It is very close to the Tigris River, which floodplain is narrower and bounded by scarps; moreover, the Tigris floodplain preserves several oxbow lakes between the cities of Bagdad and Numaniya (**Figure 5A**). Both rivers flow meandering thanks to a low gradient and in proximity up to the city of Karbala, where the Euphrates diverges westward and the two rivers move away. In the LMP, the Euphrates pattern becomes anastomosing, with significant distributaries such as the Shatt al-Hilla and others between Najaf and Samawa cities; so, the Euphrates floodplain widens, developing a complex system of distributaries, sub-flood basins and related irrigation canals (**Figure 5B**). From Samawa, the southern sector of the floodplain still preserves the abandoned meandering watercourse of the Euphrates, with associated relict landforms such as scrollbars, point bars, levees, and crevasse splays (**Figure 5C**). The abandoned Euphrates watercourse is also recognizable southward the Hammar Lake, suggesting that it was an outflowing river. As reported by Yacoub (2011), the eastward migration of the Euphrates can be linked to the subsidence toward the centre of the plain. Instead, the Tigris of the LMP preserves its meandering pattern, even if the Shatt al-Gharraf and the abandoned Dujaila channels represent its main distributaries with a southward and an eastward direction, respectively (**Figure 5D**). Like the Euphrates distributaries, the Tigris' ones develop several levees, crevasse splays and local flood basins, which are still active only along the Shatt al-Gharraf. Before reaching the Al-Amara city, the Tigris bifurcates, losing much of its sediment supply and discharge into the lacustrine delta of the Huwaizah Marshes. Even the lowermost reach of the Euphrates floodplain is occupied by wetlands. Indeed the northernmost Euphrates branch flows between the Central Marshes and the West Hammar, joining the Tigris at Al-Qurnah city and forming the Shatt al-Arab River, while the southernmost Euphrates branch flows into the West Hammar and south of the East Hammar, joining the Shatt al-Arab near the Garimat Ali town (**Figure 6**) (Verhoven, 1998; Yacoub, 2011; Jotheri, 2016; Sissakian et al., 2020 a).

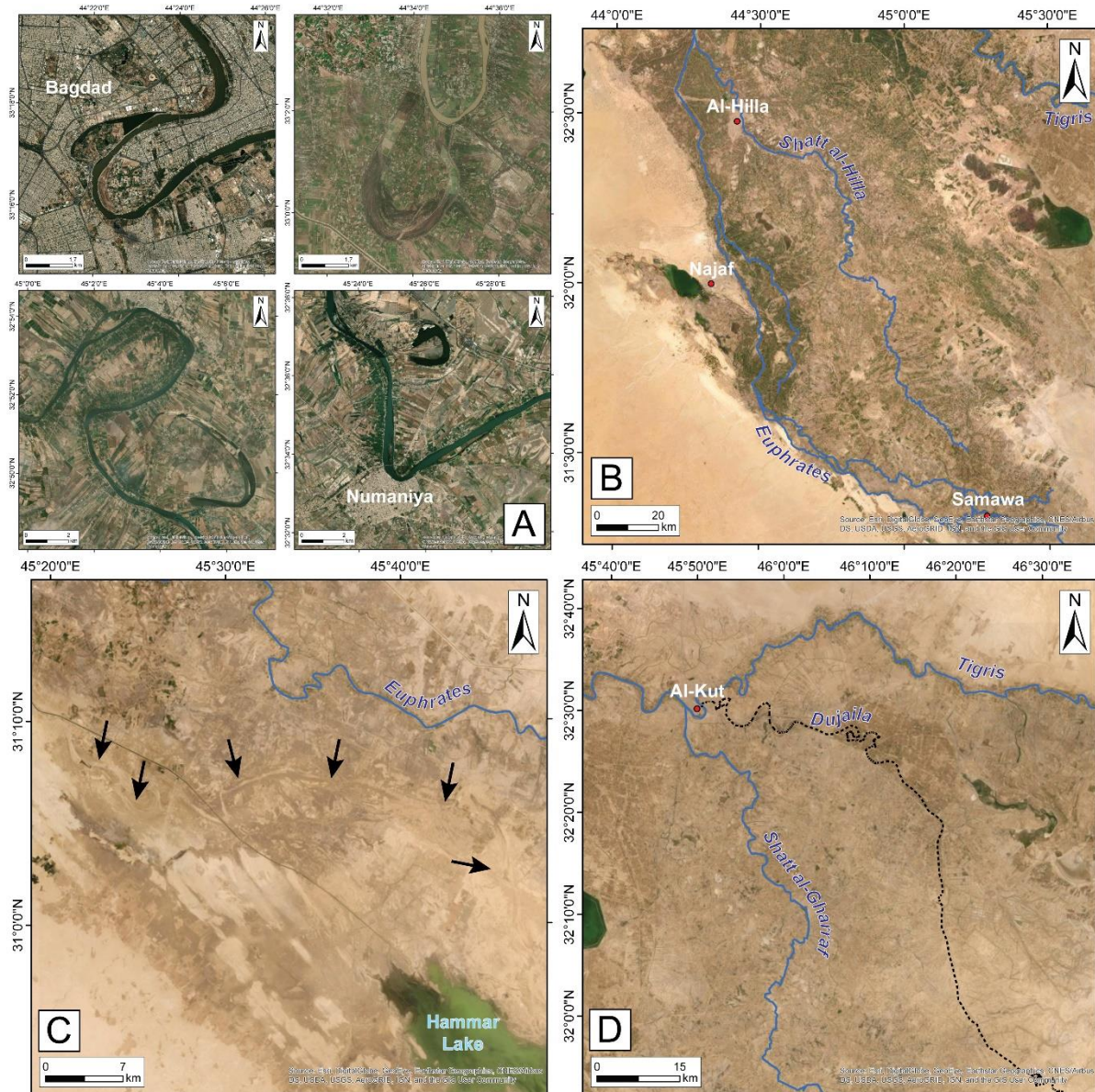


Figure 5 - A) The oxbow lakes of the Tigris between Bagdad and Numaniya. B) The anastomosing pattern of the Euphrates and its main distributary, the Shatt al-Hilla. C) The abandoned course of the Euphrates north of Hammar Lake, pointed out by black arrows. D) The Tigris' distributaries, the active Shatt al-Gharraf and the traces of the abandoned Dujaila.



Figure 6 - The Ahwar area of the LMP.

The Shatt al-Arab floodplain is characterized by a very smooth meandering pattern with levees of about 1 m of height. The uppermost sector is surrounded by the western marshes (i.e., the East Hammar) and a shallow flood basin eastward; from Basra, the lowermost reach passes into the estuarine sabkhas of the western side while the eastern bank is occupied by the Karun River floodplain, which joins with the Shatt al-Arab near Khorramshahr town. Downstream of Basra, the Shatt al-Arab mouth is affected by the Persian Gulf tides, which vary between 1 and 3 m (Yacoub, 2011; Jotheri, 2016; Sissakian et al., 2020 a).

Indeed, the southernmost sector of the MP is occupied by a wide tidal flat (i.e., about 10,000 km²), where numerous tidal creeks occur into the coastal muddy shore. The active tidal zone is about 2 km width, but the super-tides reached 10 km landward before the construction of embankments along the coast. The dendritic pattern of Khor Al-Zubair and Bandar-e Emam Khomeyni (in the Iranian territory) are the main examples of tidal creeks, where typically the channel width decreases landward and increases seaward, reaching up to 2 km (Figure 7) (Yacoub, 2011; Sissakian et al., 2020 a).

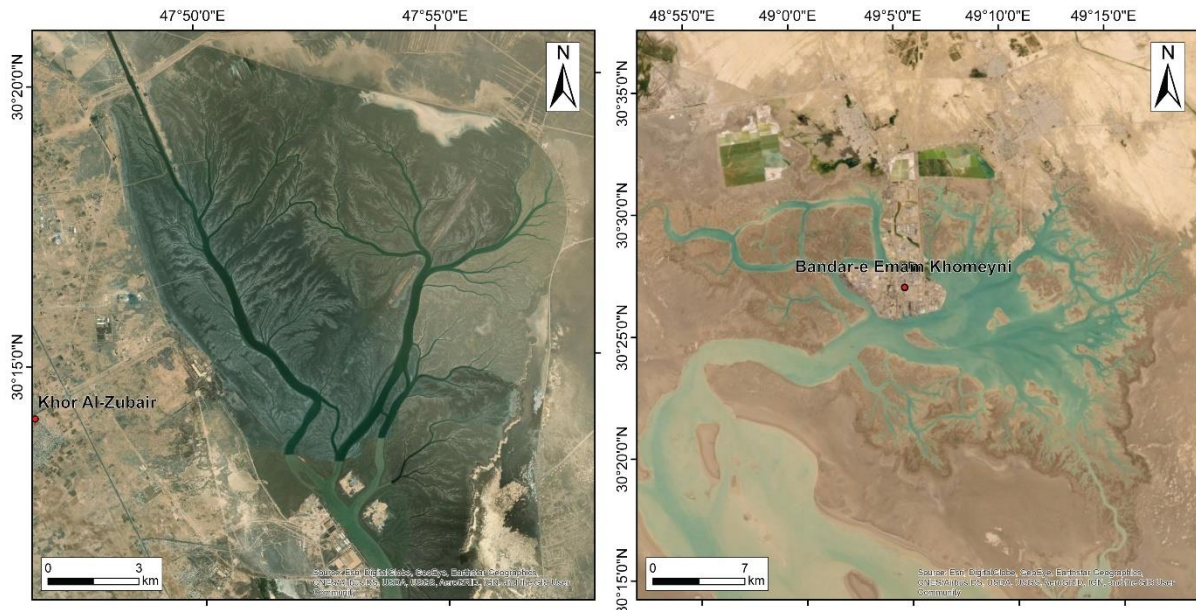


Figure 7 - The dendritic tidal creeks of the southern tidal flat.

The lacustrine-wetland unit is mainly represented by the marshes of the central LMP. They occupy shallow depression where a low sedimentation rate prevailed after the marine regression. Even if the continuous subsidence of the MP maintains these shallow water basins, many authors support the main influence of eustatism and deltaic progradation in the marshland development (Yacoub, 2011; Sissakian et al., 2020 a). At the beginning of the twenty-first century, many marshes have been dried due to the built of dams, canals, and reservoirs for energetic and agricultural purposes. Until the 1970s, the marshlands covered an area of about 20,000 km², but in the 1990s Saddam Hussein's regime drained large areas for punishing the participation of local tribes to the anti-government rebellions. Only after 2003, the marshlands slowly brought back to the natural conditions (<http://www.unesco.org/new/en/member-states/single-view/news/the-marshlands-of-iraq-inscribed-on-unescos-world-heritag/>; <https://earthobservatory.nasa.gov/world-of-change/Iraq>). The marshes depth varies between few decimetres up to 2-4 m; the shallowest depressions are frequently occupied by playas and sabkhas thanks to the intensive evaporation of the salty water. Where the depth is higher, brackish and freshwater conditions prevail, favouring the growth of vegetation (Yacoub, 2011; Sissakian et al., 2020 a).

Finally, the MP is also characterized by the Aeolian unit, that prevails where the fluvial-floodplain processes are cessed. The main landforms of this unit are the sand dune fields, mostly barchan type, and the sand sheets of hundreds of square kilometres (Yacoub, 2011; Sissakian et al., 2020 a).

4. Materials

In remote sensing, the energy emanated by the earth's surface is measured through a specific sensor mounted on a terrestrial platform, an aircraft or a spacecraft (Richards and Jia, 2006). Thus, the collected images are potentially useful for the researcher to investigate remote and inaccessible areas, where frequent warfare and political conflicts occur or when globally lockdowns are adopted by different countries for preventing a disease outbreak. Moreover, when the study area is particularly wide, the recognition of Earth surface processes and associated landforms encourages the application of remote sensing (Iacobucci et al., 2020).

Considering the vast variability of free-access datasets from different Earth's Observation missions, the Lower Mesopotamian Plain (LMP) has been investigated through the optical and multispectral data of Landsat Mission, while the Digital Elevation Models (DEMs) of the area have been obtained by two optical derived and freely available datasets with a ground-resolution of 1 arcsec (ca. 30 m cell⁻¹). Only the area surrounding the archaeological site of Tell Zurghul has been examined through an interferometric DTM obtained by elaborating the SPOT imagery of the Italian mission COSMO-SkyMed©.

In the following sections, the technical specifications and details of each sensor will be described, in addition to their derived products.

4.1 Landsat 8

It has long been known that alluvial deposits of different ages, like these of the Mesopotamian floodplain, can be distinguished using multispectral imagery, where different reflectance properties due to changes in chemistry, mineralogical composition and micro-relief are highlighted (Kahle et al., 1984, D'Arcy et al., 2018, Iacobucci et al., 2020). Therefore, multispectral imagery can be adopted for getting information about the types of sedimentary deposits and so for discerning landforms (D'Arcy et al., 2018, Iacobucci et al., 2020), while the availability of multispectral Landsat 8 satellite imagery for the LMP leads to carrying on the multispectral analysis and supervised classifications.

Indeed, Landsat imagery provides essential and useful information for different disciplines and applications such as the agribusiness, global change researchers, academia, state and local governments, commercial users, national security agencies, the international community, decision-makers, and the public. Landsat Project's mission provides repetitive acquisition of middle-resolution multispectral data of the Earth's surface. This project is the only source for global, calibrated, moderate spatial resolution measurements of the Earth's surface, preserved in a national archive and freely available. Data from the Landsat spacecraft constitute the longest record of the Earth's continental surfaces as seen from space (Ihlen and Zanter, 2019).

Landsat 8 is launched on February 11, 2013. First known as Landsat Data Continuity Mission (LDCM), it was created for investigating and researching feasible solutions to follow Landsat 7 mission. Since 1972, Landsat satellites have continuously acquired images of the Earth's land surface, providing uninterrupted data until today. Landsat 8 carries the Operational Land Imager (OLI) and the Thermal Infrared Sensor (TIRS). OLI works on nine spectral bands, including a panchromatic one, while TIRS works on the last two bands (**Table 2**) (Roy et al., 2014; Sekandari et al., 2020; USGS Landsat Missions). Besides its brief time life, Landsat 8 is one of the best multispectral satellites thanks to the eleven bands with high-resolution (Bull, 1991; Gillespie, 1992; Roy et al., 2014).

Table 2 - The spectral bands of the Landsat 8 sensors, OLI and TIRS, compared to the ones of Landsat 7 ETM+.

Landsat 7 ETM+			Landsat 8 OLI and TIRS		
Bands	Wavelength (µm)	Resolution (m)	Bands	Wavelength (µm)	Resolution (m)
			1	0.435 – 0.451	30 Coastal/Aerosol
1	0.441 – 0.514	30 Blue	2	0.452 – 0.512	30 Blue
2	0.519 – 0.601	30 Green	3	0.533 – 0.590	30 Green
3	0.631 – 0.692	30 Red	4	0.636 – 0.673	30 Red
4	0.772 – 0.898	30 NIR	5	0.851 – 0.879	30 NIR
5	1.547 – 1.749	30 SWIR-1	6	1.566 – 1.651	30 SWIR-1
6	10.31 – 12.36	60 TIR	10	10.60 – 11.19	100 TIR-1
			11	11.50 – 12.52	100 TIR-2
7	2.064 – 2.345	30 SWIR-2	7	2.107 – 2.294	30 SWIR-2
8	0.515 – 0.898	15 Pan	8	0.503 – 0.676	15 Pan
			9	1.363 – 1.384	30 Cirrus

The OLI sensor represents a significant technological advancement over Landsat 7 ETM+ sensor (Enhanced Thematic Mapper Plus). Indeed, OLI has 4-mirror telescopes which generate 12-bit data compared to the 8-bit data produced by the Thematic Mapper (TM) and ETM+. Each width of the OLI bands has been improved to avoid the atmospheric absorption which affected the ETM+ bands. Indeed, the OLI band 5 excludes the water vapour absorption at 0.825 µm, narrowing the wavelength from 0.772 – 0.898 µm of ETM+ to 0.851 – 0.879 µm. Moreover, the OLI Pan band has been also narrowed for enhancing the contrast between vegetated areas and zones without vegetation cover. Finally, the two new bands of OLI (i.e., band 1 and 9) has been added for improving the ocean colour observation and for detecting the cirrus clouds contained ice crystals (Ihlen and Zanter, 2019).

The TIRS is a push-broom sensor like the OLI, which measures the longwave Thermal Infrared (TIR) through the Quantum Well Infrared Photodetectors (QWIPs). These QWIPs can distinguish the two thermal infrared wavelengths emitted by the Earth's surface and the atmosphere, representing an advancement over the single-band thermal data of the Landsat 7. The TIRS sensor collects imagery quantized to 12 bits and with a lower spatial resolution than the TM and ETM+ sensors (Ihlen and Zanter, 2019).

Landsat 8 provides about 650 scenes per day, processed to a Level 1 standard product, providing high-quality and freely available data products. The Level 1 products are radiometrically and geometrically corrected and obtained by the data of both the sensors, the Ground Control Points (GCPs) and DEMs. The geometric correction prevents the distortions caused by the sensors (e.g., view angle effects), the satellite (e.g., attitude deviations) and the Earth (e.g., rotation, curvature, relief); while the radiometric correction avoids detector differences, dark current bias and general artefacts. Each Level 1 product consists of thirteen files: 11 band images (i.e., the OLI bands are 1-9 while the TIRS bands are 10 and 11), a product-specific metadata file and a quality assessment image. This last leads to evaluating specific land cover types, such as the clouds, and the fill data. All the thirteen files are in 16-bit GeoTIFF (Georeferenced Tagged Image File Format). The geographic information embedded within the Level 1 product lead to georeferencing the image in a geographic information system (Ihlen and Zanter, 2019).

The standard file-naming convention for the Level 1 products leads to giving some relevant preliminary information to the users (**Table 3**).

Table 3 - The standard file-naming convention for Landsat 8 Level 1 product.

LXSS_LLLL_PPPRRR_YYYYMMDD_yyyymmdd_CC_TX	
L	Landsat
X	Sensor type (“C” = OLI+TIRS, “O” = OLI, “T” = TIRS)
SS	Satellite (“08” = Landsat 8)
LLLL	Processing collection level (L1TP/L1Gt/L1Gs)
PPP	Path
RRR	Row
YYYYMMDD	Acquisition year (YYYY), month (MM) and day (DD)
Yyyymmdd	Processing year (yyyy), month (mm) and day (dd)
CC	Collection number (01, 02...)
TX	Collection category (“RT” = real time, “T1” = tier 1, “T2” = tier 2)
Example	LC08_L1TP_167039_20200722_20200722_01_RT

The USGS EarthExplorer is the search interface for downloading the Landsat data product, besides other aerial, mapping, elevation, and satellite data available in the USGS archives.

The dataset used for the multispectral analysis of the LMP includes the image tiles displayed in **Figure 8**. Considering the climatic regime of the LMP, two periods characterised by opposite moisture conditions have been selected including the wettest season (October-December) and the driest one (July-August) of 2017. Consequently, the selected dataset presents different conditions of reflectance because of variation in soil moisture, vegetation cover and percentage of suspended materials along watercourses, but the clearness of the selected imagery allows to properly interpret Earth surface landforms and processes.

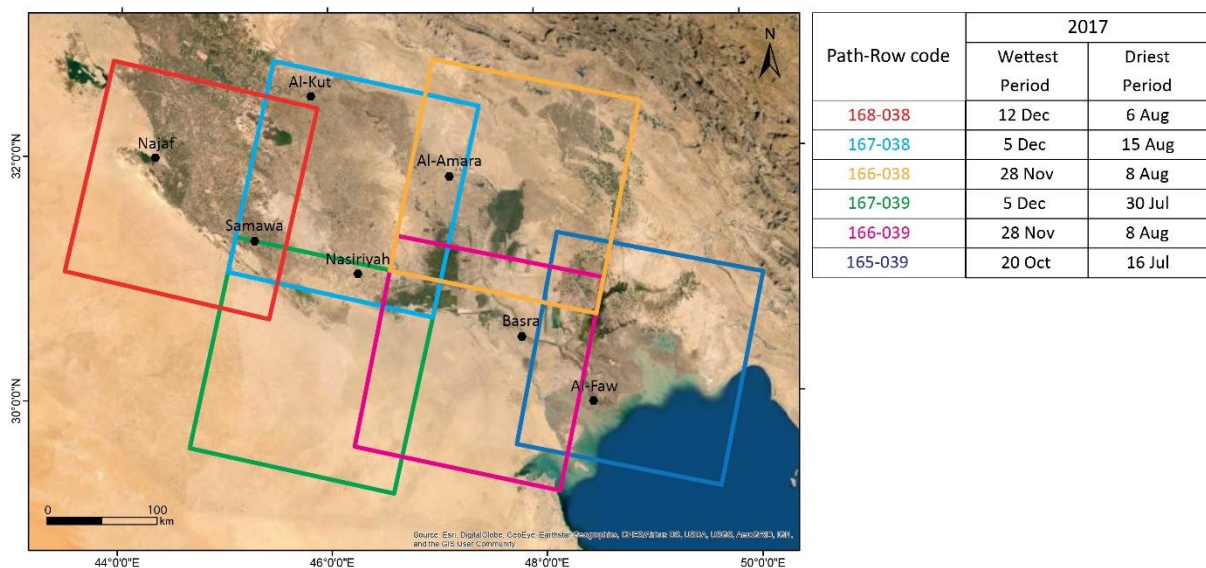


Figure 8 - The tiles of Landsat 8 available for the LMP. The tiles are identified by their Path-Row code in the table, specifying the acquisition date for the wettest and driest period.

4.2 COSMO-SkyMed Product (©ASI - Agenzia Spaziale Italiana)

COSMO-SkyMed© (COnstellation of small Satellites for Mediterranean basin Observation) is the largest Italian investment in Space Systems for the Earth Observation, composed by a constellation of four Low Earth Orbit satellites with a multi-mode high-resolution SAR (Synthetic Aperture Radar) operating at X-band, which is able to operate in all visibility conditions at high resolution and in real-time. The four satellites have been separately launched on 8th June and 9th December 2007, while the

last two on 25th October 2009 and 6th November 2010 (Fiorentino et al., 2019, <https://directory.eoportal.org/web/eoportal/satellite-missions/c-missions/cosmo-skymed>). The two couple of the constellation flies in proximity in order to acquire with a temporal gap of 24 hours, attenuating the coherence problem (Capaldo, 2013).

COSMO-SkyMed© provides essential global information useful for various applications, like risk management, cartography, agriculture, forest, hydrology, geology, and archaeology. Considering the wide application of the COSMO-SkyMed© data, the SAR has been designed for acquiring at different spatial resolution:

- SPOTLIGHT: high resolution and small image area;
- STRIPMAP (Himage and Ping-pong): medium resolution and medium image area;
- SCANSAR (Wide and Huge Region): lower resolution and wide image area.

The Spotlight and Stripmap acquisition mode are ideal for the classification and identification purposes, while the Scansar acquisition mode is perfect for monitoring and detecting wide areas, for example during a flood or an earthquake (Fiorentino et al., 2019). Further characteristics for each acquisition mode are summarized in **Table 4**.

Table 4 - The four acquisition mode's specifications available for the COSMO-SkyMed© SAR. T = transmit, R = receive, H = horizontal, V = vertical.

Spotlight		
Resolution (m)	1	
Scene size (km)	10 x 10	
Polarization (T/R)	Single, HH or VV	
Incidence angles (deg)	20.0 – 59.5	
	Stripmap Himage	Stripmap Ping-Pong
Multi-look resolution (m)	5	20
Scene size (km)	40 x 40	30 x 30
Polarization (T/R)	Single, HH or HV or VH or VV	Alternating, HH/VV or HH/HV or VV/HH
Incidence angles (deg)	18.0 – 59.8	18.86 – 59.49
	Scansar Wide	Scansar Huge
Multi-look resolution (m)	30	100
Scene size (km)	100 x 100	200 x 200
Polarization (T/R)	Single, HH or HV or VH or VV	
Incidence angles (deg)	18.4 – 59.9	

The COSMO-SkyMed© products are distinguished into i) Standard Products, ii) Higher Level Products and iii) Auxiliary Products. The Standard Products are classified into five levels of processing:

- Level 0 (RAW),
- Level 1A Single-look Complex Slant (SCS) products,
- Level 1B Detected Ground Multi-look (DGM) products,
- Level 1C Geocoded Ellipsoid Corrected (GEC) products,
- Level 1D Level Geocoded Terrain Corrected (GTC) product.

The Higher-Level Products are:

- Quick-Look Products
- Speckle Filtered Products
- Co-registered Products

- Interferometric Products
- Digital Elevation Model (DEM) Products
- Mosaicked Products

As for the Landsat 8 products, the COSMO-SkyMed© ones are named according to a specific convention for identifying the SAR Standard Products and most of the Higher Level Products files (**Table 5**).

Table 5 - The standard file-naming convention for COSMO-SkyMed® products.

CSKS<i>_<YYY_Z>_<MM>_<SS>_<PP>_<s><o>_<D><G>_<YYYYMMDDhhmmss>_<YYYYMMDDhhmmss>.h5		
Sub-string code	Meaning	Allowed values
<i>	Identifier of the satellite within the SAR constellation that acquired the scene	1, 2, 3, 4
<YYY_Z>	Product type	Standard Products: RAW_B, SCS_B, SCS_U, DGM_B, GEC_B, GTC_B
<MM>	Instrument Mode used during the acquisition	HI (Himage), PP (PingPong), WR (WideRegion), HR (HugeRegion), S2 (Spotlight 2)
<SS>	Identifier of the swath (or subswath combination in the case of ScanSAR mode) used for the data acquisition	[0A-0B-01-...-24] for Himage [0A-0B-01-...-23] for PingPong [00-...-07] for WideRegion [00-...-05] for HugeRegion [0A-...-0D-01-...-33] for Enhanced Spotlight
<PP>	Polarizations used during the acquisition	HH = Horizontal Tx/Horizontal Rx for Himage, ScanSAR and Spotlight modes VV = Vertical Tx/ Vertical Rx for Himage, ScanSAR and Spotlight modes HV = Horizontal Tx/ Vertical Rx for Himage, ScanSAR VH = Vertical Tx/ Horizontal Rx for Himage, ScanSAR CO = Co-polar acquisition (HH/VV) for PingPong mode CH = Cross polar acquisition (HH/HV) with Horizontal Tx polarization for PingPong mode CV = Cross polar acquisition (VV/VH) with Vertical Tx polarization for PingPong mode
<s>	Identifier of the Look Side	L = Left; R = Right
<o>	Identifier of the Orbit Direction	A = Ascending; D = Descending
<D>	Delivery Mode	F = Fast, S = Standard
<G>	State of the Selective Availability during the acquisition, affecting Orbital Data derived by GPS Instrument	N = On; F = Off
<YYYYMMDDhhmmss>	Sensing Start Time rounded to the closest integer second	YYYY = year MM = month DD = day hh = hour mm = minute ss = seconds
<YYYYMMDDhhmmss>	Sensing Stop Time rounded to the closest integer second	As for sensing start time

Level 1A Single-look Complex Slant (SLC) products are adopted for the extraction of the high-resolution DTM of Tell Zurghul archaeological site, selecting the Spotlight acquisition mode.

In order to successfully generate a DEM, some crucial features must be considered for selecting suitable images. The first one is the *shortest temporal baseline* (i.e., the time between the first and the second image acquisition) for reducing the risk of temporal decorrelation of the phase. Any surface change between both the acquisitions generates an out-of-phase signal not exploitable, for example over vegetated and water areas, under variable moisture conditions or moving objects. Despite small areas with decorrelation are tolerated, most of the image should have visible fringes in the interferogram and high coherence. Secondly, it must be taken into account the *perpendicular baseline* (i.e. the distance between the satellite at the time of image acquisition and the target). The perpendicular baseline should be between 150 and 300 meters to display the objects of different heights relative to each other. Smaller is the perpendicular baseline, higher is the coherence and lower is the evidence of the topography. Finally, the *atmospheric conditions*, especially the water vapour, could decrease the quality of the image and delay the phase; thus, the images acquired during rainfall seasons are not suitable for the DEM extraction (Braun, 2020).

Taking into account these main aspects for downloading the suitable data, a specific form has been filled for a formal request to ASI (Agenzia Spaziale Italiana), which has sent the files showed in **Figure 9**.

Bearing in mind the aforementioned features, ASI has automatically selected two couples of images, in descending and ascending orbits, respectively. Ascending-descending combination is potentially useful for filling the gaps in the DEM, due to the geometric deformations or SAR images (Carrasco et al., 2014), especially when the target area is rather flat. Thus, the temporal baseline is as much as possible low between the ascending and the ascending couples (i.e. eight days for the ascending couple and four days for the descending's ones), as well as the perpendicular baseline. Concerning the atmospheric conditions, besides March is not the ideal period because of the average rainfall of about 20 mm (the highest rainfall period is January with about 27 mm), the water vapour noise is not so relevant for the selected imagery.

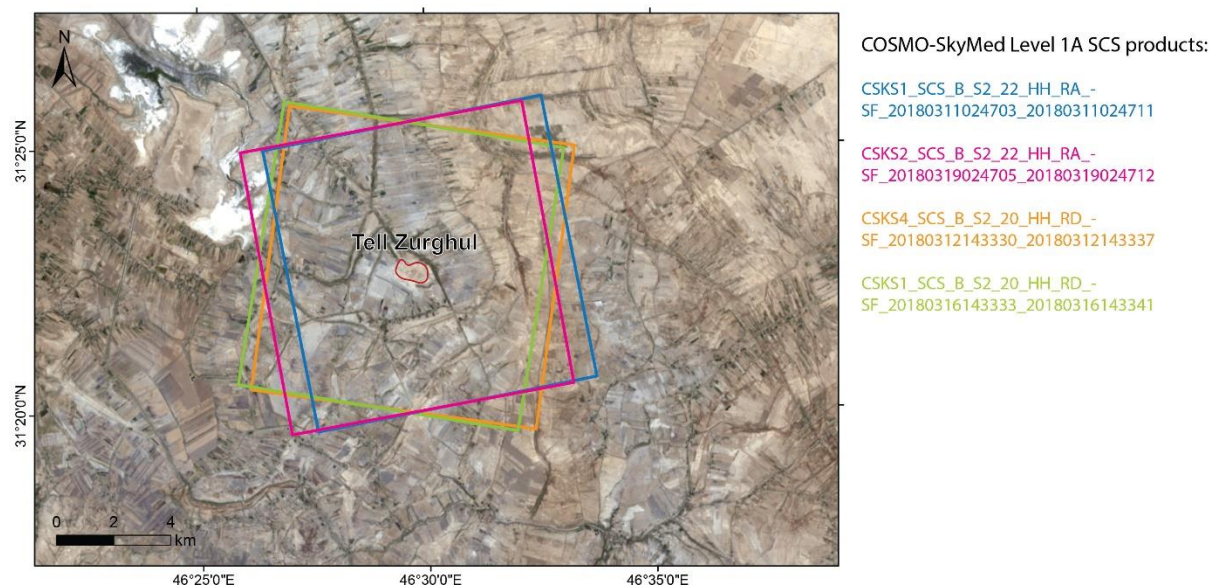


Figure 9 - The tiles of COSMO-SkyMed© furnished by ASI. The tiles are identified by their file-naming convention. The blue and pink tiles are the ascending couple, while the yellow and green tiles are the descending ones.

4.3 ALOS DEM

Besides the topographic data extracted for the archaeological site of Tell Zurghul, the entire LMP has been investigated through two freely available 1 arcsec DEMs. Their 30 m cell⁻¹ ground resolution is perfectly suitable for the main aims of the geomorphological investigation performed within the Lower Mesopotamian floodplain.

The Advanced Land Observing Satellite (ALOS) derives from the Japanese Earth observing satellite program, mainly consisting of marine-atmospheric observation and land observation. ALOS follows two previous missions, the Japanese Earth Resources Satellite-1 (JERS-1) and the Advanced Earth Observing Satellite (ADEOS), respectively ended on October 11, 1998 and on June 30, 1997 because of structural damage (https://www.eorc.jaxa.jp/ALOS/en/about/about_index.htm, <https://earth.esa.int/web/eoportal/satellite-missions/j/jers-1>, <https://earth.esa.int/web/eoportal/satellite-missions/a/adeos>).

ALOS has been launched on January 24, 2006 and ended its mission on May 12, 2011, operating for five years beyond its design life of three years. ALOS high-resolution data have been used for cartography, regional observation, environmental and hazard monitoring within 48 hours, and resource surveying, thanks to its three remote-sensing instruments. The first one is the Panchromatic Remote-sensing Instrument for Stereo Mapping (PRISM) used for cartographic applications, such as the extraction of high-resolution DEMs. PRISM is equipped with three independent catoptric telescopes (i.e., nadir, forward and backwards-looking), whose 40,000 pixels only 14,000 are electronically selected and sent to the ground station. Thus, a triplet image is made of 42,000 pixels (<https://earth.esa.int/web/eoportal/satellite-missions/a/alos>).

The Advanced Visible and Near Infrared Radiometer type 2 (AVNIR-2) is the second instrument furnished to ALOS and consists of a visible and near-infrared radiometer for detecting land and coastal areas through high-resolution (10 m) multispectral data. Its main application is the environmental monitoring, such as the land cover and the land-use maps, essentially guaranteed by the 7000 pixels per CCD detectors (Charged Coupled Device) (<https://earth.esa.int/web/eoportal/satellite-missions/a/alos>, <https://www.eorc.jaxa.jp/ALOS/en/about/avnir2.htm>).

The last remote-sensing instrument is the Phased Array type L-band Synthetic Aperture Radar (PALSAR), a side-looking phased array using L-band frequency to obtain day-and-night and all-weather land data. PALSAR has three operational modes (i.e., Fine resolution Beam, ScanSAR and 14 MHz polarimetric), but the ScanSAR mode is the most improved, being able to acquire SAR images width 250-300 km thanks to the size of the SAR antenna (i.e., 8.9 m in length and 3.1 m in width). Moreover, an array of 80 T/R modules (transmitting/receiving) is present (<https://earth.esa.int/web/eoportal/satellite-missions/a/alos>, <https://www.eorc.jaxa.jp/ALOS/en/about/avnir2.htm>). Further information about ALOS instruments are summarized in **Table 6**.

Table 6 - The main features of ALOS remote-sensing instruments.

PRISM (Panchromatic Remote-sensing Instrument for Stereo Mapping)				
Number of Bands	1 (Panchromatic)			
Wavelength	0.52 – 0.77 μm			
Spatial Resolution	2.5 m (at Nadir)			
AVNIR-2 (Advanced Visible and Near Infrared Radiometer type 2)				
Number of Bands	4			
Wavelength	Band 1: 0.42 – 0.50 μm Band 2: 0.52 – 0.60 μm Band 3: 0.61 – 0.69 μm Band 4: 0.76 – 0.89 μm			
Spatial Resolution	10 m (at Nadir)			
PALSAR (Phased Array type L-band Synthetic Aperture Radar)				
Acquisition mode	Fine resolution bean		ScanSAR	14 MHz polarimetric
Centre frequency	1270 MHz(L-band)			
Chirp Bandwidth	28 MHz	14 MHz	14 MHz, 28 MHz	14 MHz
Polarization	HH or VV	HH + HV or VV + VH	HH or VV	HH+HV+VH+VV
Range Resolution	7 – 44 m	14 – 88 m	100 m (multi-look)	24 – 89 m
Observation Swath	40 – 70 km	40 – 70 km	250 – 350 km	20 – 65 km

The first dataset released by PRISM is a high-resolution topographic map at about 5-m (0.15 arcsec) resolution and called ALOS World 3D (AW3D). AW3D is more correctly defined as a Digital Surface Model (DSM) because it derives from stacking of fine resolution (0.075 arcsec) ortho-rectified images where structures and vegetation are not removed. Indeed, photogrammetric techniques are frequently adopted to create topographic data from optical images, taken at different angles, and different satellites such as ALOS have collected and still collect visible and infrared imagery, suitable for generating topographic data (Mudd, 2020).

The second dataset released by PRISM is the AW3D30, derived from the higher resolution 5-m AW3D dataset and with a ground resolution of 1 arcsec (about 30 m cell⁻¹). The AW3D30 has been first released in 2016 and freely available at <https://www.eorc.jaxa.jp/ALOS/en/aw3d30/index.htm>. Anyway, in 2018 a new version has been released where several improvements occurred, such as the enhanced data calibration and the assessment of errors through the ICESat data (Mudd, 2020). Indeed, the AW3D dataset has been firstly validated through the ICESat data points, averaged over its 64-m footprint, resulting in that the 90% linear errors are on the order of 5 m. Moreover, Lidar and various GPS dataset’s control points have been adopted specifically for some sites, where 90% of the linear errors are mainly connected with topographic slope. Specifically, the 90% of the linear errors are less than 4 m for slopes below 20 degrees, while for steeper slopes the linear errors rise up to 9.20 m. Thus, since the AW3D30 dataset has been extracted from the AW3D dataset, the linear errors of the 30-m dataset could be higher, besides this assessment for the latest version of 2018, with higher accuracy, is not available (Mudd, 2020). Anyway, considering the rather flat area of the LMP, the linear errors should not be greater than the 4-5 m estimated for the AW3D areas with slopes up to 20 degrees.

The entire LMP has been covered with nineteen tiles, derived from the AW3D30 dataset, and mosaicked together in ESRI® ArcMap 10.6 (**Figure 10**).

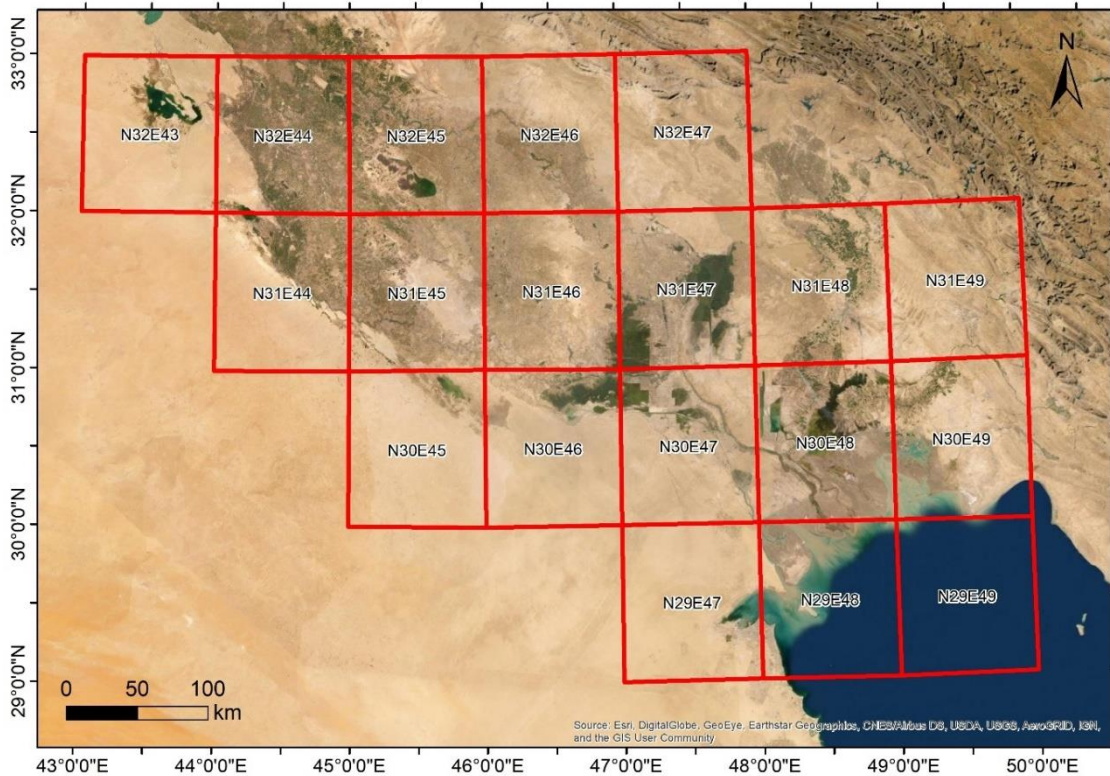


Figure 10 - The downloaded AW3D30 tiles for covering the LMP. Each tile is identified by its latitude-longitudinal name.

4.4 ASTER DEM

An additional DEM has been considered for the study of the LMP in order to enhance the reliability of the topographic elaborations through the comparison and mutual confirmation of different sources (Iacobucci et al., 2020).

ASTER (Advanced Spaceborne Thermal Emission and Reflection Radiometer) is the Japanese instruments aboard NASA's Terra spacecraft (launched in February 1999 and still active), a joint Earth-observing mission between USA, Japan, and Canada. Terra carries aboard other four instruments for obtaining information about the physical properties of clouds, for evaluating the air-land and air-sea exchanges of energy, carbon, and water, for measuring trace gases, and for volcanological applications. These instruments are the American CERES (Clouds and Earth's Radiant Energy System), MISR (Multi-angle Imaging Spectroradiometer) and MODIS (Moderate Resolution Imaging Spectroradiometer) and the Canadian MOPITT (Measurements of Pollution in the Troposphere) (<https://directory.eoportal.org/web/eoportal/satellite-missions/t/terra#sensors>, <https://earthdata.nasa.gov/learn/articles/new-aster-gdem>).

ASTER provides high-resolution (15 to 90 square meters per pixels) and multispectral imagery of the Earth's surface and clouds through three instruments subsystems, which operate in a different spectral region. Specifically, the subsystems are three telescopes in VNIR (Visible Near Infrared), SWIR (Shortwave Infrared) and TIR (Thermal Infrared), covering fourteen different wavelengths of the electromagnetic spectrum (Table 7) (<https://directory.eoportal.org/web/eoportal/satellite-missions/t/terra#sensors>, <https://terra.nasa.gov/about/terra-instruments/aster>).

Table 7 - The parameters of ASTER's subsystems (VNIR, SWIR and TIR).

Parameter	Band No	VNIR	Band No	SWIR	Band No	TIR	
Spectral bands in μm	1	0.52-0.60	4	1.600-1.700	10	8.125-8.475	
	2	0.63-0.69	5	2.145-2.185	11	8.475-8.825	
	3N	0.76-0.86	6	2.185-2.225	12	8.925-9.275	
	3B	0.76-0.86	7	2.235-2.285	13	10.25-10.95	
	Stereoscopic viewing capability along-track			8	2.295-2.365	14	10.95-11.65
				9	2.360-2.430		
Ground resolution	15 m		30 m		90 m		

Besides the application of ASTER data for creating maps of land surface temperature, emissivity and reflectance, its dataset is adopted to extract the Global Digital Elevation Model (GDEM) from the in-track stereo images of the VNIR camera, processing about 2.3 million scenes. The first version of the GDEM has been released in June 2009 to users worldwide at no charge, while a second version (here named as GDEM2) has been available since October 2011 with considerable improvements derived from new 260,000 scenes, higher spatial resolution and enhanced water masking. This last version has been adopted for the study area, downloaded from <https://search.earthdata.nasa.gov/search>. For the LMP, the selected tiles are eighteen, covering the same area of ALOS, and mosaicked together in ESRI® ArcGIS 10.6 (Figure 11).

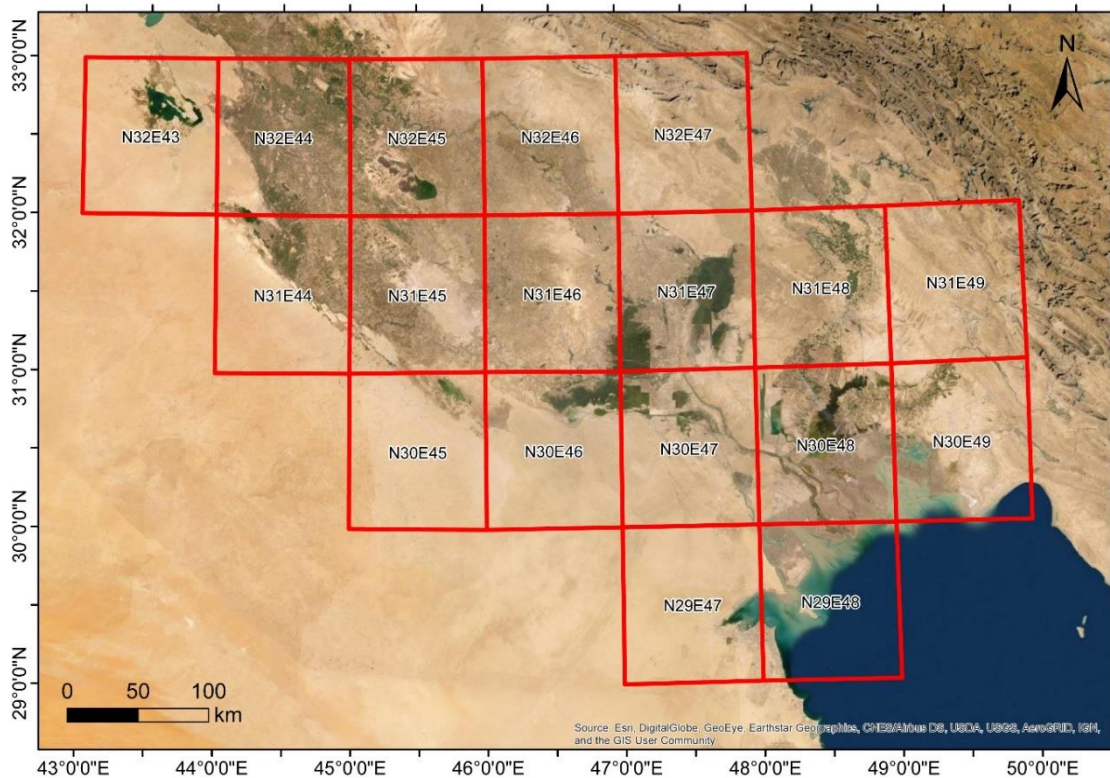


Figure 11 - The selected tiles of GDEM2 for covering the LMP area, identified by their latitude-longitude name.

The GDEM2 is released in GeoTIFF format with a 1 arcsecond (about 30 m cell⁻¹) grid of elevation postings. The vertical and horizontal accuracies of this DEM are 20 m and 30 m, respectively, at 95% confidence (<https://lpdaac.usgs.gov/news/nasa-and-meti-release-aster-global-dem-version-3/>).

5. Methods

This section forms the basis for the paper Iacobucci et., 2020. Specification:

Iacobucci, G.; Troiani, F.; Milli, S.; Mazzanti, P.; Piacentini, D.; Zocchi, M.; Nadali, D. Combining Satellite Multispectral Imagery and Topographic Data for the Detection and Mapping of Fluvial Avulsion Processes in Lowland Areas. *Remote Sensing*. 2020, 12, 2243

The following section will be dedicated to the methodological approach for detecting active and relict fluvial landforms that most of all characterize the waterscape of the LMP. Indeed, this area presents several examples of active channels with a meandering and anastomosing pattern, abandoned channels belonging to a paleo-delta distributary system, levees above the surrounding floodplains and widespread active and relict crevasse splays (Morozova, 2005; Yacoub, 2011; Jotheri et al., 2016; Engel and Brückner, 2018; Sissakian et al., 2020a). One of the main common features of these landforms is the relatively high topographic elevation that encourages the use of the topographic analysis of the micro-relief.

Optical and multispectral satellite imagery, in addition to the digital topography for the analysis of the micro-relief, are the suitable tools for detecting and mapping the target features in lowland and barren area like the LMP, and their increasing diffusion among geologists, geomorphologists and archaeologists is a suitable challenge for integrating different information and knowledge in a multidisciplinary approach.

The LMP preserves several examples of crevasse splays and abandoned channels, perfectly recognizable using specific features which are detectable through a remote sensing approach. Their main characteristic is the height above the surrounding floodplain. For example, paleochannels and recently abandoned channels frequently appear as a sinuous, convex, single ridge (in contrast to the active channels where the two levees are higher and recognizable respect to the channel itself) (Jotheri, 2016). Anyway, abandoned channels and crevasse splays have optical characteristics, like the typical distributary and anastomosing pattern of the crevasse channels or the ridge-and-swale topography inside of a meander bend in the abandoned channels, that both the preliminary inspection and the multispectral analysis can highlight. Due to the width of the study area, the adoption of specific multispectral indexes and the supervised classification is useful for focusing on these target landforms; lastly, the archaeological area of Tell Zurghul has been adopted as sampling area for proving and increasing the mapping of both active and abandoned fluvial landforms, in addition to the detection of the human impact over the waterscape.

The complete methodological approach follows the steps shown in **Figure 12**.

World Imagery provides at least one-meter satellite and aerial imagery in many parts of the world and lower resolution satellite imagery worldwide. For the LMP, the map includes 15 x 15 m TerraColor imagery at small and mid-scale and 2.5 x 2.5m SPOT Imagery (<https://www.arcgis.com/home/item.html?id=10df2279f9684e4a9f6a7f08febac2a9>). This preliminary study allowed an early discerning of active fluvial landforms, especially the meandering and anastomosing channels and the modern canals network, which represents the irrigation systems superimposed to the natural drainage pattern (Kennett and Kennett, 2006; Yacoub, 2011; Engel and Brückner, 2018; Jotheri, 2016; Heyvaert and Walstra, 2016;). Indeed, it is an essential step since the relief of the study area is not sufficiently evident and the automatic extraction of the *blue line* model of the present-day drainage system through the available algorithms in the ESRI® ArcGIS 10.6 does not work.

Some features (i.e., tone, pattern, shape, and situation) are potentially useful for recognizing channels and canals during the preliminary visual inspection (Jotheri, 2016), while the elevation is essentially inspected through the topographic analysis of the micro-relief.

The analysis and interpretation of the micro-relief were favoured by the generation of colour-coded DEMs with a 1–5 m re-classification scheme starting from the sea-level up to the maximum elevation of the study area (with a major interval frequency for the first 30 m a.s.l.). In particular, taking into account the vertical accuracy of the AW3D30 (Santillan et al., 2016; Mudd, 2020) and the GDEM2 (Tachikawa et al., 2011; Mudd, 2020), a re-classification of the elevation data using narrow elevation intervals was helpful for the visual inspection of the floodplain features, even those landforms characterized by low or very low topographic relief such as the fluvial landforms and the human-dug canals. Specifically, 1-m interval re-classified DEMs lead to better visualizing the higher elevation relative to the surrounding floodplain of the archaeological mounds, channels and canals' levees and the crevasse deposits (Jotheri, 2018), as well as to emphasize the visualization of their planform convex geometry (**Figure 13**).

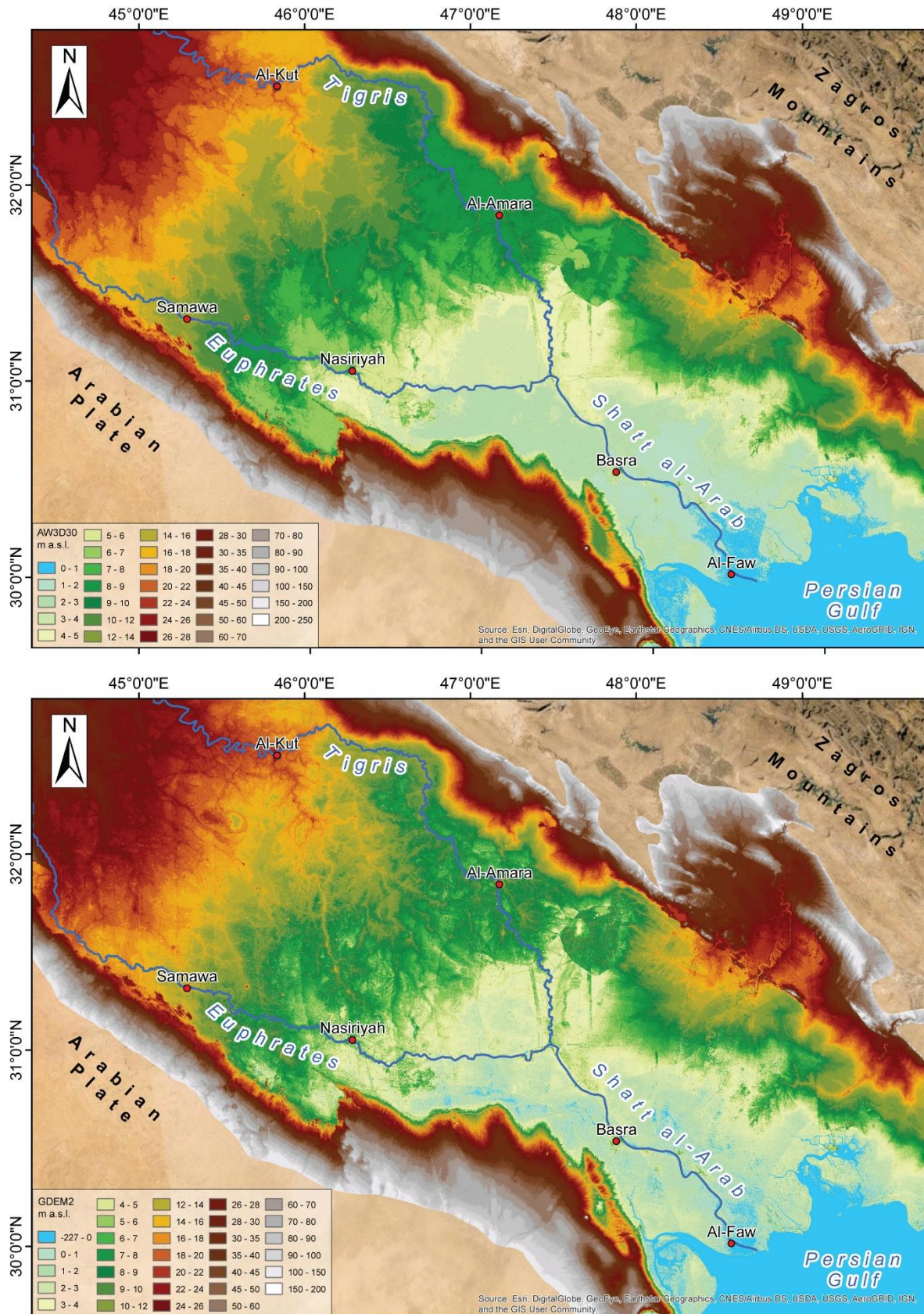


Figure 13 - The mosaicked DEMs AW3D30 and GDEM2, with the colour-coded re-classification. Specifically, both of DEMs are classified 1-m interval between 0 and 10 m a.s.l., 2-m interval between 10 and 30 m a.s.l., 5-m interval between 30-50 m a.s.l., 10-m interval between 50 and 100 m a.s.l. and 50-m interval between 100 and 200 m a.s.l. Both of DEMs are clipped following the 200 and 250 m contour lines, respectively.

The drainage system of the LMP, as well as the ones of other similar lowlands, can be defined as a “suspended drainage system”, where the watercourse (i.e., the bankfull channel and its levees) are higher than the surrounding floodplain. Indeed, the levees of the Mesopotamian watercourses are created by cumulative deposition episodes during each annual flood, so channel levees are higher than the surrounding floodplain, delimiting the channel itself. When the channel is abandoned, the two distinguishable levees are hidden because of their erosion and the siltation of the bankfull channel, resulting in a single levee. Thus, the cross-profiles of the channels, using both elevation dataset, is one of the methods for highlighting the typical double-convex and single-convex profile of active and abandoned channels, respectively (**Figure 14A**) (Hritz and Wilkinson, 2006; Jotheri, 2016).

As regards the crevasse splays, their distinction between active and abandoned has been evaluated through the drawing of four elevation profiles, comparing both the elevation dataset AW3D30 and GDEM2. The first profile is along the dip direction, proximal to the adjacent floodplain, to evaluate the limit of distal crevasse deposits, while further profiles are along the cross direction in the proximal, middle, and distal sectors of the crevasse. In this way, the floodplainward loss of thickness can be appreciated alongside both dip and cross directions (**Figure 14B**).

Due to the use of optical-derived DEMs, the elevation profiles of both channels and crevasse splays are affected by “on-surface noise” because of acquisition limits due to the presence of the vegetation cover, though scarce and scattered in this specific study area. Thus, the moving average filter has been applied for smoothing the elevation data.

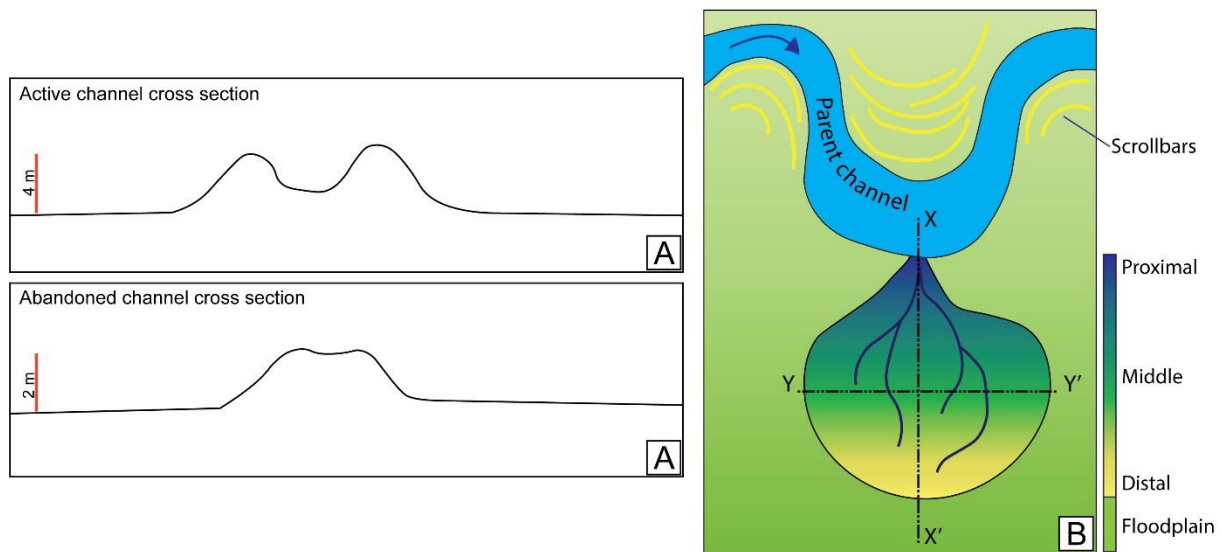


Figure 14 - A) The conceptual cross section sketches of an active and abandoned channel, comparing the double-convexity and the single-convexity, respectively. B) The conceptual sketch of a typical fan-shaped crevasse splay due to a levee break at the outer zone of a river belt. The along-dip crevasse sub-division adopted in this study is reported laterally. Direction and terminology for the altimetric profiles are XX' = along-dip direction, YY' = cross direction.

5.2 Multispectral satellite imagery analysis

The multispectral satellite imagery analysis has been adopted for confirming the crevasse splays recognized during the visual inspection and for detecting their association of landforms such as channels, levees and deposits, whose shape is not always easy to delimit perfectly.

It has long been known that landforms such as alluvial fans of different ages can be distinguished using multispectral imagery (Kahle et al., 1984; Gillespie, 1992; D’Arcy et al., 2018, Iacobucci et al., 2020). Indeed, different reflectance properties in deposits with different ages have been attributed to

changes in chemistry, mineralogical composition, and micro-relief as a result of weathering (Kahle et al., 1984; Bull, 1991; D’Arcy et al., 2018, Iacobucci et al., 2020). Therefore, multispectral imagery can be used to get information about the types of sedimentary deposits characterizing the fluvial landforms of the LMP (D’Arcy et al., 2018). Due to the availability of multispectral Landsat 8 satellite imagery for the LMP, a multispectral analysis and supervised classifications have been carried on.

The multispectral analysis has been carried on through the ENVI 5.3 software, on which the six tiles reported in **Figure 8** have been firstly mosaicked, obtaining two mosaics for the wettest and driest periods, respectively.

The Spectral Indices Toolbox available in ENVI 5.3 allows computing several spectral indices combining the spectral reflectance between two or more wavelengths, indicating the relative abundance of the target features (<https://www.harrisgeospatial.com/docs/spectralindices.html>). Among these, the Vegetation Indices and Geology Indices are the most suitable for the association of landforms which characterizes a crevasse splay. The Vegetation Indices are fundamental for monitoring the ecosystem and land surface processes, among which the Normalized Difference of Vegetation Index (NDVI) is the most adopted (Ke et al., 2015). The vegetation interacts with solar radiation dissimilarly from soils and water bodies because the different plant components (e.g., water, pigments, nutrients, and carbon) vary considerably by wavelength and their reflected optical spectrum- ranges from 400 nm to 2500 nm (<https://www.harrisgeospatial.com/docs/backgroundvegetationindices.html>). NDVI is a measure of healthy green vegetation through the highest absorption and reflectance regions of the chlorophyll and can be applied over a wide range of conditions. NDVI ratio is:

$$\frac{(NIR - Red)}{(NIR + Red)}$$

Specifically, for the Landsat 8 imagery:

$$\frac{(Band\ 5 - Band\ 4)}{(Band\ 5 + Band\ 4)}$$

NDVI allows to assess the seasonal vegetation variability, the lateral shifting degree of the distributary and crevasse channels, and to identify the areas where human activities have a lesser impact. Indeed, NDVI values indicate the amount of green vegetation occurring in each raster pixel and help to discern those areas where crops and human activities have obliterated the ancient landforms. Moreover, the development of vegetation drives the kind of overbank flow (i.e., confined vs unconfined) (Dawson, 1988; Corenblit et al., 2020). The presence of vegetation generally increases velocities within the confined channel, while the lateral outflow occurs due to the decreasing vegetation roughness (Hiatt and Passalacqua, 2017), proving useful information for detecting the areas where the avulsion processes prevail. The topography establishes a lateral water surface gradient between the channel and the islands even with low vegetation roughness, which drives the lateral flow. Hence, the NDVI computation leads to focusing on areas where inactive crevasse splays are better preserved, and human activities do not occur.

The second spectral index computed is a Geology Index known as Clay Ratio (CR), which highlights hydrothermally altered rocks containing clay and alunite through the following ratio:

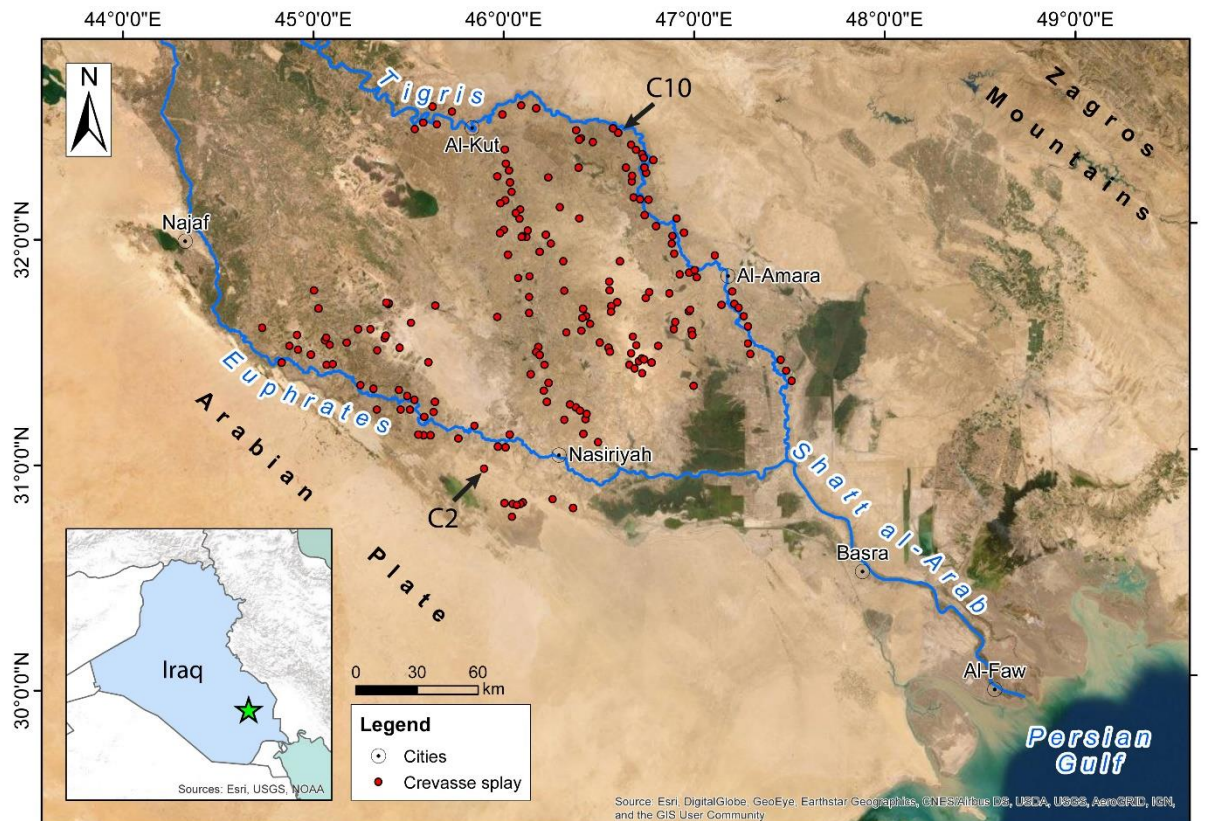
$$\frac{SWIR1}{SWIR2}$$

Specifically, for the Landsat 8 imagery:

$$\text{Band 6} / \text{Band 7}$$

CR is essential for recognizing the activity of the distributaries and crevasse channels and to infer the in-channel flow direction (i.e., floodplainward or riverward). During a flood event, the sand fraction transported as bedload is deposited especially in the proximal part of the splay, whereas the silt and clay fraction is transported in suspension to be deposited in the distal parts, where flow rates are reduced (Burns et al., 2017). The return flow after a flooding event leads to the in-channel deposition of suspended sediment (Van Toorenburg et al., 2018), potentially detectable through the CR.

Finally, specific target features have been submitted in the Supervised Classification (SC). The main aim of the SC is clustering the pixels of a dataset into specific classes defined by the user through training data. In particular, in order to recognize crevasse splays and for focusing exclusively on them, their training data are delineated like Regions Of Interest (ROIs). The target feature of a crevasse splay has been distinguished into three main sub-features in order to better specify the ROIs, where the spectral signature has been extracted: (i) active and abandoned channel; (ii) active levee; (iii) active and abandoned deposit. The ROIs have been extracted on the active crevasse C10 and the abandoned crevasse C2, which sub-features are perfectly recognizable and reported by several authors (**Figure 15**); the calibration ROIs for the SC is composed by 22 records for both the wettest and the driest periods. In the SC, four different methods have been adopted and their performance has been estimated: (1) *Mahalanobis*; (2) *Maximum Likelihood*; (3) *Minimum Distance*; (4) *Spectral Angle Mapper (SAM)*.



FID	OBJECTID	Area (km2)															
1	C1	12,4	28	C28	19,0	55	C55	1,8	82	C82	0,1	109	C109	12,9	136	C136	3,2
2	C2	97,5	29	C29	9,9	56	C56	4,9	83	C83	0,1	110	C110	17,1	137	C137	14,4
3	C3	16,2	30	C30	30,8	57	C57	3,6	84	C84	0,2	111	C111	55,9	138	C138	6,5
4	C4	14,3	31	C31	11,9	58	C58	40,5	85	C85	5,9	112	C112	126,0	139	C139	6,0
5	C5	2,5	32	C32	1,0	59	C59	2,0	86	C86	21,1	113	C113	30,5	140	C140	8,5
6	C6	2,6	33	C33	0,7	60	C60	7,8	87	C87	7,1	114	C114	2,7	141	C141	4,0
7	C7	4,7	34	C34	12,9	61	C61	2,5	88	C88	3,4	115	C115	7,4	142	C142	2,7
8	C8	4,6	35	C35	2,7	62	C62	2,0	89	C89	13,7	116	C116	16,8	143	C143	14,1
9	C9	67,4	36	C36	22,6	63	C63	1,4	90	C90	2,7	117	C117	2,6	144	C144	12,5
10	C10	144,7	37	C37	8,7	64	C64	89,7	91	C91	25,3	118	C118	8,6	145	C145	24,4
11	C11	7,1	38	C38	8,4	65	C65	0,9	92	C92	56,7	119	C119	5,2	146	C146	31,9
12	C12	2,3	39	C39	8,8	66	C66	141,9	93	C93	6,5	120	C120	84,5	147	C147	30,8
13	C13	69,5	40	C40	16,0	67	C67	1,5	94	C94	9,8	121	C121	29,3	148	C148	13,2
14	C14	15,0	41	C41	2,1	68	C68	4,4	95	C95	4,0	122	C122	4,3	149	C149	4,7
15	C15	18,0	42	C42	2,5	69	C69	11,2	96	C96	41,7	123	C123	58,0	150	C150	4,7
16	C16	21,6	43	C43	2,2	70	C70	6,8	97	C97	14,6	124	C124	11,6	151	C151	5,0
17	C17	0,9	44	C44	2,3	71	C71	19,0	98	C98	5,3	125	C125	14,3	152	C152	3,0
18	C18	1,5	45	C45	2,1	72	C72	1,5	99	C99	7,6	126	C126	11,8	153	C153	9,0
19	C19	0,0	46	C46	26,5	73	C73	2,1	100	C100	20,9	127	C127	16,0	154	C154	8,5
20	C20	4,3	47	C47	19,9	74	C74	2,4	101	C101	15,1	128	C128	2,5	155	C155	4,4
21	C21	5,3	48	C48	58,0	75	C75	1,0	102	C102	18,6	129	C129	1,5	156	C156	30,9
22	C22	4,5	49	C49	1,1	76	C76	0,6	103	C103	34,9	130	C130	2,9	157	C157	4,6
23	C23	4,8	50	C50	5,9	77	C77	7,3	104	C104	46,8	131	C131	10,5	158	C158	8,7
24	C24	8,1	51	C51	1,0	78	C78	1,9	105	C105	1,4	132	C132	2,8	159	C159	5,6
25	C25	20,8	52	C52	11,1	79	C79	0,1	106	C106	6,9	133	C133	6,9	160	C160	9,8
26	C26	65,8	53	C53	10,7	80	C80	0,1	107	C107	22,8	134	C134	1,4	161	C161	10,1
27	C27	25,6	54	C54	2,0	81	C81	0,1	108	C108	2,1	135	C135	10,1	162	C162	5,5

Figure 15 - Satellite nadir view of the LMP from TerraColor satellite imagery with the distribution of the active and abandoned crevasse splays recognized in the investigated area during the visual inspection. The active crevasse C10 along the Tigris and the abandoned crevasse C2 along the Euphrates paleobranh are indicated by black arrows, while the entire dataset of the crevasse splays is reported below, highlighting the sample crevasses described in Chapter 6.

Mahalanobis is a direction-sensitive classification method that uses statistics for each class, similarly to Maximum Likelihood. The main difference is the class covariance considered equal, making faster this classification method. The pixels are classified to the closest training data.

Maximum Likelihood assumes the statistics for each class in each band are normally distributed, calculating the probability that a pixel *x* belongs to a specific class. Thus, the pixel *x* will be assigned to the class with the highest probability (i.e., the maximum likelihood).

Minimum Distance uses the mean ROI for each class calculating the Euclidean distance from each unknown pixel to the mean ROI for each class. So, the pixels are classified to the nearest class.

SAM is a physically-based spectral classification that determines the spectral similarity between two spectra through the computation of the angle between the spectra, treating them as ROIs in a space with dimensionality equal to the number of bands. Thus, smaller is the angles, closer is the match to the reference spectrum (<https://www.harrisgeospatial.com/docs/Classification.html#ClassSupervised>).

Different iterations have been done varying the specific thresholds for each classification method, but only the most accurate results have been described and discussed in this study. Despite the unavailability of a definite method to assess the absolute accuracy of image classification for remote sensing Earth observation applications, the computation of a confusion matrix is a widely accepted method to determine the relative accuracy of classifications, using the previous identified ROIs for ground truth (Liu and Mason, 2009). Each element in the major diagonal of the confusion matrix represents the number of pixels that are correctly classified for a class x , whereas the elements out of the major diagonal are the number of pixels that should be in class x but which are incorrectly classified as class y . Certainly, if all the image pixels are correctly classified, we should then have a diagonal confusion matrix where all non-diagonal elements become zero (<https://www.harrisgeospatial.com/docs/Classification.html#ClassSupervised>; Liu and Mason, 2009). The confusion matrix gives back the Overall Accuracy (OA) and the Kappa coefficient (K). The first one is the percentage of the correct classification and the second one is the statistical measure of classification accuracy and quality. The maximum value of K is 1, representing the perfect agreement between the classification and the reference data, while K becomes 0 for no agreement (Liu and Mason, 2009). In light of the discouraged use of the Kappa metric in the remote sensing community for validating a classification (Pontius and Millones, 2011), the User Accuracy (UA) and the Producer Accuracy (PA) have also been taken into consideration. The first one is the probability that a value predicted to be in a class x really is in that class, (i.e., how often the class x on the map occurs on the ground). The PA is the probability that a value in a given class was classified correctly, signifying how often the real features on the ground are correctly shown on the classified map (<https://www.harrisgeospatial.com/docs/CalculatingConfusionMatrices.htm>, http://gis.humboldt.edu/OLM/Courses/GSP_216_Online/lesson6-2/metrics.html). The UA and PA for any given class usually are not the same. **Figure 16** shows an example where the 75% of the crevasse channels occurred on the ground have been correctly classified (i.e., PA = 75%) whereas some of them are wrongly classified as “levee”. Anyway, the class “crevasse channel” perfectly corresponds to the channels on the ground, except for a “fake-channel” on the right side, thus only the 90% of the classified areas as “active channel” are actually a channel (i.e., UA = 90%) (Banko, 1998).

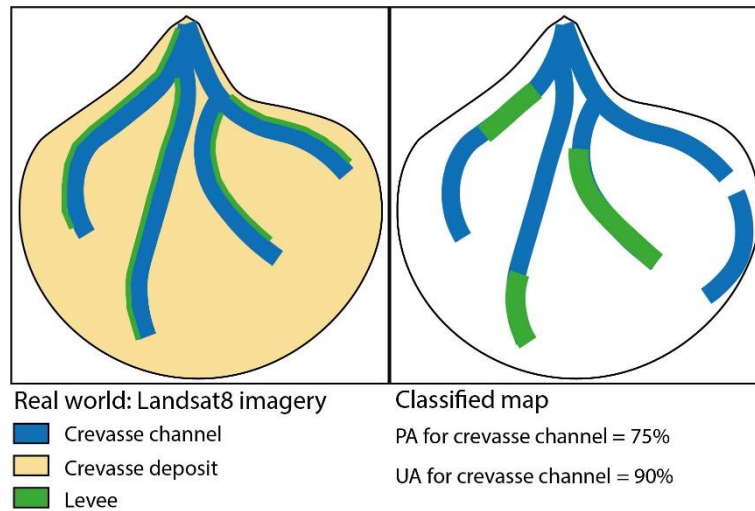


Figure 16 - Example for producer and user accuracy (*sensu Banko 1998*) for a typical landforms association of a crevasse splay.

The assessment of accuracy leads to defining which thresholds must be adopted for the most accurate classifications of crevasse features (**Table 8**).

Table 8 - The most accurate thresholds for each classification method.

Driest period					
	Active channel	Active levee	Active deposit	Abandoned channel	Abandoned deposit
Mahalanobis (Maximum distance error)	3000	2000	2000	2000	2000
Maximum Likelihood (Probability threshold)	0.30	0.70	0.30	0.30	0.30
Minimum distance (Standard deviation from mean)	4.00	1.50	3.00	1.50	3.00
SAM (Maximum spectral angle)	0.10	0.04	0.05	0.008	0.008
Wettest period					
Mahalanobis (Maximum distance error)	3000	1500	1500	1000	1000
Maximum Likelihood (Probability threshold)	0.20	0.60	0.40	0.60	0.30
Minimum Distance (Standard deviation from mean)	3.00	2.00	2.00	1.50	1.30
SAM (Maximum spectral angle)	0.10	0.03	0.03	0.01	0.015

5.3 DEM generation from COSMO-SkyMed© SPOT imagery

The highest-resolution image mode available in COSMO-SkyMed© is the Spotlight, which can achieve resolution of meter or sub-meter through the steering backwards of the antenna when the satellite passes over the area of observation (Lombardi et al., 2016).

The Interferometric synthetic aperture radar (InSAR) exploits the phase difference between two SAR acquisitions taken when the sensor is on two different positions, thus extracting information about the Earth's surface. Indeed, the SAR signal consists of amplitude and phase data; the first one is the

strength of the radar response while the phase is the fraction of one complete sine wave cycle (i.e., a single SAR wavelength), which determines the distance between the satellite and the target feature (Braun, 2020).

In order to extract the DEM of Tell Zurghul area, SARscape version 5.2.0 has been used as an extension of ENVI 5.3. The preliminary step is the conversion of the COSMO-SkyMed© data into SARscape's Data Format through the "Import Data" tool. For the interferometric processing, the selected datasets is a Single Look Complex (SLC) data products, the binary data containing the data matrix, to which other two ASCII files are associated (.sml file contains essential information for the data processing, .hdr file is an ENVI header file for displaying the data). In addition to the SPOT imagery, an accurate reference DEM has been adopted for improving the following steps of geocoding, coregistration and interferometric phase flattening. For the study area, the SRTM is downloaded in SARscape using the "Digital Elevation Model Extraction" tool (Braun, 2020; <https://www.l3harrisgeospatial.com/Support/Self-Help-Tools/Help-Articles/Help-Articles-Detail/ArtMID/10220/ArticleID/15704/DEM-Extraction-from-Radarsat-2-Data-in-SARscape>; http://www.sarmap.ch/tutorials/Getting_started.pdf).

SARscape sets up two workflows for generating DEM; for the COSMO-SkyMed© data the InSAR Digital Elevation Model Workflow is adopted, where after the preliminary steps of the data format conversion and the download of the reference DEM, the main steps are the following:

- Coregistration,
- Interferogram Formation,
- Goldenstein Phase Filtering,
- Phase Unwrapping,
- Phase to Height Conversion and Geocoding.

Coregistration is the first step where both SPOT imagery has been jointed in a stack for exploiting the phase difference between the two acquisitions. Using the image statistics, coregistration aligns both acquisitions at sub-pixels accuracy.

Interferogram Formation is the step where the master image is cross multiplied with the complex conjugate of the slave. The amplitude of both images is multiplied whereas the obtained phase is the difference between the two images, generating a flattened interferogram without the constant phase due to the acquisition mode and the topographic phase. Indeed, the interferometric phase of a SAR image should depend only on the difference in the travel paths between the two acquisitions, but the computed interferogram contains several contributions such as the flat-earth phase (ϕ_{flat}), the topographic phase (ϕ_{DEM}), the atmospheric different conditions between the two acquisitions (ϕ_{atm}), other general noise due to changes in the scatterers, different look angle and volume scattering (ϕ_{noise}), and finally the surface deformation between the two acquisitions (ϕ_{disp}):

$$\varphi = \varphi_{DEM} + \varphi_{flat} + \varphi_{disp} + \varphi_{atm} + \varphi_{noise}$$

When the atmospheric and noise contribution is small as possible and the displacement contribution is null (i.e., there is no change in elevation between the two acquisitions), the contribution of the Earth's surface (ϕ_{flat} and ϕ_{DEM}) is considered equal for the two acquisitions and the heights of the topography are equal to:

$$\varphi_{DEM} = \varphi - \varphi_{flat}$$

The Interferogram Formation or Interferogram Flattening is computed through the input reference DEM (i.e., the SRTM for the selected area).

Goldenstein Phase Filtering is one of the three available filtering methods in SARscape. The interferometric phase could be altered by the temporal and geometric decorrelation, volume scattering or general processing errors. The Goldenstein filter uses a Fast Fourier Transformation (FFT) for increasing the quality of the interferogram fringes (**Figure 17**), essential for the next step of the *Phase Unwrapping*. This filtering approach employs the coherence: lower is the coherence, more filtered are the zones.

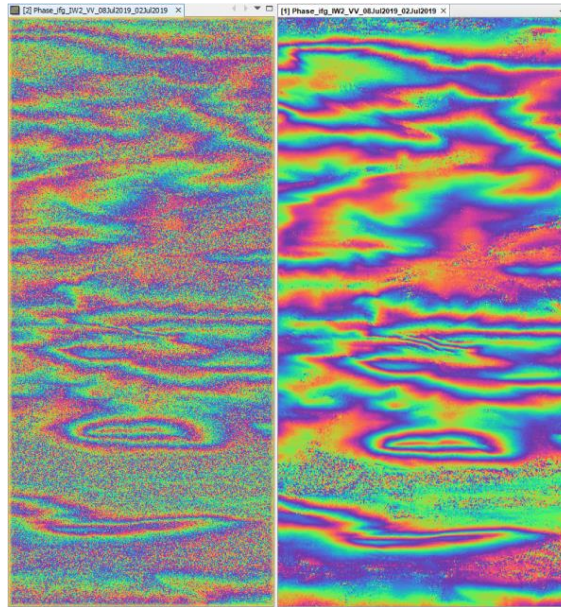


Figure 17 - The interferogram before (left) and after (right) the Goldenstein Phase Filtering (from Braun, 2020).

Phase Unwrapping allows resolving the ambiguity of the interferometric phase when it becomes larger than 2π . Thus, in order to relate the interferometric phase to the topographic height, the phase must be unwrapped by integrating the phase difference between neighbouring pixels. Removing any integer number of the 2π phase cycles, the obtained phase variation between two points represents the actual altitude variation and should be interpreted as relative height (**Figure 18**).

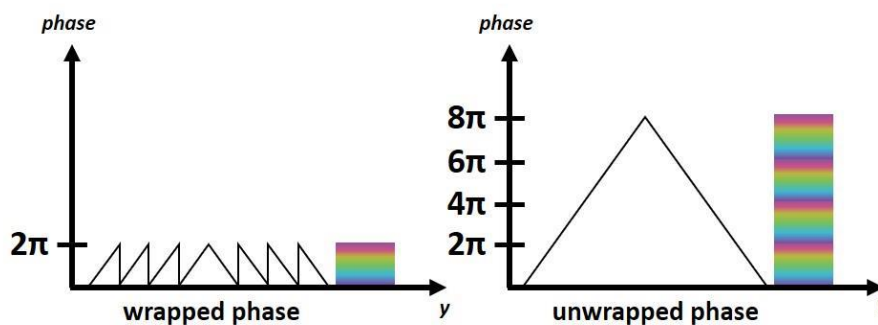


Figure 18 - The difference between the wrapped phase and the unwrapped phase (from Braun, 2020).

The last steps are the *Phase to Height Conversion* and the *Geocoding*, in order to combine the unwrapped phase with the synthetic phase, convert it to height and finally geocode into a map projection. Through the Range-Doppler approach, its equations are applied to the two antennas for getting the height of each pixel and its location in a specific cartographic and geodetic reference system (e.g., for the study the coordinate system is the WGS84 UTM Zone 38 N) (Braun, 2020; https://www.harrisgeospatial.com/docs/pdf/sarscape_5.1_help.pdf).

Both the ascending and descending couples have been processed following this workflow, obtaining the ascending and descending DEMs, respectively. The arithmetic average of both DEMs has been computed through MATLAB R2018b, achieving the DEM (hereafter named CSK-DEM) of the Tell

Zurghul area with a ground resolution of 4x4 m, essentially used for the topographic analysis of the micro-relief.

6. Results

This chapter starts with two essential preliminary results obtained through the small-scale investigation of the entire LMP: the reconstruction of the multi-channel fluvial system and the reconstruction of the early Holocene maximum marine ingressions (i.e., 6000 yrs BP). Indeed, the mapping of the abandoned multi-channel system of the LMP, essentially by the visual inspection of the TerraColor imagery, is the first essential step from which the following ones started (i.e., the medium-scale investigation of the avulsion processes and the large-scale investigation of Tell Zurghul archaeological site). The visual traces of abandoned channelized flow (**Figure 19A**) are essentially recognized by three characteristics such as tone, pattern, and specific association-situation. The tone of the abandoned channels is mainly brownish-greyish, while their levees are vegetated and present a green tone only when a proximal man-made canal occurs; indeed, it is not rare that the modern man-made canals follow the same direction of the abandoned channels, making difficult their distinction. The abandoned channel pattern is frequently sinuous and meandering, but in the areas where the human impact on the landscape is null, the anastomosing pattern is still preserved. Finally, the specific association-situation takes into account the occurrence of other fluvial features like scroll bars or crevasse splays. Then, the mapped abandoned multi-channel system is compared to the topographic data of the AW3D30 (**Figure 19B**), where the above floodplain configuration is still preserved for several abandoned channels. The highest detail is in the floodplain between the Shatt al-Gharraf and Tigris (i.e., between Shatrah and Al-Amara cities), where the large-scale investigation of Tell Zurghul area has been concentrated. The exclusively visual recognition of the abandoned channels is strongly poor where the human activities prevail, like along the areas proximal to the modern rivers, leading to recognize only short reaches.

As concerning the reconstruction of the maximum marine ingressions and its shoreline at 6000 yrs BP, it is obtained through the raster reclassification of the AW3D30 elevation data. The *Reclassify* tool available in ArcGIS 10.6 leads to changing the raster values (i.e., the elevation data) into a new one, specifying only two classes: values below 5 m and values above 5 m. Through the reclassified AW3D30 a plausible reconstruction of the shoreline during the maximum ingressions is feasible, considering the geological and sedimentological evidence which prove the marine ingressions reached the cities of Nasiriyah and Al-Amara, despite Lambeck (1996) proposed a sea-level rise of about 2-3 m in the area of Al-Faw. Indeed, it is worth noting that the value of the sea level rise (i.e., 5 m) is exclusively nominal and the significant result is the reconstructed morphology of the shoreline shown in **Figure 20**. The reconstruction of maximum marine ingressions has been useful essentially for the large-scale investigation of Tell Zurghul area, where the presence of water was so relevant so much so developing a waterscape.

Results obtained during the medium- and large-scale investigation of the LMP are summarized in the following sections. The first section reports the results obtained for the active and abandoned avulsion processes, that constitutes the dataset represented in **Figure 15**. In order to compare the differences between the recognized active and abandoned crevasse splays, four of them have been selected based on their size higher than 50 km²; they are named C10 and C13 (active), C2 and C9 (abandoned). The first section distinguishes the results obtained from each method into a specific subsection.

The second part is dedicated to the detailed mapping of the archaeological site of Tell Zurghul, where the computation of multispectral indices NDVI and CR, in addition to the topographic analysis

of the micro-relief, have been carried on through the Landsat 8 imagery (167-038 coded) and the extracted CSK-DEM.

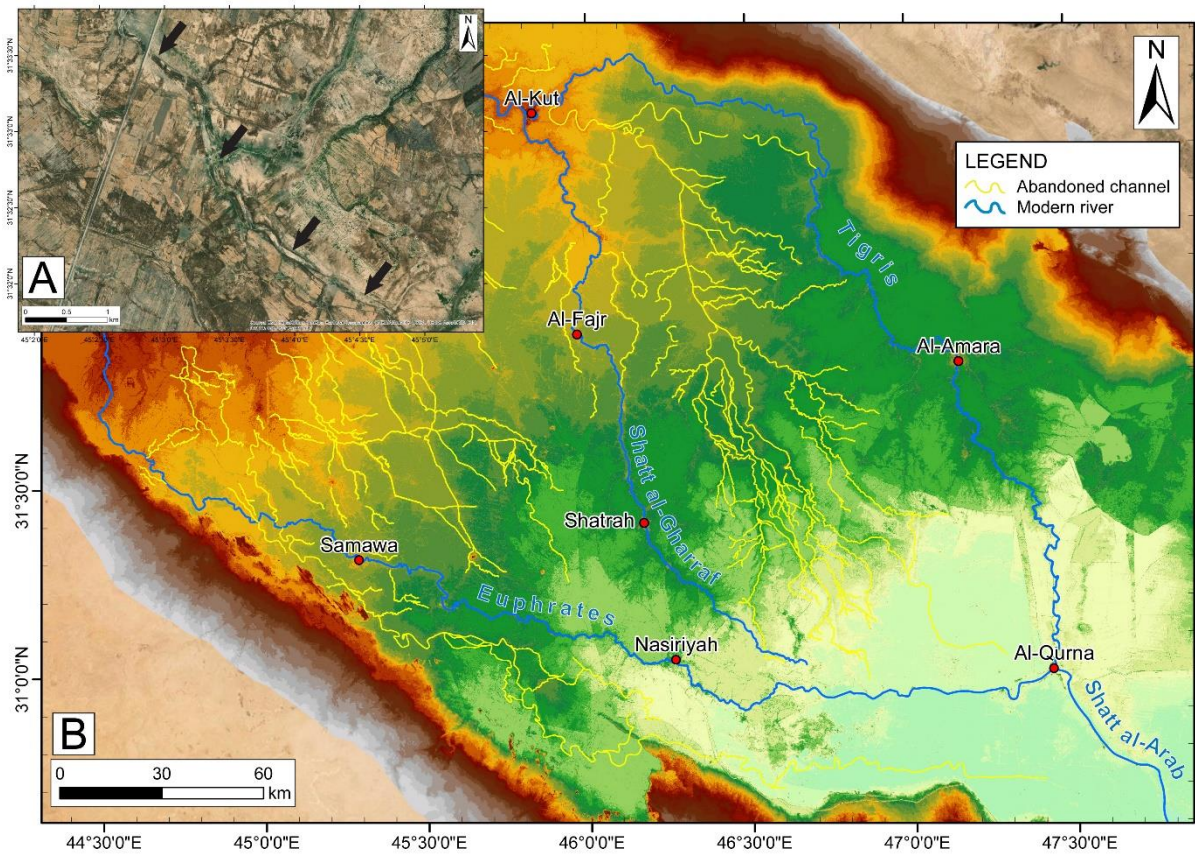


Figure 19 - A) TerraColor example of abandoned channel (pointed out by black arrows). **B)** The reconstruction of the abandoned multi-channel fluvial system which mainly characterized the early Holocene landscape of the LMP.

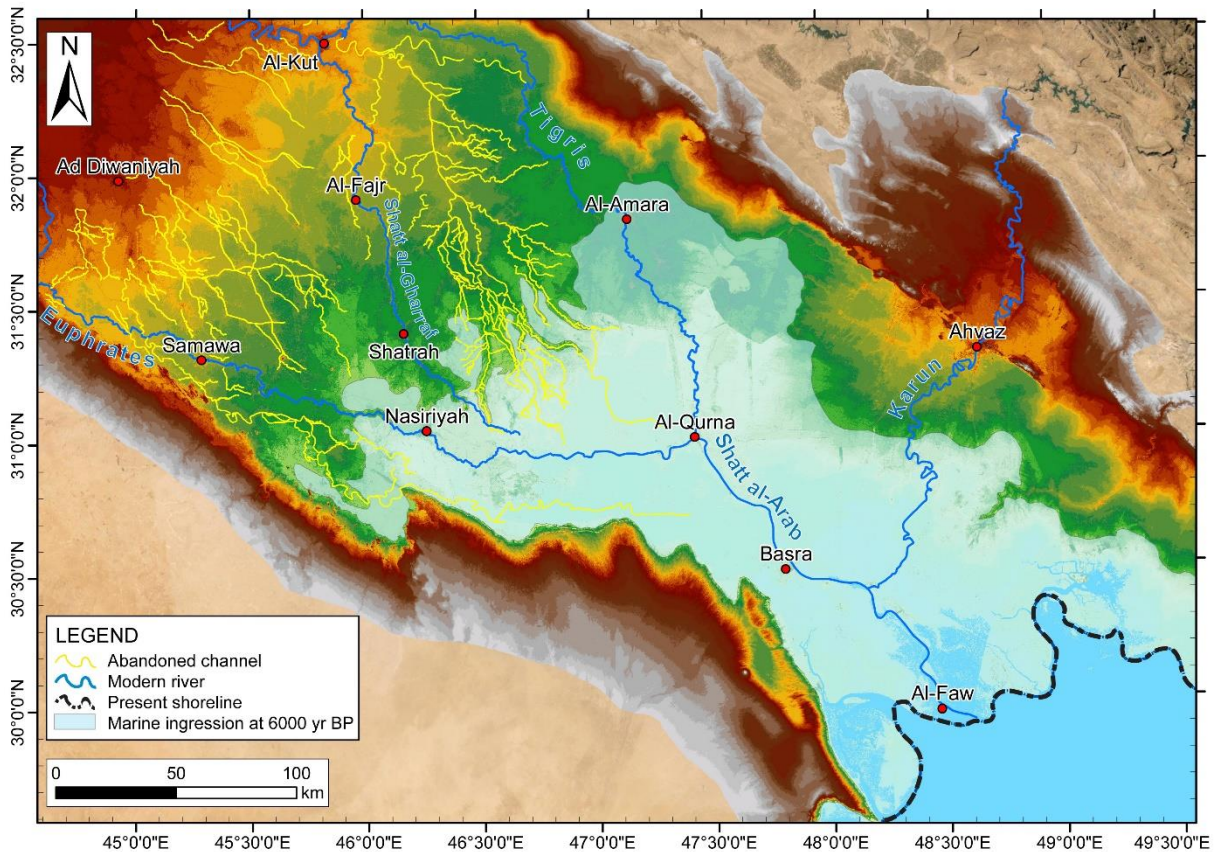


Figure 20 - The reconstructed morphology of the Persian Gulf shoreline during the maximum marine ingress at 6000 yrs BP.

6.1 The avulsion processes

This section forms the basis for the paper Iacobucci et., 2020. Specification:

Iacobucci, G.; Troiani, F.; Milli, S.; Mazzanti, P.; Piacentini, D.; Zocchi, M.; Nadali, D. Combining Satellite Multispectral Imagery and Topographic Data for the Detection and Mapping of Fluvial Avulsion Processes in Lowland Areas. *Remote Sensing*. 2020, 12, 2243

The selected crevasse splays C2, C9, C10 and C13 are sample landforms chosen for highlighting the main differences between active and abandoned avulsion processes. The active crevasse splays C10 and C13 are rather close to each other and are along the Tigris River, downstream Al-Kut city; the abandoned C2 and C9 are located along two abandoned channels, the abandoned Euphrates branch named Khalid Channel and the Dujaila channel (**Figure 21**).

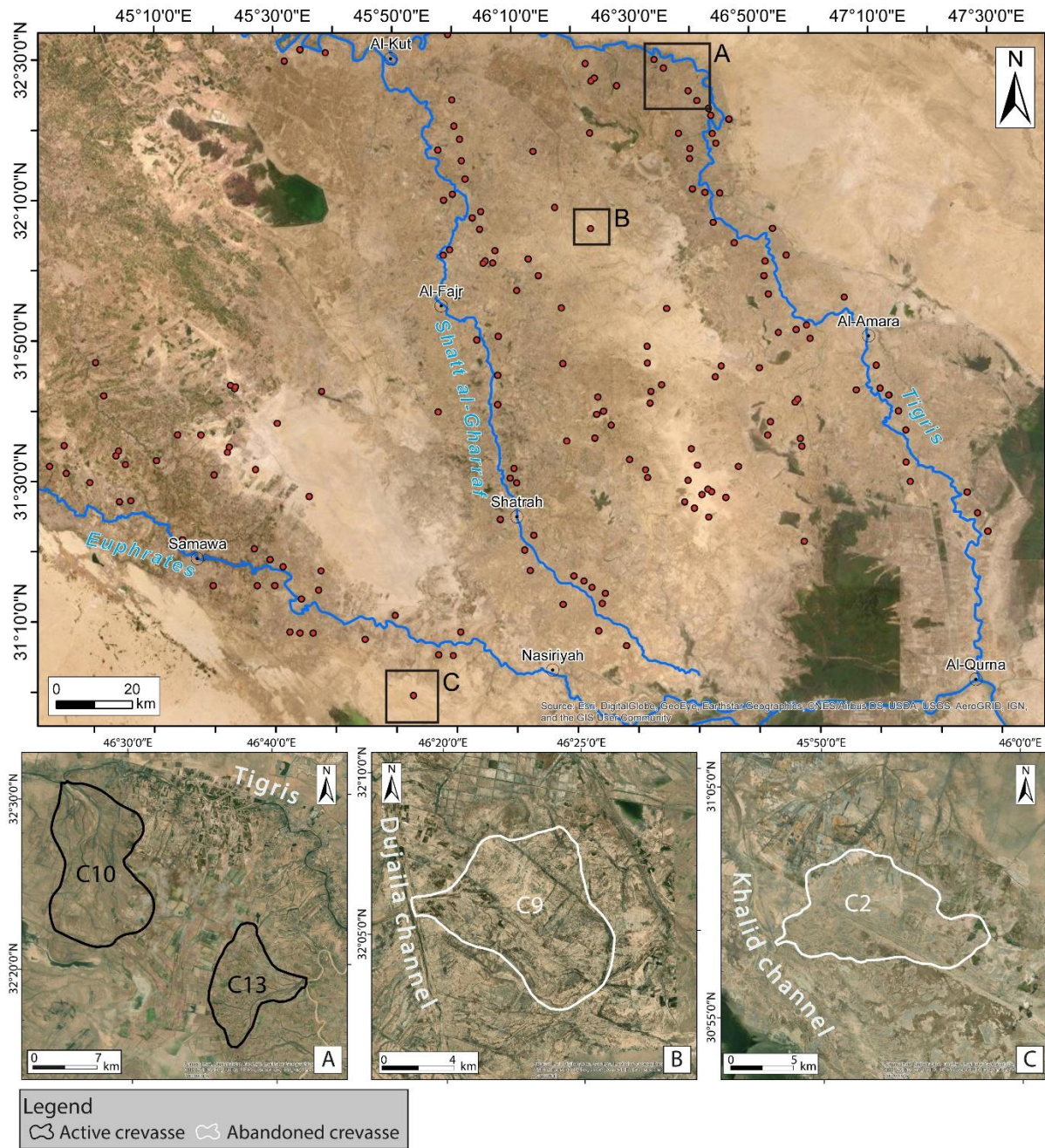


Figure 21 - The location of the selected crevasse splays C10, C13, C9 and C2.

6.1.1 Preliminary inspection and topographic analysis of the micro-relief

The preliminary inspection of the Google® Earth and TerraColor imagery allowed to identify several crevasse splays, either alongside the active fluvial system, especially on the right bank of the Tigris Rivers, or along abandoned channels. In the present research, four examples of crevasse splays have been selected based on their size (> 50 km²) and their state of activity (two examples among the recognized active crevasses and two among the abandoned ones). The preliminary inspection leads to identifying the abandoned Kut-Al-Hayy East airbase in the middle-distal sector of C9. The area of this airbase is about 18 km² and occupies only 25% of the entire C9, with a negligible “noise” in the analysis of the entire landform (Figure 22). The multi-channel system, typical of crevasse splays, is the most

recognizable feature in the optical imagery and its identification favoured the planar delimitation and mapping, especially for the active forms (**Figure 22**). The topographic analysis really improved the preliminary mapping favoured by the relevant differences in the spatial distribution of the deposits between active and abandoned crevasse splays considering the along-dip and cross directions (**Figure 22**). Moreover, the topographic analysis leads to a preliminary estimation of the depth of the deposits through the projection of the floodplain backwards, up to the proximal sector of each along-dip section.

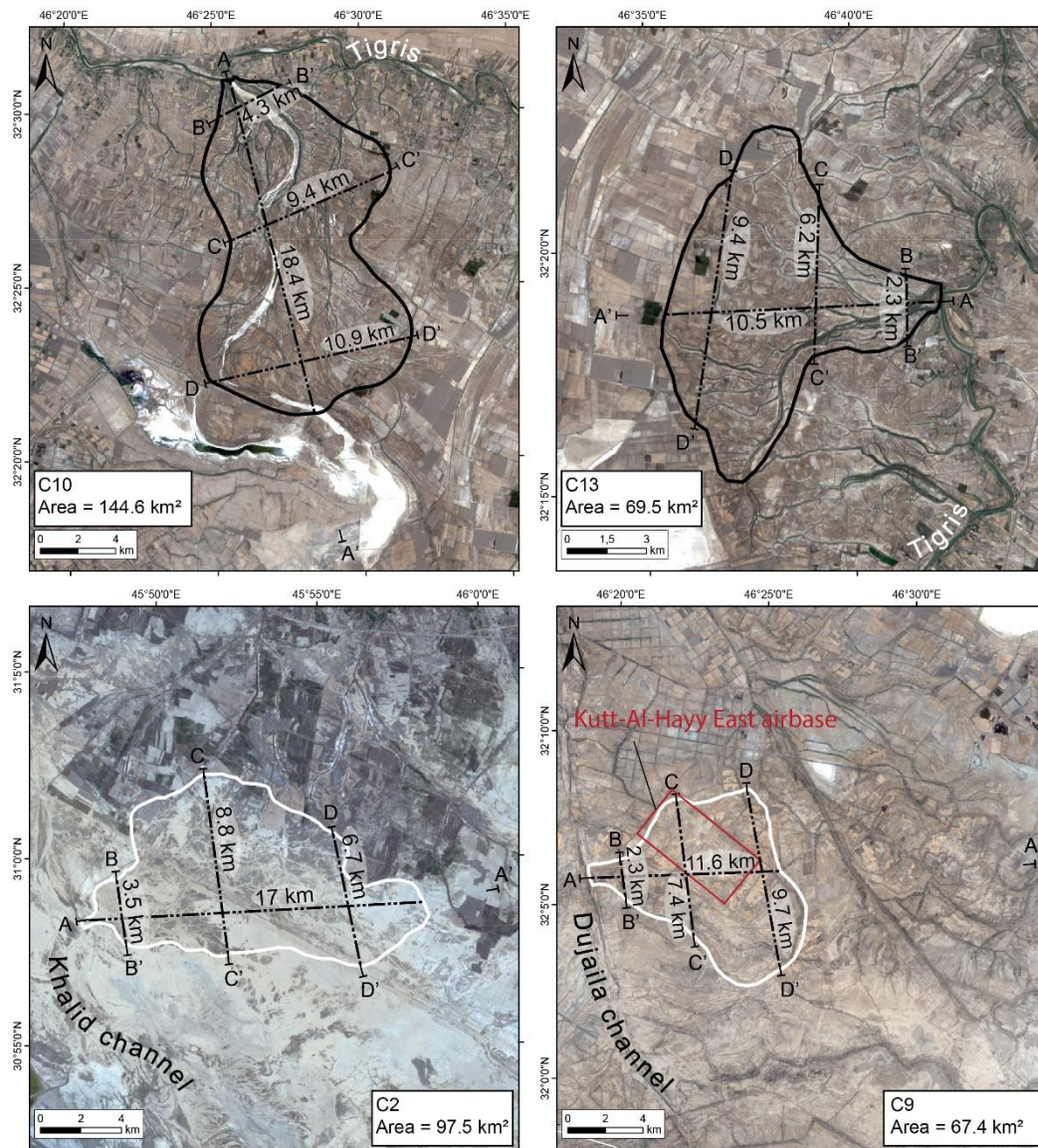


Figure 22 - Example of active (C10 and C13) and abandoned (C2 and C9) crevasse splays recognized in the area. The traces of altimetric profiles shown in Figures 23 and 24 are reported: AA' = along-dip profiles, BB' = cross-direction profiles of the proximal sector, CC' = cross-direction profiles of the middle sector, DD' = cross-direction profiles of the distal sector.

Indeed, among the recognized active crevasses, those named C10 and C13 are located along the Tigris Rivers, but their shape and spatial development are deeply different. The first one has mainly dip-direction extension while C13 is substantially developed along the cross-direction (**Figure 22**). The same divergence can be appreciated in the elevation data. Generally, both crevasses show along-dip sections with an emphasized convex-up profile at the proximal sector, gradually flattening floodplainward. On the contrary, the cross-sections show the notable differences between C10 and

C13 due to the different activity of their crevasse channels and the relative distribution of sediments (**Figure 23**). While C10 points out a more homogeneous channel activity and spatial distribution of sediments (**Figure 23A**), the proximal and middle cross-sections BB' and CC' of C13 display the main active channels in the southern part (**Figure 23B**). Anyway, each cross-section at the proximal, middle, and distal sectors broadly display the progressive decrease floodplainward of the crevasse deposits thickness (**Figure 23**). The thickness of C10 and C13 deposits are quite different: in C10, the proximal deposit is about 2.5 m thick, the middle deposit is 3 m, and the distal one reaches the lowest thickness with 1.5 m, while in C13, the proximal deposit is thicker (about 3 m), the middle deposit is about 2 m thick, and the distal deposit is quite similar to C10 one.

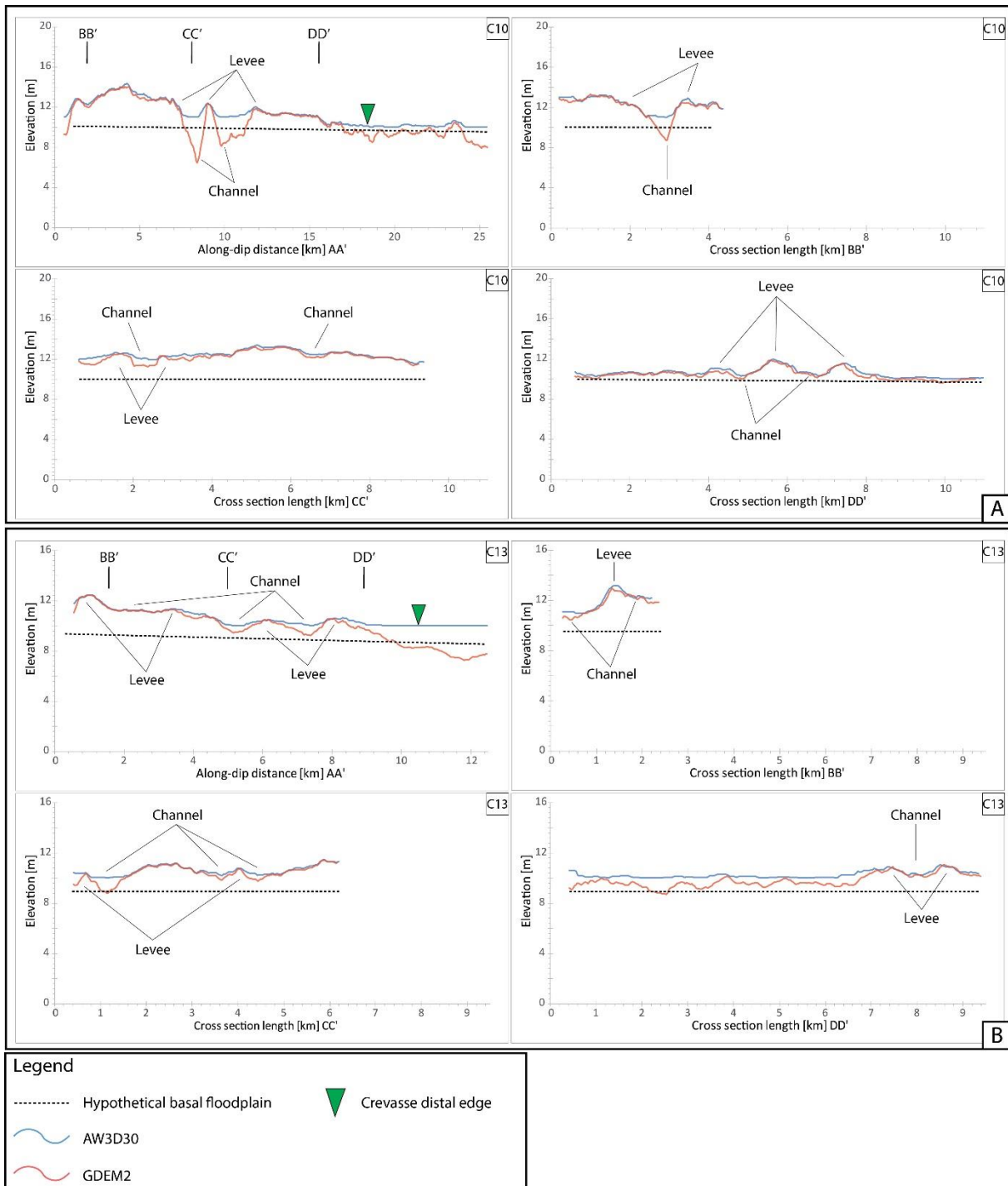


Figure 23 - Altimetric profiles based on the elevation data of both AW3D30 (blue line) and GDEM2 (red line) datasets. Moving averaged values range from 10 up to 20 m. Location of the profile traces is reported in Figure 22. A) Altimetric profiles for the crevasse C10; B) Altimetric profiles for the crevasse C13.

The two examples of abandoned crevasse splays C2 and C9 present, as expected, rather different geomorphological and geometric characteristics with respect to the active crevasse before described. C2 is well recognizable mainly in dip-section, while the cross-sections do not preserve the typical convex-up shape (**Figure 24A**). C9 shows a less convex-up profile of the deposit in the along-dip and the cross-section CC' (**Figure 24B**). Both C2 and C9 proximal deposits show a low thickness of about 1–2 m, the middle deposits are thicker reaching 3.5–4 m, while the distal deposits are 1.5–2 m thick. Nevertheless, a significant difference can be appreciated in the along-dip sections: the active crevasse C10 and C13 have an elevated proximal sector, directly connected to the above-floodplain levee of the

parent channel (i.e., the Tigris River). On the contrary, the proximal sector of abandoned crevasse C2 shows a low elevation, seemingly disconnected to the abandoned Khalid channel, while C9 still preserves the above-floodplain elevation of the Dujaila channel.

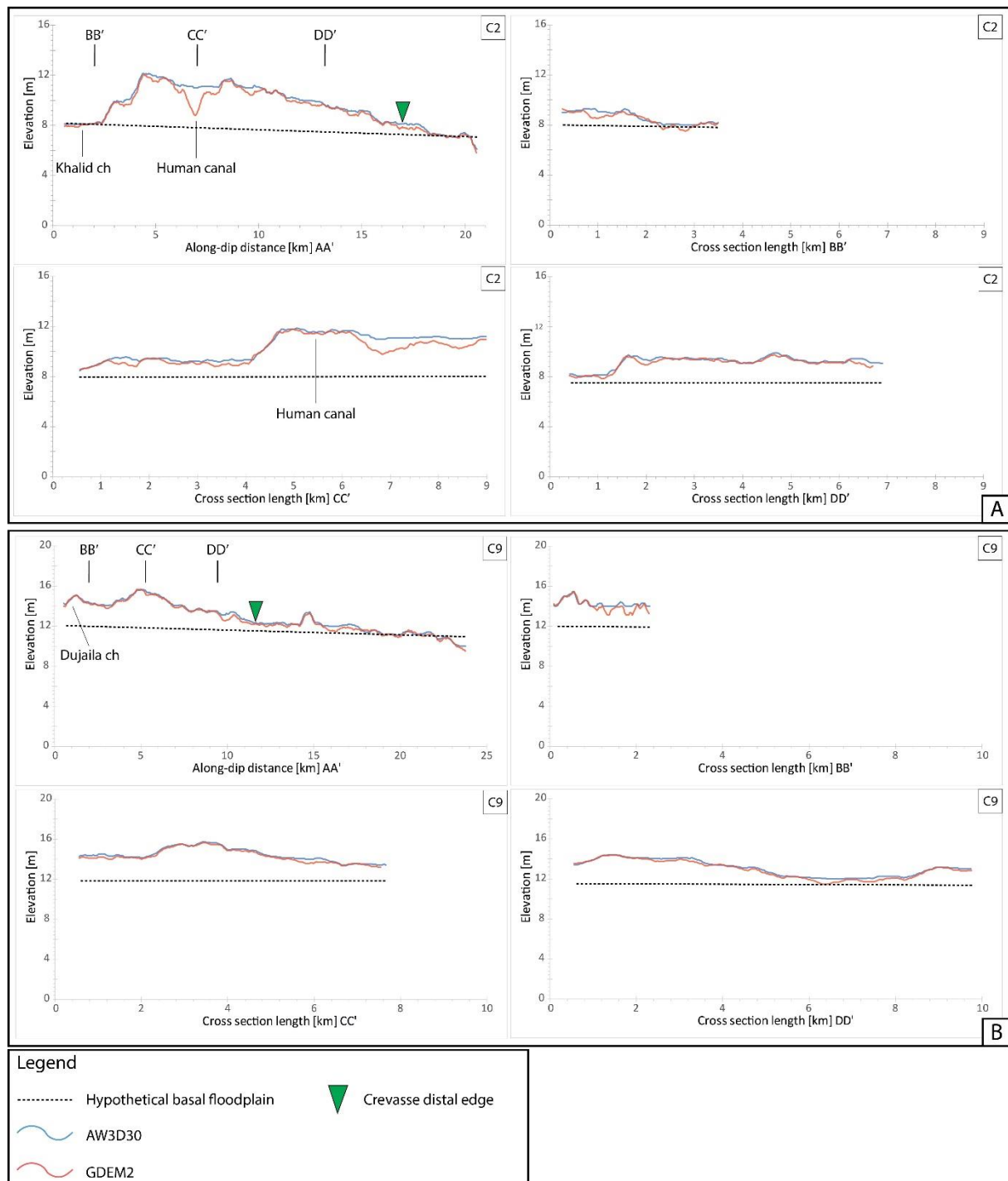


Figure 24 - Altimetric profiles based on the elevation data of both AW3D30 (blue line) and GDEM2 (red line) datasets. Moving averaged values range from 8 up to 20 m. Location of the profile traces is reported in Figure 22. A) Altimetric profiles for the crevasse C2; B) Altimetric profiles for the crevasse C9.

6.1.2 Multispectral satellite imagery analysis

NDVI and CR

The computation of the NDVI index and the CR improved the identification of crevasse splays, especially assessing the mobility of crevasse channels, the spatial distribution of the finest sediment and comparing the channelized/unchannelized flow. The NDVI has been classified into five classes (the lowermost value without a colour) (**Figure 25**). In this way, the vegetation cover is highlighted in the areas where is more abundant and with a higher density, for example along the riverbanks, within the croplands, and the crevasse splays. The NDVI does not discern which kind of vegetation we are looking (i.e., crops, riverine vegetation, or marshland), although the highest values have been recognized in the marshland areas.

The most evident difference in the NDVI computation is the occurrence of vegetation on active and abandoned crevasses, leading to discern their state of activity. Bearing in mind the influence of rainfall seasonality, the most reliable results were obtained with the images of the wettest period. Nevertheless, both examples of active crevasses (i.e., C10 and C13) show higher NDVI value than the abandoned ones (i.e., C2 and C9). Indeed, considering the NDVI during the wettest period, the highest values occur along the crevasse channels in the proximal and middle sectors of C10 (**Figure 25**). Otherwise, the NDVI values are higher in the southern part of C13, where the crevasse channels are largest. The occurrence of vegetation in the abandoned C2 and C9 is mainly due to the crops and human canals surrounding the crevasses.

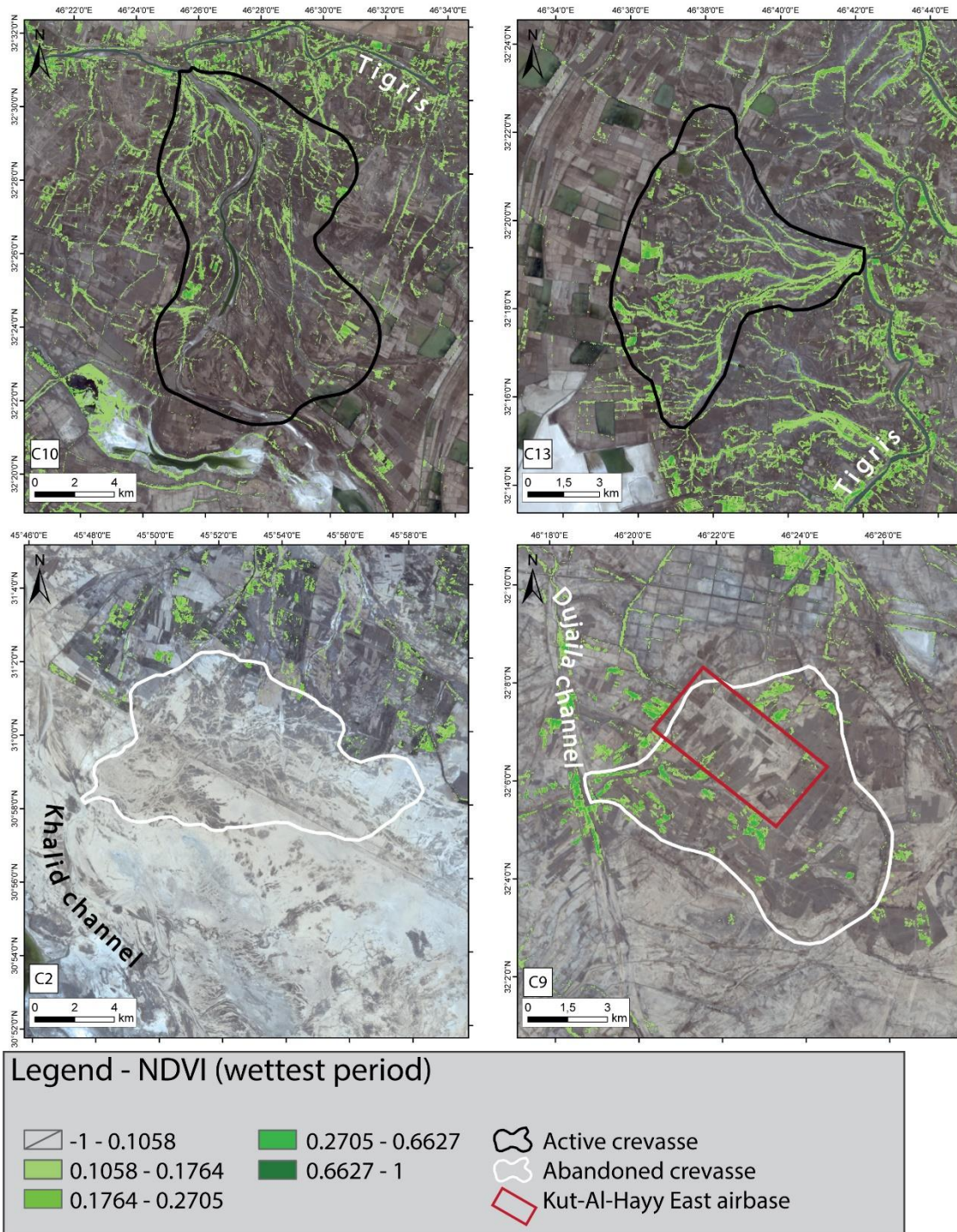


Figure 25 - Spatial distribution of NDVI, during the wettest period, for the active (C10, C13) and the abandoned (C2, C9) crevasse splays.

The state of activity of crevasse channels is estimated also through the CR, which is classified into fifteen classes for the wettest period (**Figure 26**). As for the NDVI, the lowermost class has not a colour for emphasizing the areas with higher clay content. This index is useful to recognize the in-channel clay like the last deposits of a flood event when the floodwater goes back toward the parent channel due to the decrease of river discharge below the bankfull capacity. Anyway, the basinward overland flow could be captured into the crevasse channels or remnant depressions, like in C10, depositing the finest suspended load. The highest values of CR are also on the banks of crevasse channels, leading to the identification of their levees. The abandoned C2 and C9 (**Figure 26**) seem to be completely free of clay

deposit, except for northern middle sector of C2, where the human activity can be detected, and the spotted areas in the proximal sector of C9. A preliminary re-shaping of the crevasse splays can be made starting from these elaborations. Indeed, both NDVI and CR unveil a larger areal extension of the splays, especially in the active C10 and C13.

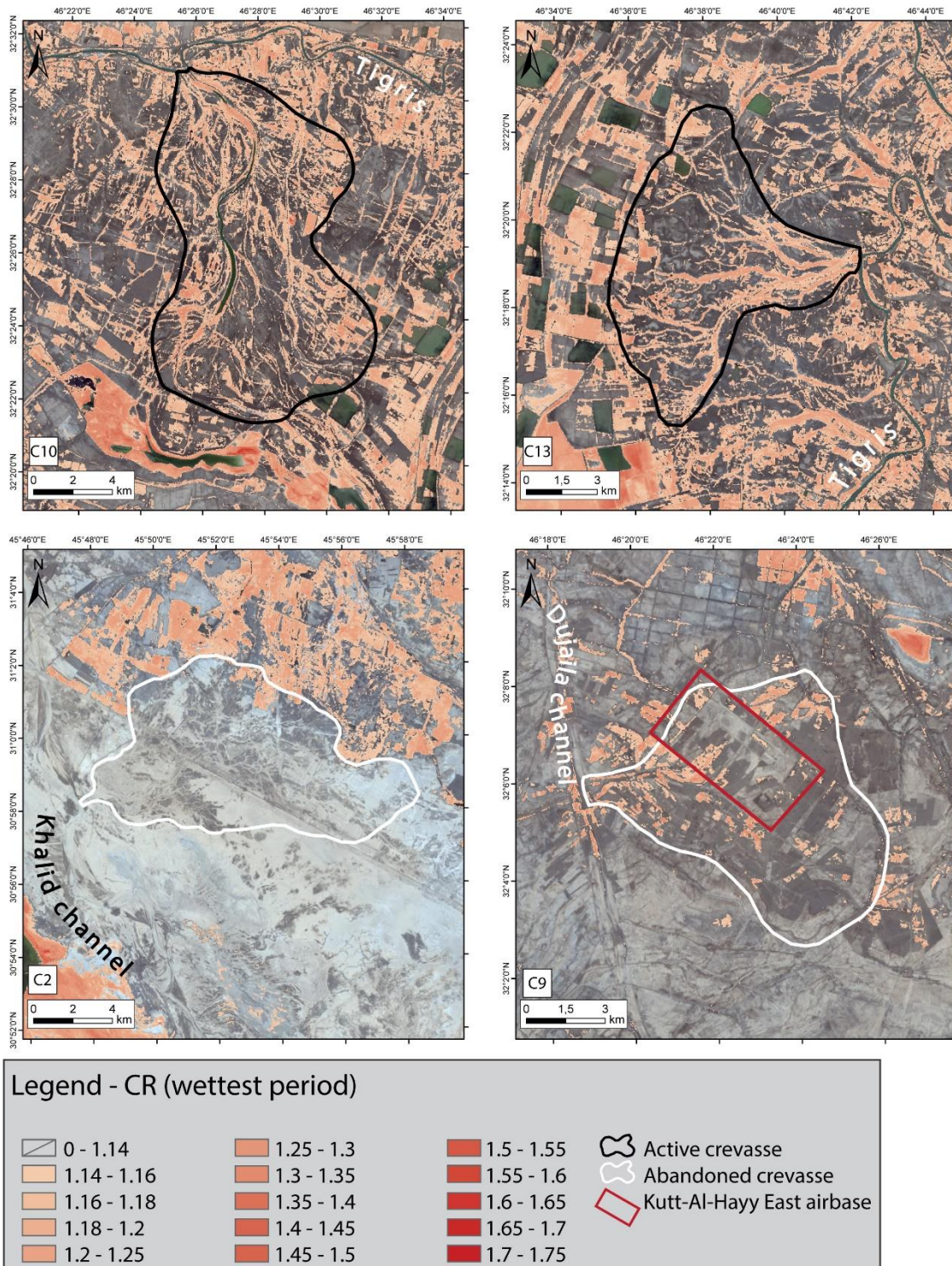


Figure 26 - Spatial distribution of the CR, during the wetttest period, for the active (C10, C13) and the abandoned (C2, C9) crevasse splays.

SUPERVISED CLASSIFICATION

Among different iterations for each classifying method, the most accurate results have been selected considering the highest OA and K values as well as the UA and the PA, summarized in **Table 9**. The outcomes of the different classification methods will be described in the following sections, for emphasizing the most suitable approach to detect the features associated with the avulsion process in the study area.

Table 9 - Accuracy of each ROIs derived from the different classification methods applied in this thesis.

		Driest period		Wettest period	
		OA (%)	K	OA (%)	K
Mahalanobis		66.0026	0.5148	67.9402	0.5755
Maximum Likelihood		69.1801	0.5636	67.7534	0.5925
Minimum Distance		62.0184	0.4607	58.4480	0.4841
SAM		61.2776	0.3676	63.9497	0.4655
		Driest period		Wettest period	
		PA (%)	UA (%)	PA (%)	UA (%)
Mahalanobis	Active channel	69.18	90.88	76.73	70.07
	Active levee	54.24	17.49	24.42	35.15
	Active deposit	67.55	98.05	68.29	94.92
	Abandoned channel	54.22	73.83	46.17	68.20
	Abandoned deposit	72.26	57.31	84.92	73.18
Maximum Likelihood	Active channel	79.92	99.74	79.65	99.09
	Active levee	23.73	46.67	37.68	60.47
	Active deposit	71.17	98.97	66.42	96.71
	Abandoned channel	63.91	96.24	52.63	88.71
	Abandoned deposit	73.29	78.49	74.40	98.85
Minimum Distance	Active channel	70.56	83.15	88.56	79.29
	Active levee	34.75	14.49	47.79	29.75
	Active deposit	66.46	96.46	45.80	91.24
	Abandoned channel	28.91	87.29	66.51	89.39
	Abandoned deposit	69.36	76.48	46.42	95.96
SAM	Active channel	71.82	58.48	75.00	77.37
	Active levee	27.97	19.88	11.37	41.22
	Active deposit	76.00	79.76	84.82	64.04
	Abandoned channel	7.50	24.24	54.55	79.17
	Abandoned deposit	25.05	26.02	19.09	97.78

Mahalanobis - In **Figure 27**, the classification of wettest period discerns active channels, levees and deposits, despite some areas are classified as an abandoned channel, especially in the proximal sector of C10 and along the active channel banks of C13, or as an abandoned deposit in the middle sectors of C10 and C13. In spite of the good detection of channels, levees, and deposits, their recognition beyond the C10 and C13 edges does not prove helpful for re-mapping them. Anyway, both distal sectors reveal the continuation of a crevasse channel (**Figure 27**). Therefore, C10 and C13 can be re-mapped for including the respective crevasse channels after this elaboration. The abandoned crevasse C2 is better classified than C9, where channels and deposits are detected mostly in the proximal and middle sectors (**Figure 28**). The distal sector is recognized exclusively as an abandoned channel even beyond the edge, resulting in unhelpful for eventually re-mapping the crevasse limits. Only the northernmost edge of C2

delimits the classified crevasse channels and deposit. Some spurious pixels without any typical shape are categorized as active channels, largely in the proximal and middle sectors, leading to an erroneous classification. A completely different detection occurs on C9, where most of the area is classified as active deposit and active channel, but without any typical shape.

Maximum Likelihood - This classification method provides the highest OA for the driest period, well-identifying each ROI (**Figure 27**). As for the Mahalanobis classification, the channels, levees, and deposits of C10 are correctly classified and allows a more accurate landform re-mapping in the distal sector with respect to the Mahalanobis classification method. Indeed, the same channel beyond the southern margin is still recognized, as the continuation of the deposit in the south-western margin, up to the backswamp. This last seems to be fed by the main crevasse channel (the white one in the optical imagery of **Figure 22**), allowing the re-shaping of the southern margin enclosing the backswamp. Moreover, the Maximum Likelihood classification clarifies the occurrence of another crevasse channel (the white arrow in **Figure 27**), which flows along the eastern margin of C10, up to the three black arrows. The same close classification is appreciable also on C13, where the edge of the distal sector can be easily re-mapped, according to the black arrows pointed to the scattered deposits. The re-shaping must also consider the aforementioned channel, out to the crevasse margin, which flows southward. The discerning between crevasse channels and the Tigris River is better in this method than in the Mahalanobis. Even if the Tigris bankfull discharge is not classified as active channel neither in Mahalanobis nor in Maximum Likelihood, this last classification looks more filtered, leaving roughly unclassified the river levee and mainly focusing on the crevasse features. The abandoned crevasse C2 is better classified than C9, like in the Mahalanobis classification (**Figure 28**). Indeed, this method perfectly recognized the abandoned channels and, partially, the deposit of C2, highlighting a necessary re-mapping of the southern margin (i.e., the black arrows in **Figure 28**). As for the active crevasses, the Maximum Likelihood is a more-filtered classification, leading to better identify the ROIs and improve the mapping of the landforms. Anyway, the same observation is not possible for the C9, where spotted areas are identified as active levees and active deposit.

Minimum Distance - For the active crevasses C10 and C13, the active channels and deposits are correctly classified in the driest period (**Figure 27**), leaving the levees unclassified. The classified areas are more selected, and the re-shaping of the crevasses is more straightforward. As for the previously described classification methods, the distal sector of C10 unveils the occurrence of the deposit and a channel beyond the traced edge, but even the western distal margin displays the deposit and a crevasse channel beyond the mapped limit (the black arrows in **Figure 27**). The Minimum Distance also displays the contribution of the eastern crevasse (the white arrow in **Figure 27**). A similar re-mapping is practicable on C13, where the distal edge may be shifted westward and southward following the deposits and the crevasse channels here detected. The features of abandoned C2 and C9 crevasses are classified differently (**Figure 28**). One more time, C2 shows up the best fitting with the ground: the abandoned channels are perfectly recognized, while the abandoned deposit is lesser identified, only in some areas. The northern middle sector is classified also like the active levee, probably because of the occurrence of the crops beyond the margin. A poor re-shaping is available for the southern edge of the proximal and middle sectors (the black arrows in **Figure 28**), whereas the distal sector insufficiently shows the channels and deposit beyond the margin. Again, most of C9 seems wrongly classified: only spotted areas are recognized as abandoned channels, without any typical shape, and as active deposits, especially on the edge of the airbase. Thus, the re-mapping of C9 is unattainable.

SAM - The last classification method used in this work provided less satisfactory results. Indeed, the active C10 and C13 are mostly classified as active deposit and secondary as active channels and levees in the wettest period imagery (**Figure 27**). Furthermore, the Tigris bankfull is classified as an active crevasse channel, like the other watercourses in the area not connected to the avulsion processes. The areas recognized as active deposit are in and out the C10 and C13 margins, forbidding an intuitive re-mapping of the crevasses. Anyway, the abandoned C2 looks roughly identified, especially for the abandoned channels, but the deposit is mainly classified as active (**Figure 28**). A partial re-shaping is practicable alongside the southern edge and in the distal sector (the black arrows in **Figure 28**). The *SAM* classifier does not improve the detection of C9, where most of the area is recognized as an active deposit.

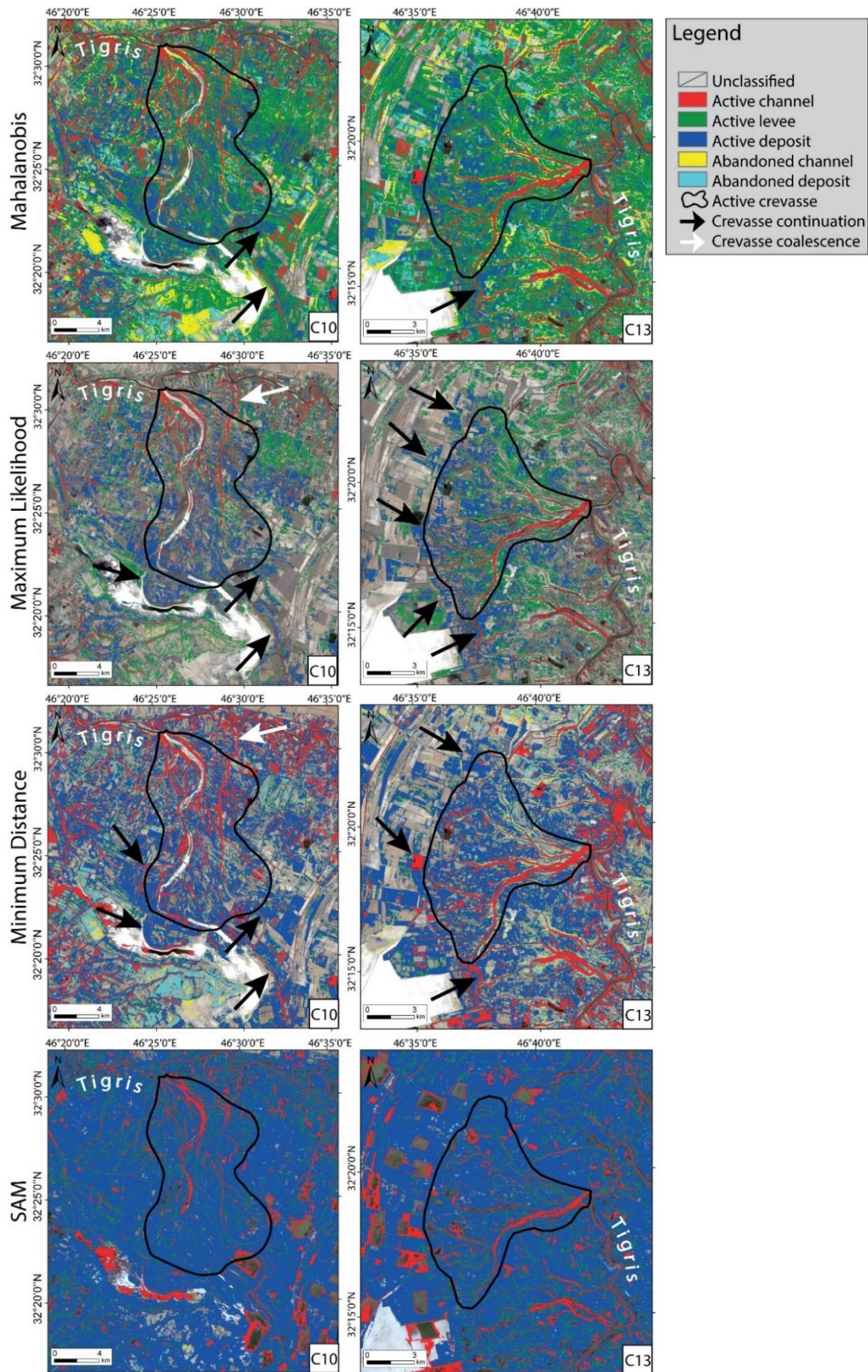


Figure 27 - Classified active crevasse plays (C10, C13) using four classification methods. For the Mahalanobis and Minimum Distance, the wettest period is shown, while for the Maximum Likelihood and SAM is the driest period.

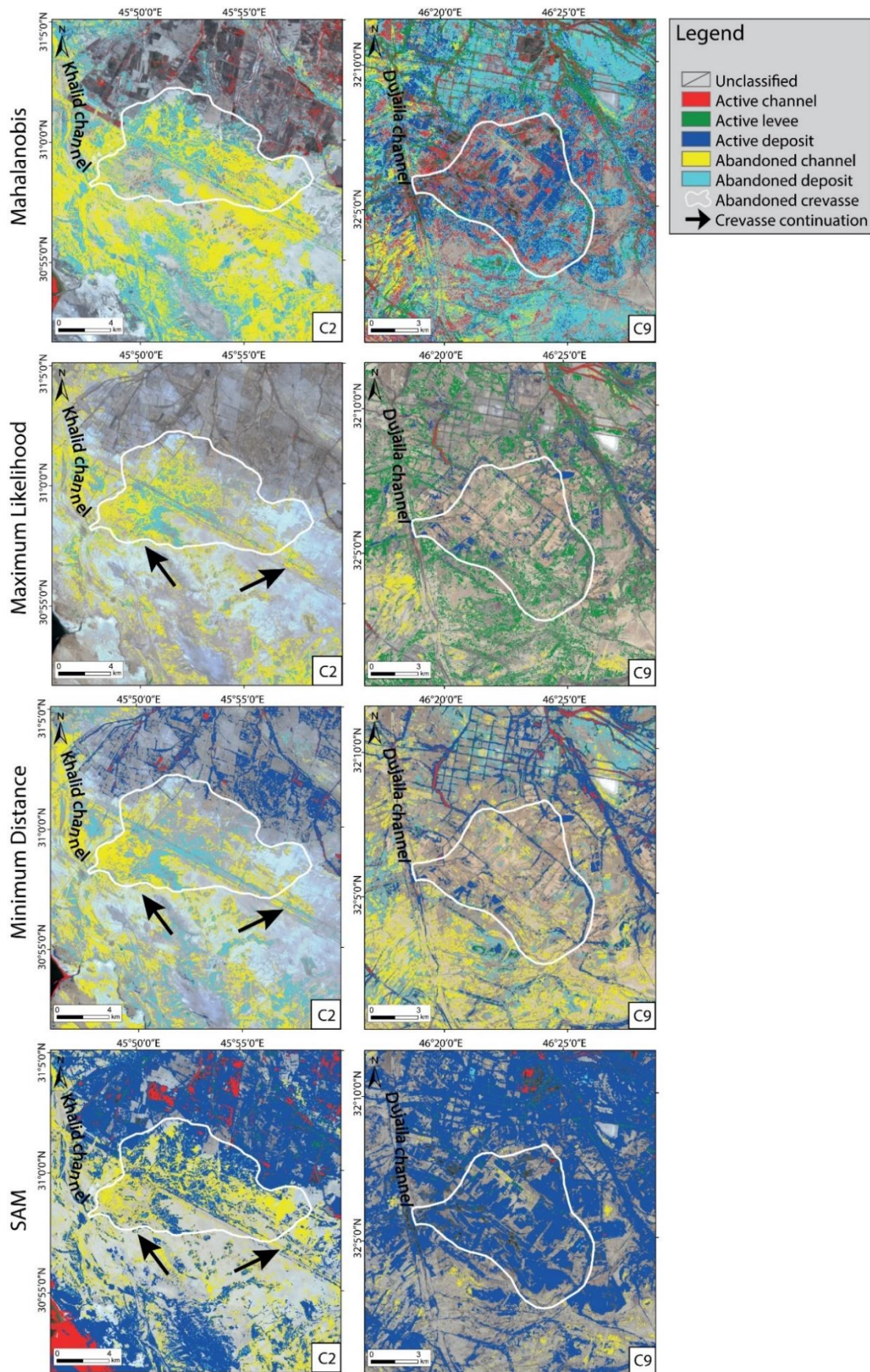


Figure 28 - Classified abandoned crevasse splays (C2, C9) using four classification methods. For the Mahalanobis and Minimum Distance, the wettest period is shown, while for the Maximum Likelihood and SAM is the driest period.

6.2 Geomorphological mapping at Tell Zurghul archaeological site

The archaeological site of Tell Zurghul is located about 40 km north-eastward from the city of Nasiriyah, in the LMP. It is known also as Nigin and composed the State of Lagash with the homonym city of Lagash and the city of Girsu (**Figure 29**). The State of Lagash developed between the half of the Third Millennium BC and the end of the Third Millennium BC when a slow decline and abandonment of the settlement was caused by the fall of the III Dynasty of Ur.

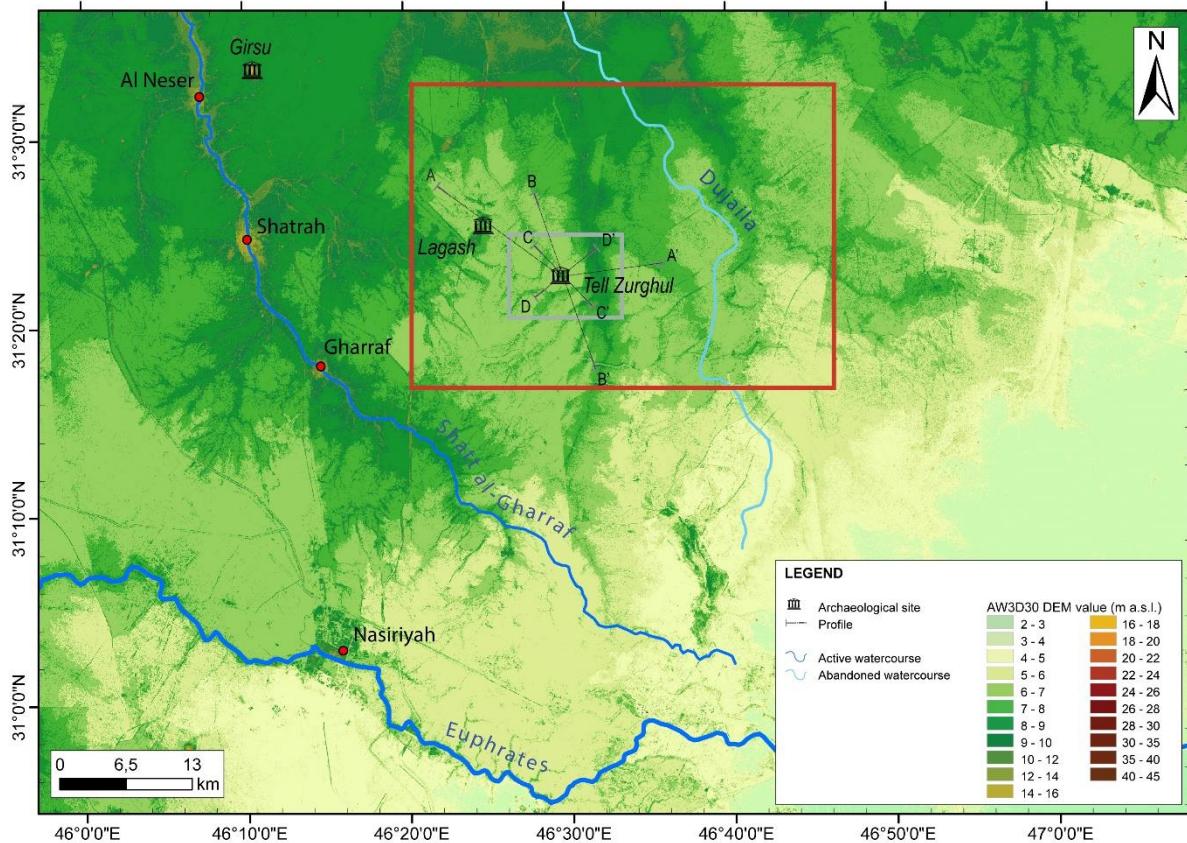


Figure 29 - Localization of the reconstructed area surrounding the archaeological sites of Lagash and Tell Zurghul. The red rectangle is detailed in Figures 30 and 31 while the grey rectangle is detailed in Figure 33.

The site has an altitude range from 8 up to 15 m a.s.l. and is surrounded by the Holocene abandoned floodplain of the Dujaila channel eastward and by the still-active floodplain of the Shatt al-Gharraf westward. Since these two main watercourses belong to the Tigris River, Tell Zurghul waterscapes is mainly influenced by the easternmost main river of the LMP. The topography typically reflects the features of a distributary floodplain, where both the natural fluvial and anthropic landforms are topographically higher than the surrounding flat floodplain. This last preserves active and relict fluvial landforms, such as channels and avulsion processes, and aeolian active landforms like blowouts, where the relict forms of the abandoned Dujaila channel are partially obliterated. The active channels of the Shatt al-Gharraf system principally preserve a dendritic meandering pattern, while the Dujaila system channels show a similar high sinuosity but with a more anastomosing pattern (**Figure 30**). Moreover, the anastomosing pattern of the Dujaila preserves evidence of high lateral mobility through several examples of scroll bars along its watercourse.

The western sector is intensively farmed (as clearly shown by the NDVI in **Figure 31**), and the main human impact is represented by several canals with a herringbone pattern, like in the north-west sector and North of Tell Zurghul. Anyway, the straight course of these canals is another peculiar feature, which can distinguish between natural channel and human-made canal. Indeed, the straight

course of the canals can reach several kilometres of length (i.e., up to 3-5 km), while the straightening course of the channels rarely reaches 2 km of length in the area.

The anthropic features over the western sector are also represented by the archaeological site of Lagash (about 4 km²) and Tell Zurghul (less than 1 km²), well recognizable thanks to their elongated ellipsoid shape and lacking vegetation. The wider one, Lagash, is surrounded by wetlands of about 40 km², which size is strongly influenced by the rainfall seasonality (**Figure 30**). As for the canals, the archaeological mounds are topographically elevated, favouring their recognition along the profiles traced in **Figure 29**.

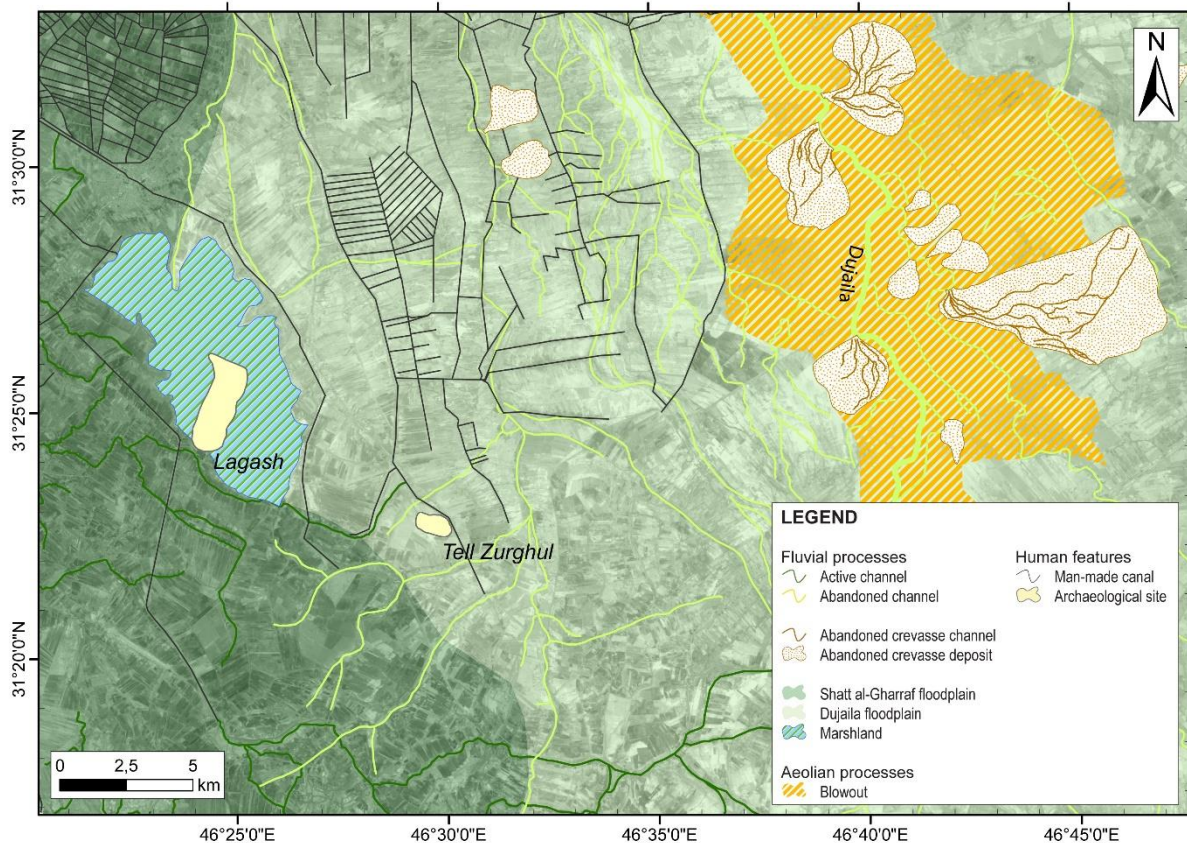


Figure 30 - The map of fluvial (principally channels and avulsions, both active and abandoned) and aeolian processes of the Shatt al-Gharraf and Dujaila floodplains, in addition to the anthropic features.

In the easternmost sector, where the vegetation is scarce as resulted from the NDVI (**Figure 31**), the aeolian processes prevail forming a wide blowout of about 240 km². The low-angle surface and the weak substrate, composed mainly by sand (as confirmed by the CR in **Figure 31**), make this zone susceptible to salt weathering and deflation. Anyway, several examples of abandoned crevasse splays are here recognized along the Dujaila channel, which sizes vary from thousands of square metres up to 25 km². The wider ones still preserve their distributary channel systems, while the smallest crevasse splays are recognizable exclusively for their fan-shaped or their location in the outer bank of a meander belt. Despite the aeolian re-working of the abandoned fluvial deposits of the Dujaila channel, they still preserve their peculiar shape and spatial distribution, while in the central sector the increase of vegetated areas corresponds to the increase of man-made canals and the decrease of preserved crevasse splays and channels.

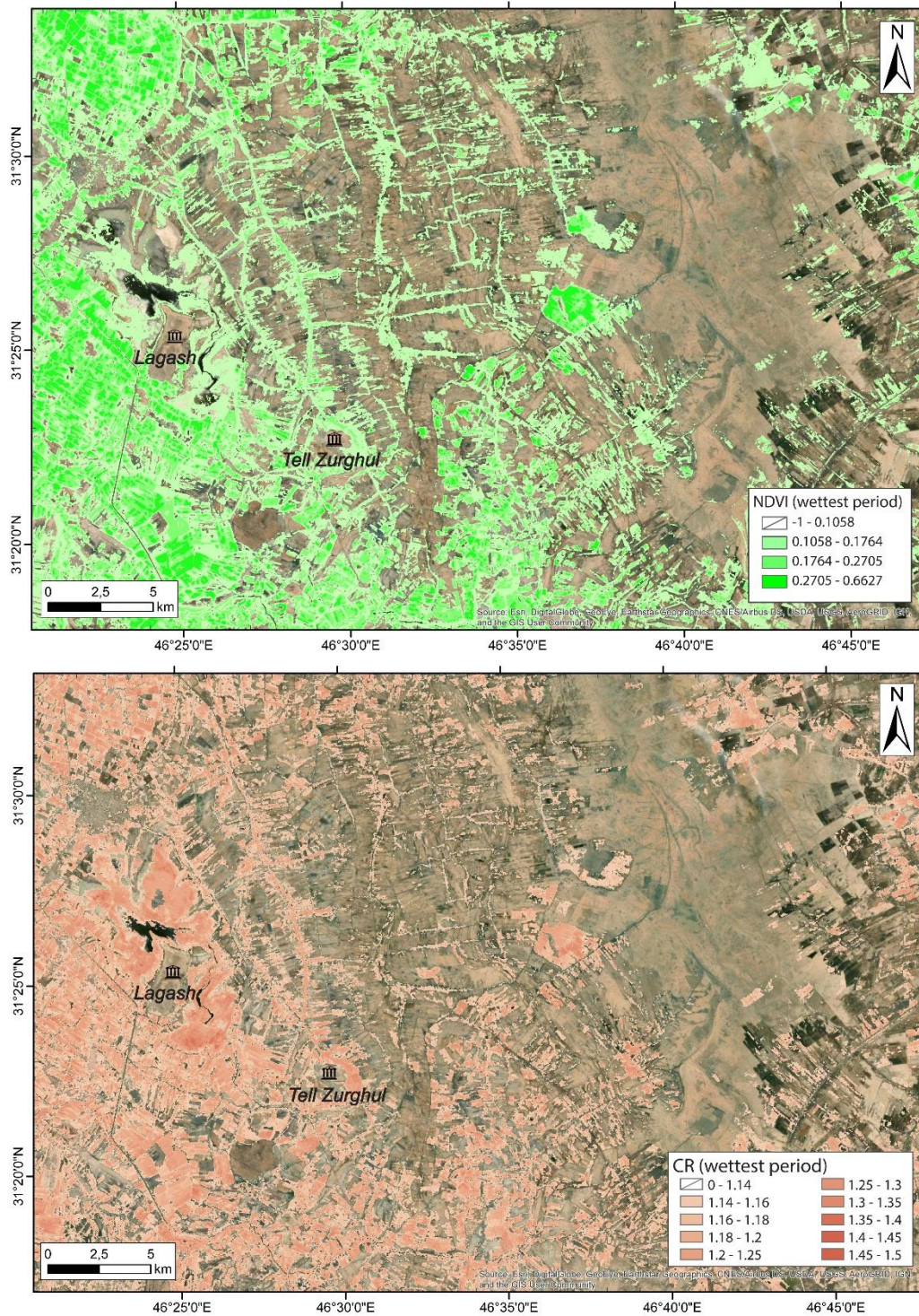


Figure 31 - The spatial distribution of clay minerals (CR) and vegetation (NDVI), both computed for the wettest period. The areas with the highest values of CR and NDVI correspond to the croplands.

The topographic analysis of the micro-relief has been carried on through four altimetric profiles in order to define the spatial distribution of fluvial and anthropic deposits: AA' and BB' profiles are about 20 km length and used the most recent elevation data of AW3D30 (i.e., 2018), while the profiles CC' and DD' are shorter (less than 10 km) and adopted the elevation data of the CSK-DEM. All the profiles are traced in the area where the avulsion processes are not preserved; thus, the identified deposits are exclusively distinguished among channel, floodplain and anthropic (man-made canals and mounds).

Starting from the longer AA' and BB' profiles (**Figure 32**), the elevated topography of both anthropic and fluvial landforms is clearly highlighted after the application of the moving average filter. The most elevated anthropic features are the archaeological sites of Tell Zurghul and Lagash, which are represented as a sort of isolated mound with a flat top, surrounded by the flat floodplain; instead, the elevation of man-made canals is less evident and sometimes is indiscernible from the floodplain. The elevation of the abandoned channels is more evident, especially alongside the AA' profile, which reaches the two branches recognizable in the AW3D30 between Tell Zurghul and the Dujaila channel. Alongside the BB' profile, the topography of the active channel resembles the so-called “baguette levees” configuration, described by Jotheri (2016). Indeed, the active channel cuts the levees of an abandoned channel (**Figure 32A**), resulting in topographically lower than the abandoned channel.

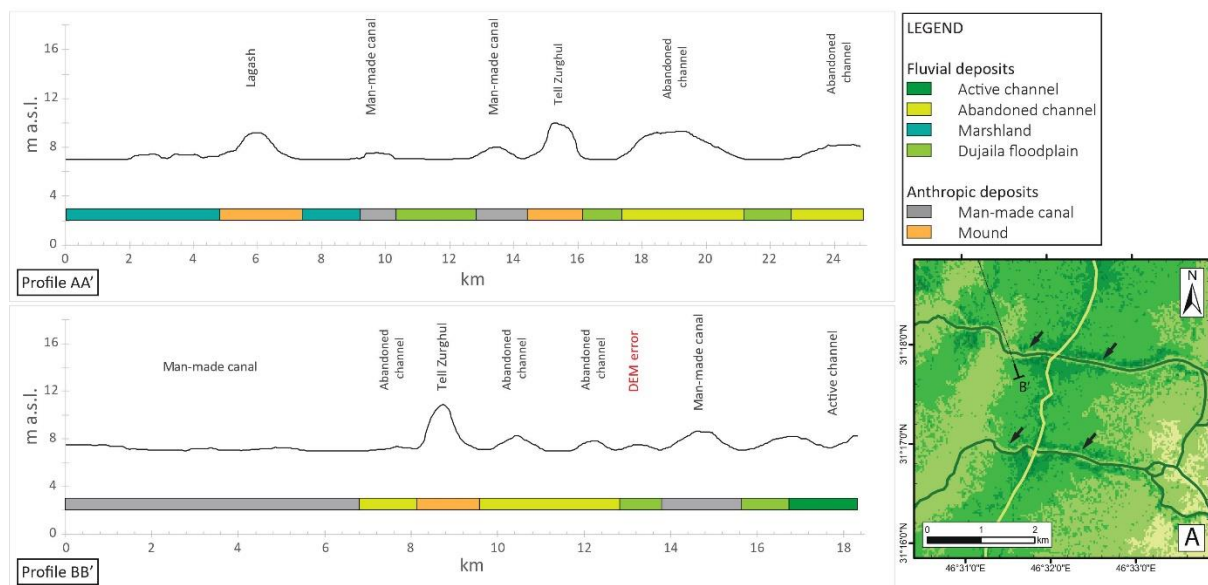


Figure 32 - Altimetric profiles based on the elevation data of AW3D30 dataset. Moving averaged values is 20 m. Location of the profile traces is reported in Figure 29. A) The active channel of profile BB' where the baguette levees configuration occurs, pointed out by black arrows.

The CSK-DEM of Tell Zurghul has been adopted for improving the topographic analysis of the micro-relief through the CC' and DD' profiles (**Figures 33, 34**), where however the application of a moving average filter does not sufficiently smooth the elevation data for detecting fluvial and anthropic features. Indeed, the CSK-DEM presents several no-data areas, especially along the south and east margins where the topography is higher. Moreover, the “human-noise” due to the farming activities is widespread over the entire DEM and can be easily identified by the swale-and-ridge pattern perpendicular to both sides of the man-made canals, most likely due to the ploughing. Thus, both the profiles still preserve this effect after the smoothing moving average filter. The topographic decrease of the heights follows a SE-NW trend, reflecting the occurrence of the marshland in the north-west sector and the presence of several abandoned channels in the eastern area. The main abandoned channel is N-S oriented and can be easily identified also on the AW3D30 (i.e., the channel between Tell Zurghul and the Dujaila channel). Despite the no-data areas and the human-noise, the topography of the entire archaeological area of Tell Zurghul well represents the two main mounds called Mound A (the highest one) and Mound B (the lowest one) in the centre and the southern margin of the archaeological area, respectively.

Despite the low smoothing, the topographic evidence of the Mound A is the most visible alongside the profiles CC' and DD'. Comparing the heights among AA' - BB' and CC' - DD' profiles, the vertical accuracy of the AW3D30 is lower than CSK-DEM: Mound A is about 15 m a.s.l., as shown by CC' and

DD', despite the moving average filter decreases its height, whereas Tell Zurghul is about 12 m along AA' and BB'. Anyway, the AW3D30 profiles better represent the typical "pyramid-trunk" of Lagash and Tell Zurghul mounds (especially along the profile AA' in **Figure 32**), whereas the flat top of Tell Zurghul Mound A is lesser evident in CC' and DD' profiles. Besides the topographic evidence of Tell Zurghul, both the anthropic and fluvial landforms with the typical configuration above-floodplain are lesser recognizable alongside both CC' and DD' profiles. Indeed, the swale-and-ridge noise prevents the recognition of man-made canals or active and abandoned channels and the spatial distribution of the fluvial and anthropic deposits has been reconstructed considering the map in **Figure 30**.

Finally, it is worth to mention the topographic profile of the active channel in CC': the double-convexity due to the levees is clearly recognizable and partially reflects the conceptual sketch proposed in **Figure 14A**, despite the height above the floodplain is lower than 4 m.

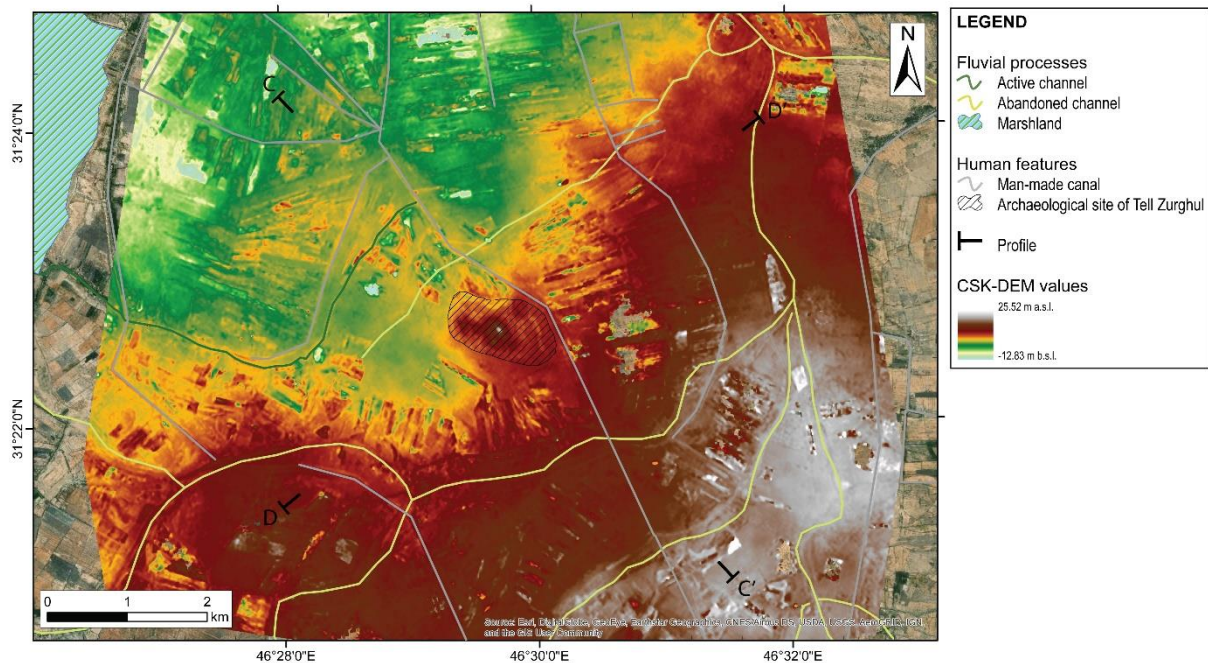


Figure 33 - The CSK-DEM of the Tell Zurghul area, where the recognized fluvial processes and human features are essentially channels and canals.

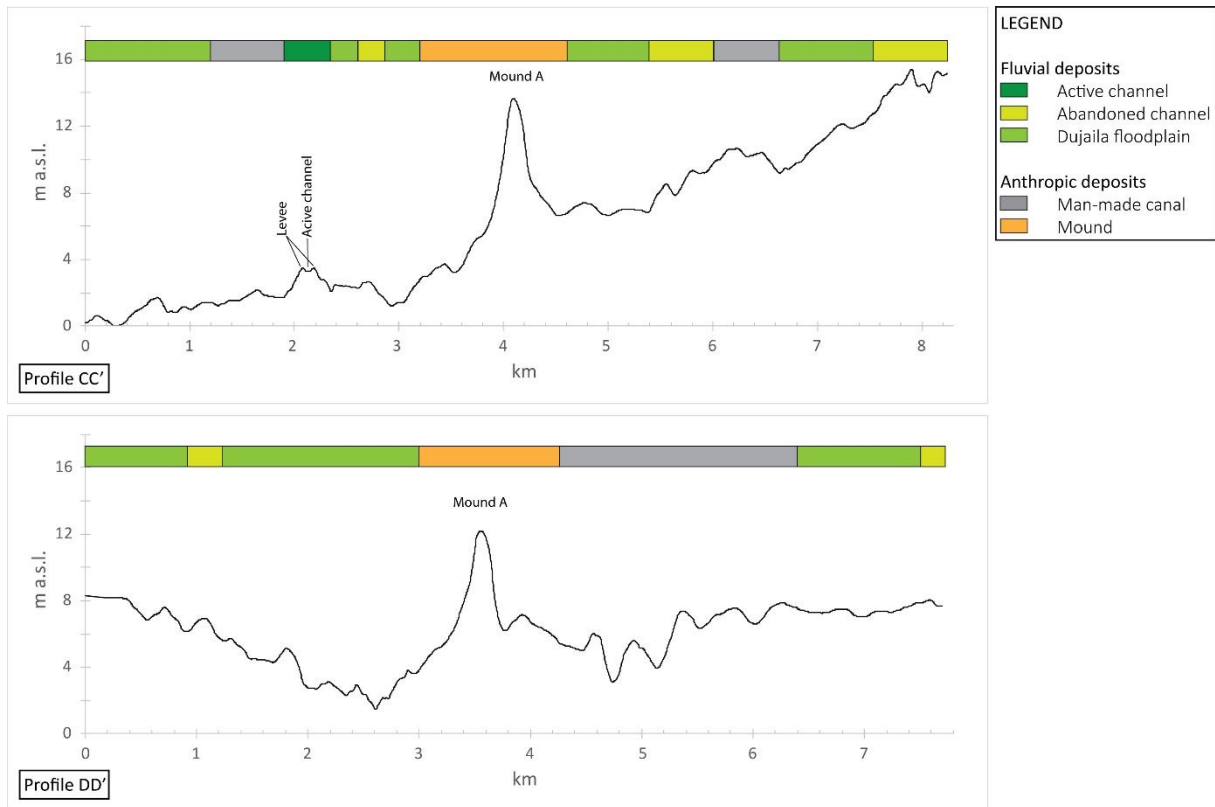


Figure 34 - Altimetric profiles based on the elevation data of CSK-DEM dataset. Moving averaged values is 40 m. Location of the profile traces is reported in Figure 29.

7. Discussion

The adopted methodological approach allowed to combine the data derivable from digital elevation datasets to the outcomes of satellite multispectral imagery analysis, for the detection and mapping of fluvial landforms and anthropic features in wide and remote areas such as the LMP. Moreover, the low relief increased the difficulties in detecting fluvial avulsion processes, but it facilitates the recognition of channels and anthropic features thanks to their above-floodplain configuration.

The target feature during the investigation of the entire LMP is exclusively the avulsion processes, which offering the challenge for proposing a completely remote sensing approach useful for detecting these specific features over a wide study area. Instead, the sample area of Tell Zurghul unravels the limits of the same approach over a restricted area, especially adopting a higher resolution DEM for the analysis of the micro-relief.

This chapter will discuss separately the results obtained during the investigation at medium- and large-scale (i.e., the avulsion processes and the geomorphological mapping of Tell Zurghul, respectively), in order to highlight the potentiality and the limits of each method considering the specific application.

7.1 Fluvial avulsion processes in lowland areas

This section forms the basis for the paper Iacobucci et., 2020. Specification:

Iacobucci, G.; Troiani, F.; Milli, S.; Mazzanti, P.; Piacentini, D.; Zocchi, M.; Nadali, D. Combining Satellite Multispectral Imagery and Topographic Data for the Detection and Mapping of Fluvial Avulsion Processes in Lowland Areas. *Remote Sensing*. 2020, 12, 2243

The very low relief of the study area increases the difficulties in discerning crevasse splays and their related landforms. In particular, the detection and mapping of the abandoned crevasses is quite challenging just adopting a single remote sensing method, especially where intense anthropogenic activities have altered the morphology of the study area. Thus, the combination of the topographic analysis of the micro-relief and the multispectral satellite imagery analysis successfully allowed recognizing crevasse splays, favouring, mainly for the active landforms, their mapping. The topographic analysis of the micro-relief mainly highlights the active crevasse splays, where the channels and levees are easily detectable when their height is above the deposit. Moreover, this is more easily detectable when the profile trace includes the surrounding floodplain, leading to better define the edge of the crevasse splay. Despite the crevasse channels and levees are frequently above the crevasse deposit, the height above the floodplain of the crevasse deposit is frequently the only characteristic for recognizing the abandoned crevasse splays in the micro-relief analysis. Indeed, the abandoned crevasse channels are unlikely distinguishable from the abandoned crevasse deposit, pointing out a probable re-working of the abandoned crevasse. Thus, the micro-relief analysis requires a combination with the multispectral analysis, which can enhance the recognition of either vegetation or clay occurrence. Indeed, both NDVI and CR are fundamental for discerning between active and abandoned crevasse splays, but also between channelized and unchannelized flow or for recognizing which crevasse channels is most likely under siltation. It is particularly true for the active crevasses (i.e., C10 and C13), where the occurrence of the vegetation mainly influences the channel sinuosity and so, the different spatial distribution of the deposit. Indeed, the crevasse splays are composed by various sub-fan-shaped deposits (i.e., single splays), each of which is due to the occurrence of a single flood event.

The spatial distribution of the crevasse channels, levees, and deposits allowed to recognize these sub-splays, arranging the entire crevasse into a hierarchical framework (**Figure 35**). The frequency and the intensity of the flood events decrease until the abandonment of the crevasse splays, leaving a relict landform, where deposits can be re-organized by aeolian processes.

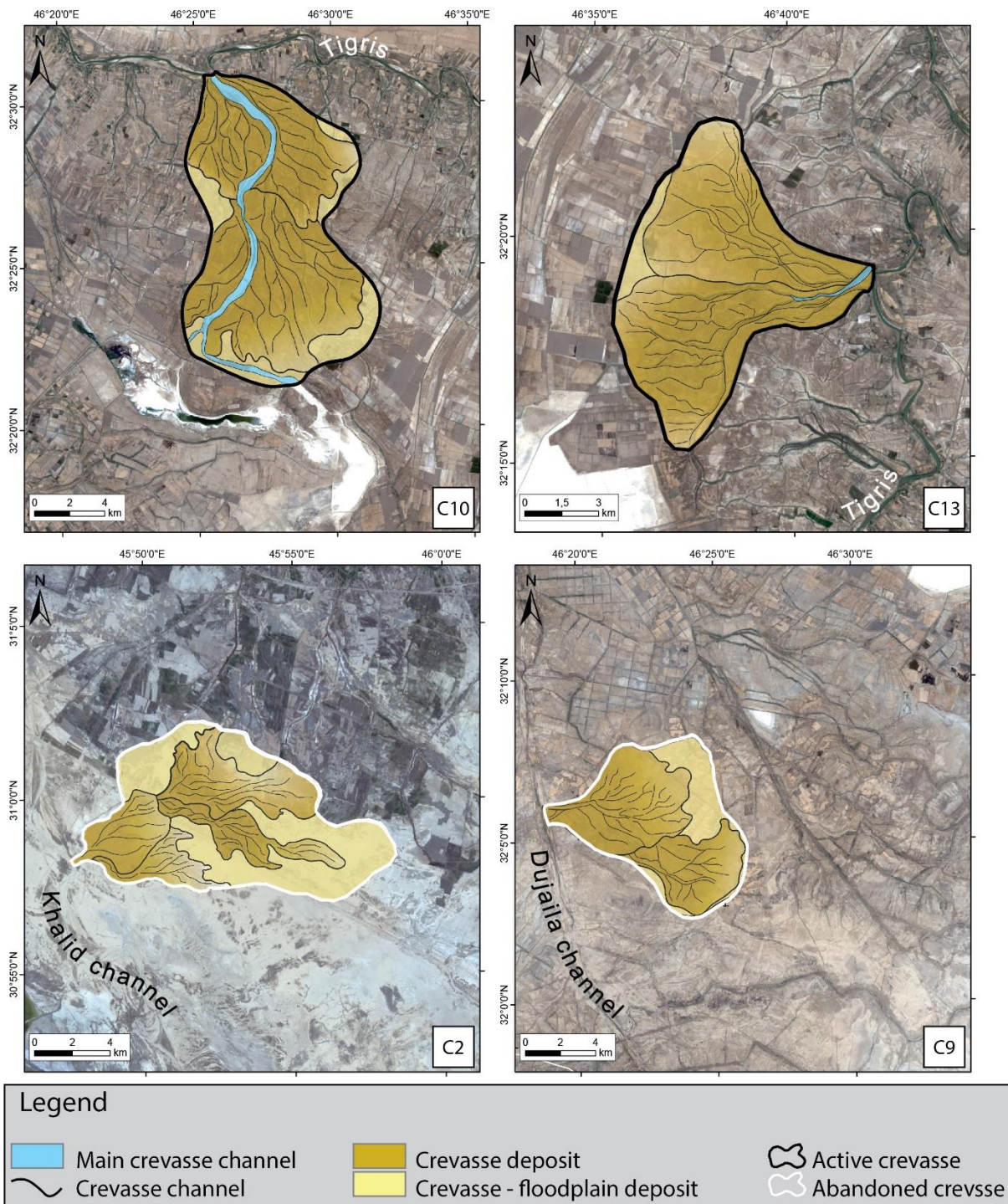


Figure 35 - The re-mapping of active (C10 and C13) and abandoned (C2 and C9) crevasse for highlighting the hierarchy of the flood event.

The SC through well-known methods is the last step for improving the re-mapping and understanding the deep difference in crevasse shape due to the hierarchy. For example, a wider proximal sector is due to the occurrence of different sub-splays and the coalescence among adjacent avulsion processes, which should lead to stretching of the crevasse channels, developing the crevasse

splay mainly in the along-dip direction. The along-dip development is also due to the depth of crevasse channels: deepest crevasse channels are mainly in the proximal and middle sectors, preventing the overflow, while in the distal sector the crevasse channels are shallow, favouring the overflow (like in C10).

Starting from the micro-relief analysis, a common geometric altimetry scheme can be tentatively supposed for the active crevasse splays. As shown in **Figure 36**, the proximal sector of active crevasse splays is above the parent channel with an along-dip convex-up profile more emphasized than in the distal sector.

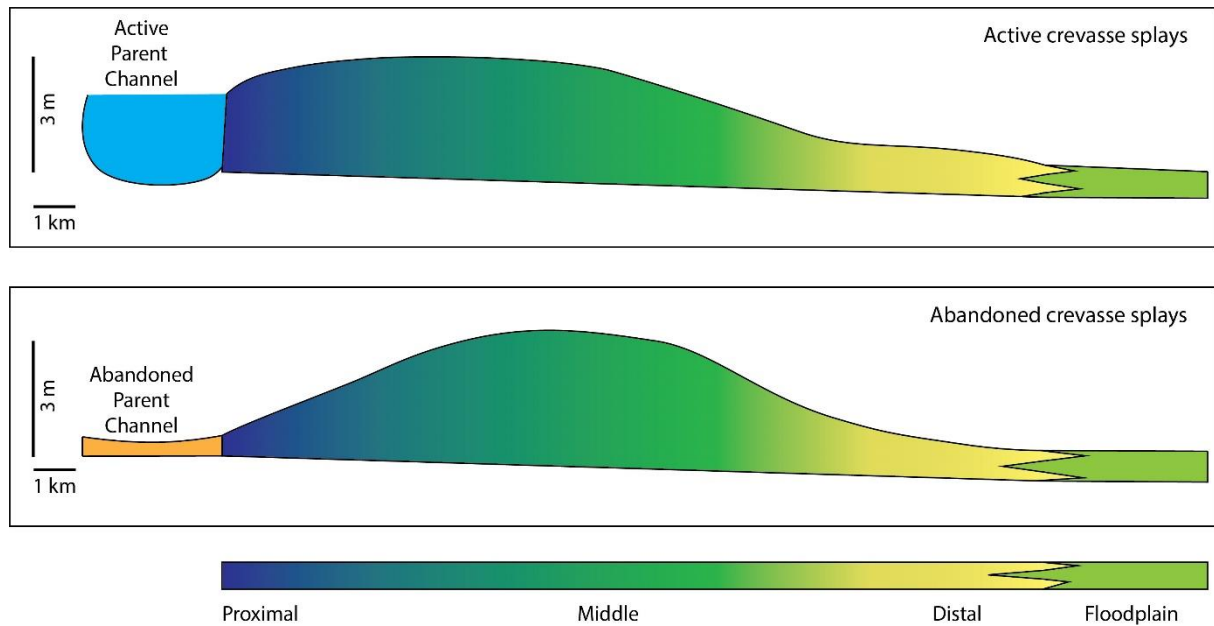


Figure 36 - Along-dip conceptual altimetric profiles of typical active and abandoned crevasse splays as inferred from this research. Crevasse splay section terminology according to Figure 14B.

The stressed convex-up profile suggests the deposition of middle-fine sands, whereas the end of the middle sector and the distal one could be characterized by the finest grain size, although a field check would be required for confirming the real spatial distribution of the deposit that distinguishes a crevasse splay from the floodplain.

Despite the uncertain results obtained for the abandoned crevasse splays, the methodological approach here proposed provided satisfying examples of landforms and deposits due to relict avulsion processes.

In particular, the micro-relief analysis of C2 highlights a convex-up profile disconnected from the parent channel, shifted to the end of the proximal sector up to the beginning of the distal one. Thus, the middle sector is the highest one, revealing an opposite condition to the active crevasse splays (**Figure 36**). Both C2 and C9 still preserve the convex-up profile along-dip direction and only partially along the cross-sections, leading to appreciate a relevant difference between active and abandoned crevasse splays. Indeed, the active crevasse splays are directly connected to their parent channel, while the abandoned crevasse splays seem disconnected (like C2 seems disconnected to the Khalid channel), despite C9 reveals an opposite framework. The SC of abandoned crevasse splays provides inhomogeneous results, suggesting these landforms are subjected to various alterations and the reworking of the deposits. Even if the optical features like the planar fan-shape, the anastomosing pattern of the crevasse channels and the perpendicular development with respect to the river belts are easily detectable on both active and abandoned crevasse splays, the micro-relief analysis and the multispectral analysis improve the discerning between active and abandoned crevasse splays. Especially the micro-relief analysis leads to the recognition of how the typical convex-up profile of the deposit is

modified because of the spatial distribution of single splays, the depth of active crevasse channels, vegetation occurrence, aeolian reworking of abandoned deposits, and human activities.

Results from the SC proved useful for re-mapping the limits of the crevasse deposit and the spatial distribution of the inner distributive channels. In particular, the SC revealed useful for recognizing and properly mapping the active crevasse splays. This approach allowed to evaluate how well the crevasse channels, levees, and deposit are detectable and the suitable classification method for the selected ROIs. Generally, the SC better recognizes the selected ROIs for active crevasse splays, while the abandoned crevasses present a different detail and accuracy.

Finally, among the classification methods adopted, the Maximum Likelihood generally resulted in the best method for recognizing the crevasse channels, levees, and deposits. On the contrary, the SAM method poorly recognized the selected ROIs.

The avulsion processes potentially represent the onset of a new watercourse, especially when the morphodynamics of the drainage pattern are characterized by a multi-channel system. Omitting the different factors involved during the avulsion processes (both human-induced and natural), their recognition is potentially useful for reconstructing the Early Holocene distributary system. Moreover, the avulsion process favoured the irrigation of croplands and the development of the early settlements (Jotheri et al., 2019). Thus, the crevasse splays assume dual importance in the study area, both for the reconstruction of the Holocene multi-channel fluvial system and the geoarchaeological surveys of the numerous ancient settlements. Moreover, at present, a correct and accurate mapping of the active crevasse splays can contribute to better management of the water resource, supporting sustainable agriculture, avoiding water wastage, and limiting the hazard to people and infrastructure (Leenman and Eaton, 2021).

7.2 Geomorphology of the area at Tell Zurghul archaeological site

The methodological approach adopted for the geomorphological reconstruction of Tell Zurghul sample area is essentially based on the visual inspection of the ESRI® TerraColor dataset, the computation of the NDVI and CR indices and the topographic analysis of the micro-relief, since the SC of the abandoned crevasse splays is unsuitable due to their narrow size (i.e., < 50 km²). Comparing two different elevation datasets (AW3D30 and CSK-DEM), the reconstruction of the spatial distribution of the fluvial and anthropic deposits unravels divergent accuracy and feasibility.

The reconstruction of the multi-channel systems of the Shatt al-Gharraf and Dujaila leads to mapping the limit of their floodplains, highlighting that both Lagash and Tell Zurghul have been exclusively influenced by the Tigris river system. Thus, the area can be discerned into the active waterscape of the Shatt al-Gharraf westward, where the man-made canals and fields prevail, and into the relict waterscape of the Dujaila eastward, where the abandoned anastomosing system and crevasse splays are still detectable despite the prevalence of the modern aeolian processes. Indeed, the morphoevolution of the area surrounding the archaeological sites essentially results from a complex interaction between the natural geomorphological processes due to the surficial running waters (channelized and non), and anthropogenic processes, these latter principally connected to the construction of canals for the management of running waters.

Despite the Dujaila Channel is dated to the Sasanian Period (I millennium BC - I millennium AD) as reported by Jotheri (2016), and in spite of the requirement of field checks for confirming the age of the mapped abandoned channels, these latter resemble the framework of a terminal distributary channel system connected to the Tigris paleo-delta. As reported by Olariu and Bhattacharya (2006), terminal distributary channels are frequent in the most distal sector of the river-dominated deltas, and

their dimensions differ between tens of meters to kilometres. The abandoned channels of the eastern sector have mainly an N-S orientation and show either sinuous or anastomosed pattern. Indeed, the terminal distributary channels are often associated with coarse sand levees and scroll-bars, both of which are still recognizable in the area. Thus, it could suppose that the development of the Dujaila during the Sasanian and Islamic periods has been favoured by the previous occurrence of the multi-channel pattern of the terminal distributary system, along which the establishment of the settlements could be complicated by the high lateral mobility of the channels and could be favoured only after the Sasanian and Islamic river channelization (i.e., flood control, straightening, levee construction, etc.).

The before-described assumption about the terminal distributary system can be proved by the archaeological evidence reported by the Italian Archaeological Mission. Indeed, the surveys at Tell Zurghul furnished evidence of the waterscape and the proximity of the Persian Gulf shoreline: the highest Mound A corresponds to the artificial hill occupied by the temple of the goddess Nanshe (i.e., the goddess of the sea and sea species) in the late III millennium BC; in the lower Mound B, fish vertebrae of “Bull Shark” (*Carcharhinus leucas*) is recovered with also other fish vertebrae, sickles to cut reeds in the marshes and fishing net clay weights, dated to Middle Chalcolithic period (early III millennium BC). Thus, Tell Zurghul waterscape developed during the Tigris paleo-delta progradation between 6000 and 4000 yrs BP, where the occurrence of the multi-channel pattern of the terminal distributary system is plausible.

The results obtained by the computation of the multispectral indices NDVI and CR confirm the distinction between the active and modern waterscape of the Shatt al-Gharraf and the relict one of the Dujaila. Indeed, the west sector of Lagash and Tell Zurghul is the most vegetated thanks to the occurrence of several branches from Shatt al-Gharraf, which favour farming activities; instead, the vegetation of the central sector, belonging to the relict waterscape of the Dujaila, presents the peculiar rectangular pattern reflecting the man-made canals spatial distribution, while the easternmost area is essentially barren. The spatial distribution of clay minerals is essentially the same of vegetation, except for the marshland, where the CR is useful for reconstructing its real extension. A similar potential application of the CR, as well as of the NDVI, is the detection of the archaeological sites: both Lagash and Tell Zurghul are free of any vegetation and mainly composed of sand deposits, despite a similar configuration is in the south-west of Tell Zurghul where none archaeological sites have been reported.

For the topographic analysis of the micro-relief, the most recent 1-arcsec DEM (i.e., AW3D30) and the high-resolution CSK-DEM has been compared in order to evaluate the potentiality and applicability of the different elevation datasets. Both the AW3D30 and CSK-DEM profiles have been smoothed through the application of the moving average filter, but for the profiles AA' and BB' (i.e., AW3D30 elevation dataset) the moving average is lower than for the CSK-DEM profiles. Moreover, despite the highest smoothing of the CC' and DD' profiles, the “human-noise” is in any case high, preventing the recognition of the natural and anthropic features alongside the profiles. Thus, the first main difference in the application of these two elevation datasets is the legibility and the easy-recognition of the above-floodplain features alongside the AW3D30 profiles. Indeed, the profiles AA' and BB', after the smoothing, well highlight both the fluvial and the anthropic landforms: the most topographically elevated features are the abandoned channels and the archaeological mounds, while the modern man-made canals and the active channels are less topographically evident. Thus, despite the age of these landforms (i.e., the Holocene) that can suggest a re-working and most likely their destruction, the topographic signature of abandoned channels and mounds is well maintained and well recognizable, while the most recent human canals are substantially less of 1-2 m of height and can be scarcely identified alongside the profiles without the comparison with the results of the visual inspection.

Taking into account the profiles CC' and DD', the topographic evidence of Tell Zurghul is the only one easily recognizable, despite the heights and the steep slope are probably altered by the moving average filter. The main difference with the profiles AA' and BB' is the topography of the floodplain deposits (i.e., the Dujaila ones): the flat surface of the intra-channel floodplain or the marshland deposits is clearly visible alongside the AW3D30 profiles, whereas the same deposits along the CSK-DEM frequently vary their elevation and slope, most likely because of the high vertical accuracy of this DEM (i.e., less of 1 m). Indeed, the "human-noise" due to the occurrence of crops and ploughing prevents the construction of reliable profiles, where the distribution of each deposit can be carried on exclusively through the cross-check with the visual inspection. Anyway, the high vertical accuracy of the CSK-DEM leads to recognizing the double-convexity of the active channels (i.e., profile CC' in **Figure 34**), stressing the two levees on both sides of the channel and the above-floodplain elevation.

Despite the occurrence of "human-noise", the profile CC' reflects a trend already recognized along the profiles AA' and BB': the south-eastward increase of the heights is due both to the presence of the low marshland in the NW sector and to the occurrence of the elevated abandoned system of the terminal distributary channels, proving the good preservation and the poor re-working of the Holocene fluvial landforms.

However, the topographic analysis of the micro-relief and the reconstruction of the deposit distribution focusing on the sample area of Tell Zurghul are better carried out through the elevation data derived from the AW3D30, whereas the CSK-DEM has an excessive vertical accuracy such that the ploughing traces disturb the profiles and provide an intuitive detection of the above-floodplain fluvial landforms and human features. Indeed, the lower vertical accuracy of the AW3D30 leads to smoothing the profiles through a lower moving average filter, quite similar to the moving average applied during the topographic analysis of the avulsion processes (i.e., 20 m), leaving the heights of channels, canals and mounds more reliable. As regarding the potential use of the CSK-DEM for large-scale mapping, it results unsuitable for the study area of Tell Zurghul, where the flat topography decreases the possibility of successful DEM extraction.

The integration of the visual inspection with the multispectral indices NDVI and CR is potentially useful not only for mapping natural and man-made watercourses and discerning the areas with the highest human impact, but also for better defining the limits of specific features like the archaeological sites and the marshland, this latter strongly influenced by the rainfall seasonality. Thus, a multi-sensor approach for a remote sensing investigation is straightforwardly the successful method for recognizing active and relict landforms over a wide flat area, such as the LMP.

8. Conclusions

The waterscape of the LMP shows an incredible variety of fluvial landforms, both active and relict, which reflect the complexity of the Holocene landscape evolution and its morphodynamics. The rapid shift of the Persian Gulf shoreline during the last 10,000 years and the occurrence of the HCC have mainly controlled the fluvial morphodynamic of the Tigris-Euphrates system. Moreover, the favourable environmental conditions led the early human societies to settle along the numerous watercourses of the MP, developing one of the Early River Valley Civilization. Thus, the taming of nature allows the onset of a new form of cultural adaptation such as the peasant farming societies, which replaced the natural ecosystem with the agricultural ones. During the Holocene, the relationship between humans and natural environment shifted from hunting-fishing-gathering groups completely dependent on natural environments to the agro-systems where the natural environmental modifications led to the development of a cultural landscape.

The first irrigation technology was the levee breaks for irrigating the crops through floods and developing flood-based farming. The ongoing levee breaks favoured the occurrence of the fluvial avulsion processes, whose geomorphological and sedimentological evidence are the numerous crevasse splays recognizable along the both active and ancient river channels composing the lowermost sector of the Tigris-Euphrates fluvial system.

The focus on the fluvial avulsion processes leads to answering the first two questions anticipated in the introductory chapter of this thesis: i) the identification of the Lower Mesopotamian fluvial morphodynamic adjustment to the Holocene Climate Changes, and ii) the recognition of the state of activity of the avulsion processes through a complete remote sensing approach, considering a wide study area like the LMP. As concerning the response of the fluvial morphodynamic along the Lower Mesopotamian floodplain, the insufficiency of field-based data and geo-chronological constraints are the main data gap for exhaustively answering to the first question. Anyway, the recognition of several fluvial landforms, both active and relict, is the main evidence of the change in the fluvial morphodynamic and landscape. Despite the incomplete response to the first question, the issue of the remote sensing approach feasibility for recognizing the state of activity of the avulsion processes is fully resolved. Thanks to the integration of the multispectral analysis and the topographic analysis of the micro-relief, the crevasse splays are recognized as the evidence of both alluvial channels and river deltas morphodynamics. Their main framework and physical characteristics can be synthesized as follow:

- The spatial distribution of the crevasse deposit in the active landforms is generally controlled by the occurrence of vegetation, and the latter generally occurs in the proximal sector, favouring the transport of silt and clay up to the distal sector. The vegetation fixes the crevasse levees, favouring the channelized flow mainly in the proximal and middle sectors.
- The maximum convexity of the along-dip altimetric profile shifts from the proximal-middle sectors of the active crevasse splays to the middle sector of the abandoned ones.
- The CR can be used for a change detection analysis of crevasse channels aimed at recognizing which step of a flood event we are observing, and thus for determining the state of activity of a crevasse splay as well as the NDVI.
- The topographic analysis of the microrelief and the multispectral analysis are useful tools for discerning crevasse channels, levees, and deposits, improving their delimitation and mapping, especially for the active landforms.

- Maximum Likelihood proved to be the best classification method, whereas the SAM method proved unsuitable for detecting and mapping the crevasse features in the context of this work.

Finally, the focusing on the archaeological site of Tell Zurghul leads to integrating multidisciplinary data, specifically derived from the survey of the Italian Archaeological Mission and the remote sensing data derived from DEMs (i.e., AW3D30 and CSK-DEM) and Landsat 8 optical-multispectral data. Here, the archaeological evidence of the ancient waterscape surrounding Tell Zurghul and Lagash have been fundamental for defining the geomorphological evidence of a multi-channel system, most likely belonging to the terminal distributary system of the Tigris paleo-delta. As for the remote sensing investigation of the avulsion processes, the multidisciplinary approach for the study area of Tell Zurghul has highlighted these main conclusions:

- The waterscape of the archaeological sites of Tell Zurghul and Lagash was essentially controlled and influenced by the Tigris River, from which a first terminal distributary system developed and successively replaced by the Dujaila Channel.
- The archaeological evidence of fishing and the cult of water goddess dated to ca. 5000 years ago are simultaneous to the delta progradation of the Tigris-Euphrates delta system.
- The computation of NDVI and CR is essential for evaluating the human impact and the probability of abandoned landforms preservation. Indeed, the lowest values of these indices correspond to the less human-influenced area, where the present aeolian processes prevail.
- The topographic analysis of the micro-relief is one more time essential for recognizing the above floodplain framework of the channels and man-made canals. Anyway, increasing the spatial resolution of the DEM is unsuitable for the archaeological area; indeed, several “human noises” affect the elevation data, also after the moving average filter.
- Despite the human disturbance over the CSK-DEM elevation data, the double-convexity of the active channels is clearly shown alongside the profiles. Therefore, the elevation data of AW3D30 is the most suitable for the topographic analysis of the micro-relief, where the above floodplain configuration is easily detectable after a low moving average filter.
- The CSK-DEM shows a north-westward elevation decreasing, not appreciable on AW3D30, highlighting the topographic elevation of the abandoned multi-channel system respect to the topographic depression where the marshes developed.

The results obtained from this thesis can contribute to the evaluation of the risk associated alongside lowland areas to the formation and development of crevasse splays. Indeed, the multi-sensor remote sensing approach is appropriate for investigating extended areas, especially where the population is mainly settled along the rivers. Furthermore, in the specific study area, this work can contribute to the enhancement of knowledge concerning the Holocene waterscape dynamics in relation to the HCC, that favoured the development of the first agricultural techniques and the development of the early human settlements. The methodological approach here proposed can potentially enhance the knowledge about the Holocene human-environmental interactions, which deeply modified the landscape of the LMP.

9. Implications

The sensitivity of a fluvial system is extremely influenced by external disturbance, which can be mainly connected to climate and human activities. These last can easily upset the natural equilibrium of a fluvial system, altering either the entire catchment conditions or the local river channel. In addition to the knowledge about the sensitivity of the fluvial system, the rate of a change and the timescale needed for a complete readjustment are fundamental for successful management of the fluvial environment.

The present study focused on the geomorphological response of the Lower Mesopotamian fluvial system is potentially suitable for the hazard scenarios considered, among others, by the river management, especially for the proposed remote multi-sensor approach. Indeed, aims such as bank protection, flood control, floodplain zonation, pollution and soil erosion are commonly considered in fluvial hazard perspective and can be evaluated also through a remote sensing approach for quickly distinguishing which areas are more or less vulnerable to a specific hazard.

The LMP, as well all other world's greatest floodplains, is potentially appropriate for the examination of past societies' response to environmental changes; indeed, the floodplains are one of the environments where human occupancy and resources are strongly interconnected and the preservation of geoarchaeological records are paramount. Moreover, the considerable widening of the study area, the barrenness especially alongside abandoned fluvial landforms and the availability of several archaeological data provide an unparalleled opportunity for integrating a multidisciplinary approach in order to improve our knowledge about the environmental changes, human impacts and the efficiency of past management solutions.

The view that the past is the key for comprehending the present climate change and predicting its future effects on human society is central for several research programmes like CLIMAP (past climate mapping program of the International Quaternary Association), PAGES (Past Global Changes Project of the International Geosphere-Biosphere Programme) and GLOCOPH (Commission on Global Continental Paleohydrology). All these programmes encourage a multidisciplinary approach for filling the gap that an exclusively geological, biological, or archaeological approach falls into. The geomorphological, remote sensing and archaeological approach discussed in this thesis are one of the several multidisciplinary approaches recently endorsed. Indeed, the recent discoveries on the climate system obtained by satellite remote sensing have passed the insights of climate models and conventional observations, despite the short duration of observation series. The main future challenge is the acquisition of robust long-term trends not only of climate variables, but also of optical and multispectral data through which the change detection applications are useful for geomorphologists in order to reconstruct the landscape morphoevolution. Anyway, the multispectral analysis of the Landsat 8 imagery and the topographic analysis of the micro-relief through different elevation data adopted for the study of the geomorphic response of the Lower Mesopotamian fluvial system would be lacking without both a geomorphological interpretation of fluvial processes and the archaeological surveys for field evidence.

Acknowledgements

Many people who are not directly cited in this dissertation must be thanked. Indeed, behind my name, there is a team that I had the pleasure of working with.

First of all, I do want to thank my supervisor and mentor Prof. Francesco Troiani. His enthusiasm and expertise have been fundamental and invaluable for formulating the research questions and discovering the latest suitable paper for answering to each my question or doubt. His guidance has been essential for remembering me the main aims of this research, adapting them to the new challenge of smart working. His countless feedback pushed me to sharpen my thinking and improve my work every time, remembering that the holidays are essential for breaking your work and relaxing.

Secondly, a great thank goes to Prof. Davide Nadali, who has let me collaborate in a great project, financially supporting my PhD and unveiling how much the water was so relevant for the Early River Valley Civilizations in Near East. We were very disappointed for cancelling the field trip in Southern Mesopotamia because of the occurrence of COVID-19 pandemic and we wish the activities on field will restart as soon as possible.

I would like also to acknowledge Prof. Salvatore Milli, Ph.D. Paolo Mazzanti and Ph.D. Daniela Piacentini, whose expertise in sedimentology, remote sensing and geomorphology have improved the interpretation of results, adding a significant value to this research. A special thanks to NHAZCA team and his CEO Paolo Mazzanti for the logistic support during the elaboration of the COSMO-SkyMed© data. So, a special thank also goes to ASI (Agenzia Spaziale Italiana) for furnishing the COSMO-SkyMed© imagery. Moreover, thanks to Emanuele Mele for helping me with the interferometric analysis.

Some great thanks go to Ph.D. Hans von Suchodoletz and his colleagues of the Institut für Geographie (Leipzig Universität), who have hosted me during my first and second year of my Ph.D., showing me different methodological approach and suggesting new ways for answering to the open question of my research.

Thanks to the reviewers of this thesis: Prof. Domenico Capolongo and Prof. Jorge Pedro Galve Arnedo. Their comments and observations have been helpful for improving this thesis.

Last but not least, thanks to the “Laboratorio di Geografia e Geomorfologia” colleagues, Mario Valiante and Michele Delchiaro, whose company and innumerable discussions about “ArcGIS vs QGIS” have enhanced this experience. A special thanks to the head of the laboratory, Prof. Marta Della Seta, for letting us have a personal desk and create a team with multi-skills.

Appendix

Holocene Climate Changes in the Mediterranean area: an example of traditional, field-based study in the northern Apennines

This section has been presented during the Physich-geographisches Forschungskolloquium Leipzig SoSe 2019 - 19.06.2019, Institut für Geographie, Universität Leipzig. *Geomorphic response to Holocene climate changes: Insights from the Cesano River valley, northern Apennines of Italy* - Giulia Iacobucci.

The mid sector of the Cesano River valley is located in the foothills of the northern Marche Apennines. The Umbro-Marchean Apennines form an NW-SE thrust-and-fold belt, developed from the Early Miocene because of the collision between the Eurasian and African Plates (Mayer et al., 2003; Troiani and Della Seta, 2011). Since the Middle-Upper Pliocene, the tectonic uplift of the Adriatic side of the Apennines occurred and increased at the end of the Lower Pleistocene, carrying on during the Holocene with a rate of 0.3-0.5 mm/yr in the inner sector and decreasing eastward towards the coastal area (Troiani and Della Seta, 2008; Calderoni et al., 2010; Troiani and Della Seta, 2011; Nesci et al., 2012).

The transversal drainage network of this sector, with the sub-parallel arrangement of the main valleys, developed from the Upper Pliocene-Lower Pleistocene, whose southwest-northeast orientation is mainly controlled by the persistent tectonic uplift which favoured the river entrenchment, river terrace formation, headward erosion and stream captures (Mayer et al., 2003; Troiani and Della Seta, 2011; Nesci et al., 2012). In addition to the regional uplift, the sea-level oscillation during Middle and Late Pleistocene times played a key role in the fluvial morphodynamic, especially in the middle and low sector of the Marchean rivers. In particular, the Last Glacial Maximum sea level drop caused the north Adriatic continental shelf emersion, the doubling of the major rivers length and the increase of the river incision, largely in the mouth sectors. During the lowstand at the glacial stages, the cold-climate driven aggradation prevailed, successively interrupted by the fluvial erosion during the inter-glacials, forming a well-preserved staircase of fluvial terraces (Troiani and Della Seta, 2008; Calderoni et al., 2010; Troiani and Della Seta, 2011).

One of the first classifications of the Umbro-Marchean fluvial terraces proposed by Selli (1954) recognized four main orders of fill terraces (T1-T4 from the Middle Pleistocene to the Holocene); anyway, further following surveys also considered and described the oldest and higher strath terraces and, in particular, highlighted the complexity of the Holocene fluvial succession which is characterized by typical fluvial cut-and-fill episodes (Calderoni et al., 2010; Nesci et al., 2012).

The four main guide stages of the fill terraces involve the complex climatically-driven aggradation and incision episodes that characterize each stage. The complete succession is introduced mainly for the Metauro and Foglia basins (i.e., T1a, T1b, T2 and T3), while for the Cesano River the first level T1 is not distinguished into the sub-levels a and b (Troiani and Della Seta, 2011). Each cycle starts with an erosional phase, during which the river cuts the former alluvial fills, deepening the valley floor up to the bedrock; the meandering pattern typically reflects the interglacial conditions of sediment load and discharge. The deterioration of climatic conditions shifts the geomorphic thresholds into a braided pattern. Indeed, the decrease of the vegetation cover increases the hillslope runoff and the sediment budget exceeds the stream power (i.e., the sediment transport capacity of the river determined by discharge and slope). Thus, this first aggradation phase fills the formerly incised valley with gravels and sands until the peak of the glacial stage. Indeed, after the first response of the fluvial systems, the

second aggradation phase is driven by the climatic response of the hillslope sector with the formation of alluvial fans at the junction tributary-main trunk and piedmont aprons (Nesci et al., 2012).

However, the aforementioned guide stages are not enough detailed for describing the HCC, here represented by minor depositional-erosional episodes preserved into the cut-and-fill sequences of the Holocene terraced alluvium. Nesci et al. (2012) proposed an idealized cross section for summarizing all the main post-glacial deposits that characterize the intermediate valley sector of the Marchean Apennines and for describing their complex framework (**Figure 37**).

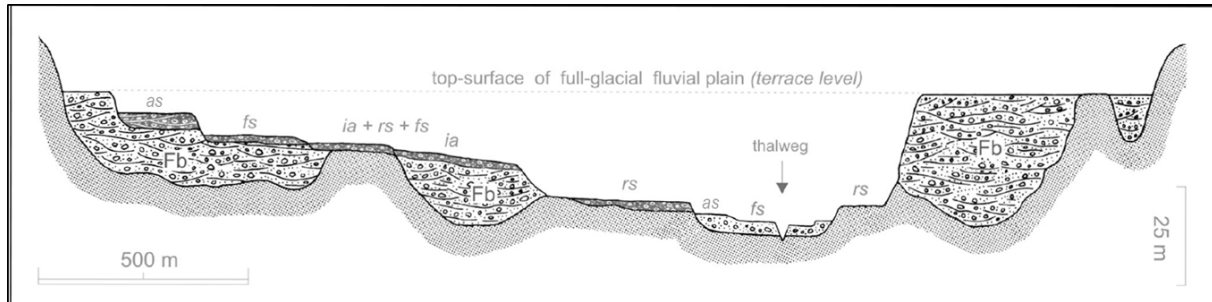


Figure 37 - The idealised transversal cross section of the intermediate valley sector in a hypothetical northern Marche river. The deposits are coded as as=minor fill terraces, fs=in-growing meandering, ia=inclined alluvial sheets, rs=rock-cut strath terraces, Fb=aggradation of braided facies in full-glacial condition (from Nesci et al., 2012).

The complexity and variety of the post-glacial fluvial deposits offer an appropriate case study for a detailed reconstruction of the Cesano River morphodynamics during the Holocene and for understanding the response of a fluvial system within the Mediterranean basin to the climate change during the Holocene and historical times. Besides the Holocene has been characterized by a general post-T3 downcutting, its partial re-incision and recurrent episodes of alluvial fillings become progressively more important coastward. Moreover, the hilly sector of the Cesano River, between the towns of San Lorenzo in Campo and San Michele al Fiume, has been so far considered one of the most suitable area where the relationship between human frequentation and fluvial system dynamics can be unravelled, due to the presence of the remnants of the ancient Roman town of Suasa (III century BC).

The San Michele al Fiume area is precious because of the availability of three cores, where a preliminary recognition of the Holocene fluvial facies can be carried on (**Figure 38**) (Dall'Aglio et al., 2012). The cores s2 and s3 are proximal to Rio Freddo, a tributary of the Cesano trunk stream, while the core s1 is on the right bank of the Cesano main stream reaching, the latter, about 10 m of depth. The deepest core s1 shows the uppermost portion of the T3 deposits, which is dated ($32,500 \pm 1200$ ^{14}C or $37,185 \pm 1586$ cal BP obtained through <http://www.calpal-online.de/>). The Pleistocene braided deposit underlies below a younger braided deposit dated to Late Holocene ($\approx 1530 \pm 40$ ^{14}C or 1437 ± 58 cal BP). The core s2 is the shallowest one, where only the Holocene fluvial deposits are reported; the deepest one is a sandy facies ascribed to a meandering river pattern, whose dating (4250 ± 75 - 4550 ± 75 ^{14}C or 4776 ± 114 cal BP) cannot be considered somewhat "puzzling" because of the reworking of the dating sample. The upper deposit is Late Holocene braided facies showing a sandy gravel deposit. Finally, the core s3 preserves the same facies of core s2, but the sandy one is correctly dated to Late Holocene (2970 ± 70 ^{14}C or 3147 ± 108 cal BP).

In spite of the availability of just three cores, the proposed outlined cross section in **Figure 38** is supposed for comparing the hypothetical framework of the San Michele al Fiume deposits to the idealised cross section proposed by Nesci et al. (2012).

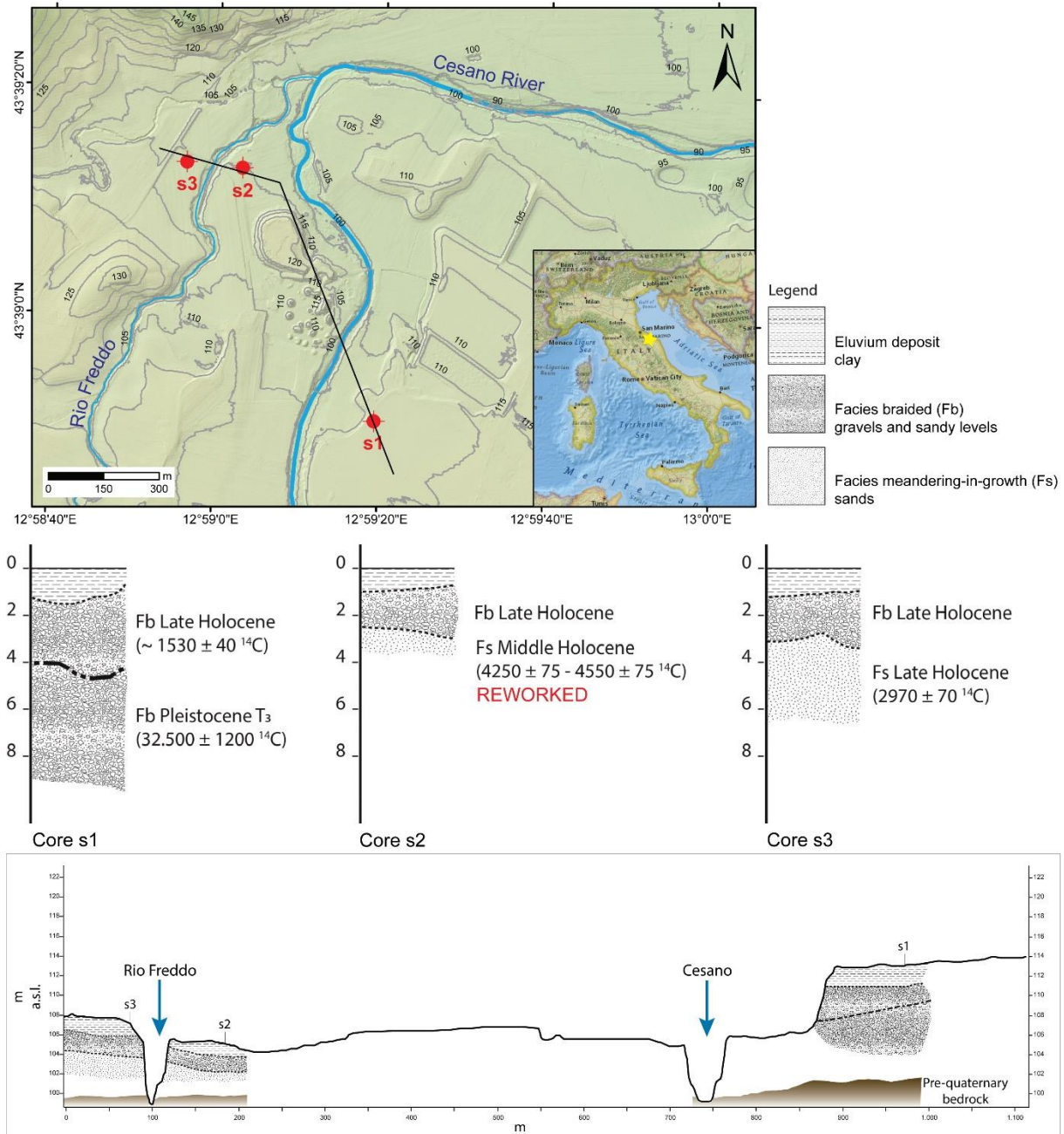


Figure 38 - The San Michele al Fiume area where the cores described and dated by Dall'Aglio et al. (2012) have been drilled and the cross section transversal to the trunk valley.

The Pleistocene braided deposit of T₃ is preserved just in core s1 on the right bank of the Cesano, most likely making up the highest sector of the right bank. Conversely, both the cores near Rio Freddo preserve Holocene facies, most likely linked to the cut-and-fill sequences, where the influence of the human impact can be supposed. The shift from a meandering pattern to a braided one during the Late Holocene (i.e., cores s2 and s3) is most likely due to the abandonment of Suasa, when the civil wars during the decline of the Roman Emperor induced the population to leave small towns and the countryside, abandoning the management of drainage system. Anyway, it cannot be excluded that the facies variations can be related to known Holocene climate variations, for example the one at the mid Holocene characterized by arid conditions shifting (i.e., the 4.2 ka Bond Event).

The sedimentary structure is appreciable along an extending outcrop near the fossil forest of Valcesano (about 5 km north-east of San Michele al Fiume), that shows the festoon-like cross

stratification of braided deposits and the epsilon stratification of meandering deposits, typically associated with point bars (**Figure 39**).

This case study is a good example of traditional, field-based analysis of river systems for understanding the relations existing between Holocene climate and river morphodynamics. Nonetheless, this classical study shows some limits due to the difficulties on appreciating the river system response to climate change just basing only a field dataset and, in the specific case study, to unravel and distinguish the river system response to human activities and climate variations. Indeed, the reworking of the dated samples and the sporadic occurrence of well-exposed outcrops like the Valcesano's one are the most common restrictions of the field-based analysis.

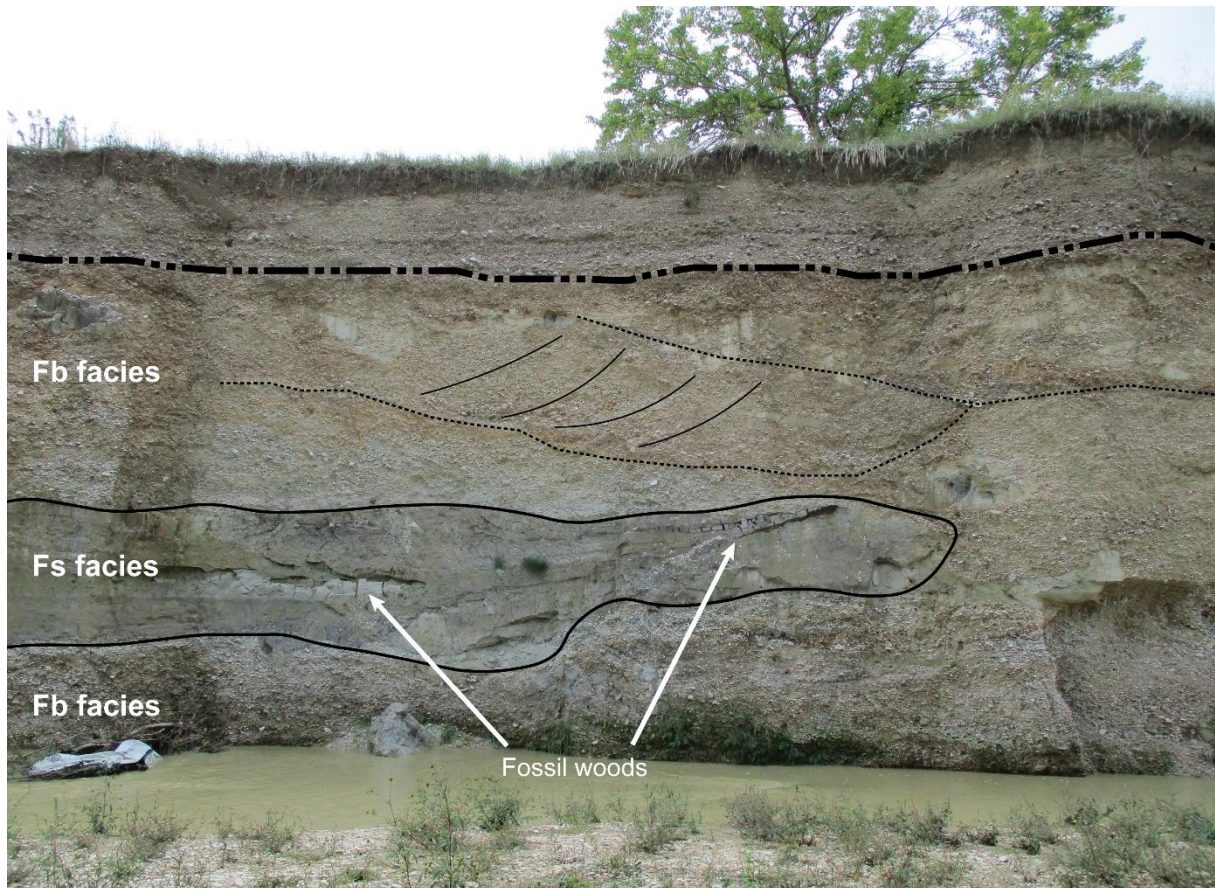


Figure 39 - The outcrop of the fossil forest of Valcesano where the stratigraphic structures of the Fb and Fs facies are appreciable.

References

- About ALOS – AVNIR-2. Available online: <https://www.eorc.jaxa.jp/ALOS/en/about/avnir2.htm> (accessed on 05 August 2020)
- About ALOS - Overview and Objectives. Available online: https://www.eorc.jaxa.jp/ALOS/en/about/about_index.htm (accessed on 20 July 2020)
- ADEOS. eoPortal Directory. Available online: <https://earth.esa.int/web/eoportal/satellite-missions/a/adeos> (accessed on 05 August 2020)
- Al-Ameri, I.D.S.; Briant, R.M. A late Holocene molluscan-based palaeoenvironmental reconstruction from southern Mesopotamia: Implications for the palaeogeographic evolution of the Arabo-Persian Gulf. *Journal of African Earth Sciences*. **2019**, *152*, 1-9. [doi:10.1016/j.jafrearsci.2018.12.012]
- Allen, J.R.L. A review of the origin and characteristics of recent alluvial sediments. *Sedimentology*. **1965**, *5(2)*, 87-191. [doi:10.1111/j.1365-3091.1965.tb01561.x]
- ALOS. eoPortal Directory. Available online: <https://earth.esa.int/web/eoportal/satellite-missions/a/alos> (accessed on 20 July 2020)
- Altinbilek, D. Development and management of the Euphrates–Tigris basin. *International Journal of Water Resources Development*. **2004**, *20(1)*, 15-33. [doi:10.1080/07900620310001635584]
- Anderson, D.G.; Maasch, K.A.; Sandweiss, D.H.; Mayewski, P.A. Climate and culture change: exploring Holocene transitions. In *Climate change and cultural dynamics. A Global Perspective on Mid-Holocene Transitions*, 1st ed.; Anderson, D.G., Maasch, K.A., Sandweiss, D.H., Eds.; Elsevier: London, UK, 2007; pp. 1-23
- Andrews, J.E.; Carolin, S.A.; Peckover, E.N.; Marca, A.; Al-Omari, S.; Rowe, P.J. Holocene stable isotope record of insolation and rapid climate change in a stalagmite from the Zagros of Iran. *Quaternary Science Reviews*. **2020**, *241*, 106433. [doi:10.1016/j.quascirev.2020.106433]
- Aqrabi, A.A.M. Correction of Holocene sedimentation rates for mechanical compaction: The Tigris Euphrates Delta, Lower Mesopotamia. *Marine and Petroleum Geology*. **1995**, *12(4)*, 409-416. [doi:10.1016/0264-8172(95)96903-4]
- Aqrabi, A.A.M. Stratigraphic signatures of climatic change during the Holocene evolution of the Tigris–Euphrates delta, lower Mesopotamia. *Global and Planetary Change*. **2001**, *28*, 267-283. [doi:10.1016/S0921-8181(00)00078-3]
- Aqrabi, A.A.M.; Domas, J.; Jassim, S.Z. Quaternary deposits. In *Geology of Iraq*. Jassim, S.Z., Goff, J.C., Eds.; Dolin Press: Prague and Moravian Museum, Brno, Czech Republic, 2006; pp. 185-198
- Aslan, A. Fluvial Environments. In *Encyclopedia of Quaternary Science*; Elias, S.A., Ed.; Elsevier: Amsterdam, The Netherlands, 2006; Volume 1, pp. 672-685
- Banko, G. *A Review of Assessing the Accuracy of Classifications of Remotely Sensed Data and of Methods Including Remote Sensing Data in Forest Inventory*; Interim Report IR-98-081; University of Agricultural Sciences: Wien, Austria, 1998.
- Bar-Matthews, M.; Ayalon, A. Mid-Holocene climate variations revealed by high-resolution speleothem records from Soreq Cave, Israel and their correlation with cultural changes. *The Holocene*. **2011**, *21(1)*, 163-171. [doi:10.1177/0959683610384165]
- Bar-Matthews, M.; Ayalon, A.; Kaufman, A.; Wasserburg, G.J. The Eastern Mediterranean paleoclimate as a reflection of regional events: Soreq cave, Israel. *Earth and Planetary Science Letters*. **1999**, *166(1-2)*, 85-95. [doi:10.1016/S0012-821X(98)00275-1]

- Benjamin, J.; Rovere, A.; Fontana, A.; Furlani, S.; Vacchi, M.; Inglis, R.H.; Galili, E.; Antonioli, F.; Sivan, D.; Miko, S.; et al. Late Quaternary sea-level changes and early human societies in the central and eastern Mediterranean Basin: An interdisciplinary review. *Quaternary International*. **2017**, *449*, 29-57. [doi:10.1016/j.quaint.2017.06.025]
- Bernal, C.; Christophoul, F.; Darrozes, J.; Laraque, A.; Bourrel, L.; Soula, J.C.; Guyot, J.L.; Baby, P. Crevasse and capture by floodplain drains as a cause of partial avulsion and anastomosis (lower Rio Pastaza, Peru). *Journal of South America Earth Sciences*. **2013**, *44*, 63–74. [doi:10.1016/j.jsames.2012.11.009]
- Bertlein, P.J. The Scales of Climate Change. In *Encyclopedia of Quaternary Science*; Elias, S.A., Ed.; Elsevier: Amsterdam, The Netherlands, 2006; Volume 1, pp. 1873-1883
- Bini, M.; Zanchetta, G.; Persoiu, A.; Cartier, R.; Català, A.; Cacho, I.; Dean, J.R.; Di Rita, F.; Drysdale, R.N.; Finnè, M.; et al. The 4.2 kaBP Event in the Mediterranean region: an overview. *Climate of the Past*. **2019**, *15*, 555-577. [doi:10.5194/cp-15-555-2019]
- Björck, S.; Walker, M.J.C.; Cwynar, L.C.; Johnson, S.J.; Knudsen, K.L.; Lowe, J.J.; Wohlfarth, B.; and INTIMATE Members. An event stratigraphy for the Last Termination in the North Atlantic region based on the Greenland ice-core record: a proposal by the INTIMATE group. *Journal of Quaternary Science*. **1998**, *13*, 283–292. [doi:10.1002/(SICI)1099-1417(199807/08)13:4<283::AID-JQS386>3.0.CO;2-A]
- Blanco-González, A.; Lillios, K.T.; López-Sàez, J.A.; Drake, B.L. Cultural, Demographic and Environmental Dynamics of the Copper and Early Bronze Age in Iberia (3300–1500 BC): Towards an Interregional Multiproxy Comparison at the Time of the 4.2 ky BP Event. *Journal of World Prehistory*. **2018**, *31*, 1-79. [doi:10.1007/s10963-018-9113-3]
- Blum, M.; Törnqvist, T.E. Fluvial responses to climate and sea-level change: a review and look forward. *Sedimentology*. **2000**, *47*(1), 2-48. [doi:10.1046/j.1365-3091.2000.00008.x]
- Blum, M.D. Glacial-Interglacial scale fluvial responses. In *Encyclopedia of Quaternary Science*; Elias, S.A., Ed.; Elsevier: Amsterdam, The Netherlands, 2006; Volume 1, pp. 686-694
- Bogemans, F.; Boudin, M.; Janssens, R.; Baeteman, C. New data on the sedimentary processes and timing of the initial inundation of Lower Khuzestan (SW Iran) by the Persian Gulf. *The Holocene*. **2017**, *27*(4), 613-620. [doi:10.1177/0959683616670224]
- Bogemans, F.; Janssens, R.; Baeteman, C. Depositional evolution of the Lower Khuzestan plain (SW Iran) since the end of the Late Pleistocene. *Quaternary Science Reviews*. **2017**, *171*, 154-165. [doi:10.1016/j.quascirev.2017.07.011]
- Bolikhovskaya, N.S.; Porotov, A.V.; Richards, K.; Kaitamba, M.D.; Faustov, S.S.; Korotaev, V.N. Detailed reconstructions of Holocene climate and environmental changes in the Taman Peninsula (Kuban River delta region) and their correlation with rapid sea-level fluctuations of the Black Sea. *Quaternary International*. **2018**, *465*, 22-36. [doi:10.1016/j.quaint.2017.08.013]
- Bond, G.; Kromer, B.; Beer, J.; Muscheler, R.; Evans, M.N.; Showers, W.; Hoffmann, S.; Lotti-Bond, R.; Hajdas, I.; Bonani, G. Persistent Solar Influence on North Atlantic Climate During the Holocene. *Science*. **2001**, *294*(5549), 2130-2136. [doi:10.1126/science.1065680]
- Bond, G.; Showers, W.; Cheseby, M.; Lotti, R.; Almasi, P.; deMenocal, P. A pervasive millennial-scale cycle in North Atlantic Holocene and glacial climates. *Science*. **1997**, *278*(5341), 1257-1266. [doi:10.1126/science.278.5341.1257]
- Bozkurt, D.; Sen, O.L. Climate change impacts in the Euphrates–Tigris Basin based on different model and scenario simulations. *Journal of Hydrology*. **2013**, *480*, 149-161. [doi:10.1016/j.jhydrol.2012.12.021]

- Braun, A. DEM generation with Sentinel-1 Workflow and challenges. Available online: <http://step.esa.int/docs/tutorials/S1TBX%20DEM%20generation%20with%20Sentinel-1%20IW%20Tutorial.pdf> (accessed on 17 June 2020)
- Braun, A. Sentinel-1 Toolbox: DEM generation with Sentinel-1. Available online: <http://step.esa.int/docs/tutorials/S1TBX%20DEM%20generation%20with%20Sentinel-1%20IW%20Tutorial.pdf> (accessed on 22 August 2020)
- Bridge, J.; Demicco, R. *Earth Surface Processes, Landforms, and Sediment Deposits*. Cambridge University Press: New York, 2008
- Bridge, J.S. *Rivers and Floodplains: Forms, Processes, and Sedimentary Record*. Blackwells: Oxford, 2003.
- Bridge, J.S.; Leeder, M.R. A simulation model of alluvial stratigraphy. *Sedimentology*. **1979**, *26*, 617–644. [doi:10.1111/j.1365-3091.1979.tb00935.x]
- Bridgland, D.R.; Bennett, J.A.; McVicar-Wright, S.E.; Scrivener, R.C. Rivers through geological time: the fluvial contribution to understanding of our planet. *Proceedings of the Geologists' Association*. **2014**, *125*, 503-510. [doi:10.1016/j.pgeola.2014.11.001]
- Bridgland, D.R.; Westaway, R. Quaternary fluvial archives and landscape evolution: a global synthesis. *Proceedings of the Geologists' Association*. **2014**, *125*, 600-629. [doi:10.1016/j.pgeola.2014.10.009]
- Bristow, C.; Skelly, R.; Ethridge, F. Crevasse splays from the rapidly aggrading, sand-bed, Niobrara River, Nebraska: effect of base-level rise. *Sedimentology*. **1999**, *46*, 1029-1048. [doi:10.1046/j.1365-3091.1999.00263.x]
- Brown, A.G. *Alluvial geoarchaeology: Floodplain archaeology and environmental change*, 1st ed.; Cambridge University Press: Cambridge, UK, 1997
- Buehler, H.A.; Weissmann, G.S.; Scuderi, L.A.; Hartley, A.J. Spatial and temporal evolution of an avulsion on the Taquari River distributive fluvial system from satellite image analysis. *Journal of Sedimentary Research*. **2011**, *81*, 630–640. [doi:10.2110/jsr.2011.040]
- Bull, W.B. *Geomorphic Responses to Climatic Change*; Oxford University Press: New York, NY, USA, 1991; ISBN 978-1932846218
- Burns, C.; Mountney, N.P.; Hodgson, D.M.; Colombera, L. Anatomy and dimensions of fluvial crevasse-splay deposits: Examples from the Cretaceous Castlegate Sandstone and Neslen Formation, Utah, USA. *Sedimentary Geology*. **2017**, *351*, 21–35. [doi:10.1016/j.sedgeo.2017.02.003]
- Butzer, K.W. Collapse, environment, and society. *Proceedings of the National Academy of Sciences of the United States of America*. **2012**, *109*(10), 3632-3639. [doi:10.1073/pnas.1114845109]
- Calderoni, G.; Della Seta, M.; Fredi, P.; Palmieri, E.L.; Nesci, O.; Savelli, D.; Troiani, F. Late Quaternary geomorphological evolution of the Adriatic coast reach encompassing the Metauro, Cesano and Misa river mouths (Northern Marche, Italy). *Geology of the Adriatic Sea*. **2010**, *3*, 109-124.
- Capaldo, P. High resolution radargrammetry with COSMO-SkyMed©, TerraSAR-X and RADARSAT-2 imagery: development and implementation of an image orientation model for Digital Surface Model generation. Ph.D. Thesis, Sapienza Università di Roma, Roma, Italia, April 2013
- Carrasco, D.; Díaz, J.; Broquetas, A.; Arbiol, R.; Castillo, M.; Palà, V. Ascending-descending orbit combination SAR interferometry assessment. Available online: <https://earth.esa.int/workshops/ers97/papers/carrasco/index-2.html> (accessed on 20 July 2020)
- Chauhan, P.R.; Bridgland, D.R.; Moncel, M.H.; Antoine, P.; Bahain, J.J.; Briant, R.; Cunha, P.P.; Despriée, J.; Limondin-Lozouet, N.; Locht, J.L.; et al. Fluvial deposits as an archive of early human activity: Progress during the 20 years of the Fluvial Archives Group. *Quaternary Science Reviews*. **2017**, *166*, 114-149. [doi:10.1016/j.quascirev.2017.03.016]

Cologne Radiocarbon Calibration & Paleoclimate Research Package. Available online: <http://www.calpal-online.de/> (accessed on 15 July 2019)

Corenblit, D.; Vautier, F.; González, E.; Steiger, J. Formation and dynamics of vegetated fluvial landforms follow the biogeomorphological succession model in a channelized river. *Earth Surface Processes and Landforms*. **2020**, *45*, 2020-2035. [doi:10.1002/esp.4863]

Cullen, H.M.; deMenocal, P.B. North Atlantic Influence on Tigris–Euphrates streamflow. *International Journal of Climatology*. **2000**, *20*, 853-863. [doi:10.1002/1097-0088(20000630)20:8<853::AID-JOC497>3.0.CO;2-M]

Cullen, H.M.; Kaplan, A.; Arkin, P.A.; deMenocal, P.B. Impacts of the North Atlantic Oscillation on Middle Eastern climate and streamflow. *Climate Change*. **2002**, *55*, 315-338. [doi:10.1023/A:1020518305517]

D’Alpoim Guedes, J.; Manning, S.W.; Bocinsky, R.K. A 5,500-Year Model of Changing Crop Niches on the Tibetan Plateau. *Current Anthropology*. **2016**, *57*(4), 517-522. [doi:10.1086/687255]

D’Arcy, M.; Mason, P.J.; Roda-Boluda, D.C.; Whittaker, A.C.; Lewis, J.M.T.; Najorka, J. Alluvial fan surface ages recorded by Landsat-8 imagery in Owens Valley, California. *Remote Sensing of Environment*. **2018**, *216*, 401–414. [doi:10.1016/j.rse.2018.07.013]

Dall’Aglio, P.L.; Giorgi, E.; Silani, M.; Aldrovandi, M.; Franceschelli, C.; Nesci, O.; Savelli, D.; Troiani, F.; Pellegrini, L.; Zizioli, D. Ancient landscape changes in the North Marche region: an archaeological and geomorphological appraisal in the Cesano valley. In Proceedings of the XXXII rencontres internationales d’archéologie et d’histoire d’Antibes, 2012, pp. 101-112

Davis, M.E.; Thompson, L.G. An Andean ice-core record of a Middle Holocene mega-drought in North Africa and Asia. *Annals of Glaciology*. **2006**, *43*, 34-41. [doi:10.3189/172756406781812456]

Dawson, H.F. Water flow and the vegetation of running waters. In *Vegetation of Inland Waters*, 1st ed.; Symoens, J.J., Ed.; Kluwer Academic Publishers: Dordrecht, The Netherlands, 1988; Volume 15-1, pp. 283–309

Denton, G.H.; Karlén, W. Holocene climatic variations - Their pattern and possible cause. *Quaternary Research*. **1973**, *3*(2), 155-174. [doi:10.1016/0033-5894(73)90040-9]

Di Rita, F.; Magri, D. Holocene drought, deforestation and evergreen vegetation development in the central Mediterranean: a 5500 year record from Lago Alimini Piccolo, Apulia, southeast Italy. *The Holocene*. **2009**, *19*(2), 295-306. [doi:10.1177/0959683608100574]

El Bastawesy, M.; Gebremichael, E.; Sultan, M.; Attwa, M., Sahour, H. Tracing Holocene channels and landforms of the Nile Delta through integration of early elevation, geophysical, and sediment core data. *The Holocene*. **2020**, *30*(8), 1129-1141. [doi:10.1177/0959683620913928]

Emiliani, C. Paleotemperature Analysis of Caribbean Cores P6304-8 and P6304-9 and a Generalized Temperature Curve for the past 425,000 Years. *The Journal of Geology*. **1966**, *74*(2), 109-124. [doi:10.1086/627150]

Engel, M.; Brückner, H. Holocene climate variability of Mesopotamia and its impact on the history of civilisation. *EarthArXiv* **2018**. [doi:10.31223/osf.io/s2aqt]

Engel, M.; Brückner, H.; Pint, A.; Wellbrock, K.; Ginau, A.; Voss, P.; Grottker, M.; Klasen, N.; Frenzel, P. The early Holocene humid period in NW Saudi Arabia – evidence from sediments, microfossils and palaeo-hydrological modelling. *Quaternary International*. **2012**, *266*, 131-141. [doi:10.1016/j.quaint.2011.04.028]

Enzel, Y.; Kushnir, Y.; Quade, J. The middle Holocene climatic records from Arabia: Reassessing lacustrine environments, shift of ITCZ in Arabian Sea, and impacts of the southwest Indian and African monsoons. *Global and Planetary Change*. **2015**, *129*, 69-91. [doi:10.1016/j.gloplacha.2015.03.004]

Epstein, S.; Mayeda, T. Variation of O¹⁸ content of waters from natural sources. *Geochimica et Cosmochimica Acta*. **1953**, *4*(5), 213-224. [doi:10.1016/0016-7037(53)90051-9]

- Evans, G. An historical review of the Quaternary sedimentology of the Gulf (Arabian/Persian Gulf) and its geological impact. In *Quaternary Carbonate and Evaporite Sedimentary Facies and Their Ancient Analogues: A Tribute to D.J. Sherman*. Kendall, C.G.S, Alsharhan, A. Eds. Wiley-Blackweel: Chichester, UK: pp. 11-44
- Faust, D.; Zielhofer, C.; Escudero R.B.; del Olmo, F.D. High-resolution fluvial record of late Holocene geomorphic change in northern Tunisia: climatic or human impact? *Quaternary Science Reviews*. **2004**, *23*, 1757-1775. [doi:10.1016/j.quascirev.2004.02.007]
- Fiorentino, C.; Virelli, M.; Battagliere, M.L. *COSMO-SkyMed© Mission and Products Description*; Doc. N° ASI-CSM-PMG-NT-001; Italian Space Agency, 2019
- Fisher, D.; Osterberg, E.; Dyke, A.; Dahl-Jensen, D.; Demuth, M.; Zdanowicz, C.; Bourgeois, J.; Koerner, R.M.; Mayewski, P.; Wake, C.; et al. The Mt Logan Holocene - late Wisconsinan isotope record: tropical Pacific - Yukon connections. *The Holocene*. **2008**, *18(5)*, 667-677. [doi:10.1177/0959683608092236]
- Fouad, S.F. Tectonic and structural evolution of the Mesopotamia Foredeep. *Iraqi Bulletin of Geology and Mining*. **2010**, *6(2)*, 41-53.
- Garzanti, E.; Al-Juboury, A.I.; Zoleikhaei, Y.; Vermeesch, P.; Jotheri, J.; Akkoca, D.B.; Obaid, A.K.; Allen, M.B.; Andò, S.; Limonta, M.; et al. The Euphrates-Tigris-Karun river system: Provenance, recycling and dispersal of quartz-poor foreland-basin sediments in arid climate. *Earth-Science Reviews*. **2016**, *162*, 107-128. [doi:10.1016/j.earscirev.2016.09.009]
- Gaugnin, M.; Jennings, R.; Eager, H.; Parton, A.; Stimpson, C.; Stepanek, C.; Pfeiffer, M.; Groucutt, H.S.; Drake, N.A.; Alsharekh, A. et al. Rock art imagery as a proxy for Holocene environmental change: A view from Shuwaymis, NW Saudi Arabia. *The Holocene*. **2016**, *26(11)*, 1822-1834. [doi:10.1177/0959683616645949]
- Gillespie, A.R. Spectral mixture analysis of multispectral thermal infrared images. *Remote Sensing of Environmental*. **1992**, *42*, 137-145. [doi:10.1016/0034-4257(92)90097-4]
- Giosan, L.; Clift, P.D.; Macklin, M.G.; Fuller, D.Q.; Constantinescu, S.; Durcan, J.A.; Stevens, T.; Duller, G.A.T.; Tabrez, A.R.; Gangal, K.; et al. Fluvial landscapes of the Harappan civilization. *Proceedings of the National Academy of Sciences of the United States of America*. **2012**, *109(26)*, E1688-E1694. [doi:10.1073/pnas.1112743109]
- Goldstein, S.L.; Hemming, S.R. Long-lived Isotopic Tracers in Oceanography, Paleoceanography, and Ice-sheet Dynamics. In *Treatise on Geochemistry*. Holland, H.D., Turekian, K.K., Eds.; Elsevier: Amsterdam, The Netherlands, 2003; Volume 6, pp. 453-489
- González-Sampériz, P.; Utrilla, P.; Mazo, C.; Valero-Garcés, B.; Sopena, M.C.; Morellón, M.; Sebastià, M.; Moreno, A.; Martínez-Bea, M. Patterns of human occupation during the early Holocene in the Central Ebro Basin (NE Spain) in response to the 8.2 ka climatic event. *Quaternary Research*. **2009**, *71(2)*, 121-132. [doi:10.1016/j.yqres.2008.10.006]
- Goudie, A.S. *Encyclopedia of Geomorphology*, 1st ed.; Routledge: London, UK, 2004; pp. 19-21, 381-384
- Gulliford, A.R.; Flint, S.S.; Hodgson, D.M. Crevasse splay processes and deposits in an ancient distributive fluvial system: The lower Beaufort Group, South Africa. *Sedimentary Geology*. **2017**, *358*, 1-18. [doi:10.1016/j.sedgeo.2017.06.005]
- Guo, L.; Xiong, S.; Ding, Z.; Jin, G.; Wu, J.; Ye, W. Role of the mid-Holocene environmental transition in the decline of late Neolithic cultures in the deserts of NE China. *Quaternary Science Reviews*. **2018**, *190*, 98-113. [doi:10.1016/j.quascirev.2018.04.017]
- Hajek, E.A.; Wolinsky, M.A. Simplified process modelling of river avulsion and alluvial architecture: connecting models and field data. *Sedimentary Geology*. **2012**, *257-260*, 1-30. [doi:10.1016/j.sedgeo.2011.09.005]
- Heinrich, H. Origin and consequences of cyclic ice rafting in the Northeast Atlantic Ocean during the past 130,000 years. *Quaternary Research*. **1988**, *29(2)*, 142-152. [doi:10.1016/0033-5894(88)90057-9]

- Heyvaert, V.M.A.; Walstra, J. The role of long-term human impact on avulsion and fan development. *Earth Surface Processes and Landforms*. **2016**, *41*, 2137–2152. [doi:10.1002/esp.4011]
- Hiatt, M.; Passalacqua, P. What controls the transition from confined to unconfined flow? Analysis of hydraulics in a coastal river delta. *Journal of Hydraulic Engineering*. **2017**, *143*(6). [doi:10.1061/(ASCE)HY.1943-7900.0001309]
- Holmgren, K., Gogou, A.; Izdebski, A.; Luterbacher, J.; Sicre, M.A.; Xoplaki, E. Mediterranean Holocene climate, environment and human societies. *Quaternary Science Reviews*. **2016**, *136*, 1-4. [doi:10.1016/j.quascirev.2015.12.014]
- Hritz, C.; Wilkinson, T. Using Shuttle Radar Topography to map ancient water channels in Mesopotamia. *Antiquity*. **2006**, *80*(308), 415-424. [doi:10.1017/S0003598X00093728]
- Huang, C.C.; Pang, J.; Zha, X.; Su, H.; Jia, Y. Extraordinary floods related to the climatic event at 4200 a BP on the Qishuihe River, middle reaches of the Yellow River, China. *Quaternary Science Reviews*. **2011**, *30*(3-4), 460-468. [doi:10.1016/j.quascirev.2010.12.007]
- Huisink, M. Changing river styles in response to Weichselian climate changes in the Vecht valley, eastern Netherlands. *Sedimentary Geology*. **2000**, *133*(1-2), 115-134. [doi:10.1016/S0037-0738(00)00030-0]
- Humboldt State University. Accuracy Metrics. Available online: http://gis.humboldt.edu/OLM/Courses/GSP_216_Online/lesson6-2/metrics.html (accessed on 29 August 2020).
- Iacobucci, G.; Troiani, F.; Milli, S.; Mazzanti, P.; Piacentini, D.; Zocchi, M.; Nadali, D. Combining Satellite Multispectral Imagery and Topographic Data for the Detection and Mapping of Fluvial Avulsion Processes in Lowland Areas. *Remote Sensing*. **2020**, *12*, 2243. [doi:10.3390/rs12142243]
- Ihlen, V.; Zanter, K. *Landsat 8 (L8) Data Users Handbook*; LDS-1574 Version 5.0; Department of the Interior, U.S. Geological Survey, 2019
- Jain, M.; Tandon, S.K. Fluvial response to Late Quaternary climate changes, western India. *Quaternary Science Reviews*. **2003**, *22*(20), 2223-2235. [doi:10.1016/S0277-3791(03)00137-9]
- JERS-1. eoPortal Directory. Available online: <https://earth.esa.int/web/eoportal/satellite-missions/j/jers-1> (accessed on 20 July 2020)
- Jones, L.S.; Schumm, S.A. Causes of avulsion: an overview. In *Fluvial Sedimentology VI*; Smith, N.D., Rogers, J., Eds.; Blackwells: Oxford, 1999; pp. 171-178
- Jones, M.D.; Roberts, N. Interpreting lake isotope records of Holocene environmental change in the Eastern Mediterranean. *Quaternary International*. **2008**, *181*(1), 32-38. [doi:10.1016/j.quaint.2007.01.012]
- Jotheri, J. Holocene Avulsion History of the Euphrates and Tigris Rivers in the Mesopotamian Floodplain. Ph.D. Thesis, Durham University, Durham, UK, June 2016
- Jotheri, J. Recognition criteria for canals and rivers in the Mesopotamian floodplain. In *Water Societies and Technologies from the Past and Present*, 1st ed.; Zhuang, Y., Altaweel, M., Eds.; UCL Press: London, UK, 2018; pp. 111–126. ISBN 978-1-911576-69-3
- Jotheri, J.; Allen, M.B.; Wilkinson, T.J. Holocene avulsions of the Euphrates river in the Najaf area of Western Mesopotamia: Impacts on human settlement patterns. *Geoarchaeology An International Journal*. **2016**, *31*, 175–193. [doi:10.1002/gea.21548]
- Jotheri, J.; Altaweel, M.; Tuji, A.; Anma, R.; Pennington, B.; Rost, S.; Watanabe, C. Holocene fluvial and anthropogenic processes in the region of Uruk in southern Mesopotamia. *Quaternary International*. **2018**, *483*, 57-69. [doi:10.1016/j.quaint.2017.11.037]
- Jotheri, J.; de Gruchy, M.W.; Almaliki, R.; Feadha, M. Remote sensing the archaeological traces of boat movement in the marshes of Southern Mesopotamia. *Remote Sensing*. **2019**, *11*, 2474. [doi:10.3390/rs11212474]

- Kadlec, J.; Kocurek, G.; Mohrig, D.; Shinde, D.P.; Murari, M.K.; Varma, V.; Stehlik, F.; Beneš, V.; Singhvi, A.K. Response of fluvial, aeolian, and lacustrine systems to late Pleistocene to Holocene climate change, Lower Moravian Basin, Czech Republic. *Geomorphology*. **2015**, *232*, 193-208. [doi:10.1016/j.geomorph.2014.12.030]
- Kahle, A.B.; Shumate, M.S.; Nash, D.B. Active airborne infrared laser system for identification of surface rock and minerals. *Geophysical Research Letters*. **1984**, *11(11)*, 1149–1152. [doi:10.1029/GL011i011p01149]
- Kaniewski, D.; Van Campo, E.; Guiot, J.; Le Burel, S.; Otto, T.; Beateaman, C. Environmental Roots of the Late Bronze Age Crisis. *PLoS ONE*. **2013**, *8(8)*, e71004. [doi:10.1371/journal.pone.0071004]
- Ke, Y.; Im, J.; Lee, J.; Gong, H.; Ryu, Y. Characteristics of Landsat 8 OLI-derived NDVI by comparison with multiple satellite sensors and in-situ observations. *Remote Sensing of Environment*. **2015**, *164*, 298-313. [doi:10.1016/j.rse.2015.04.004]
- Kennet, D.J.; Kennet, J.P. Influence of Holocene marine transgression and climate change on cultural evolution in southern Mesopotamia. In *Climate change and cultural dynamics. A Global Perspective on Mid-Holocene Transitions*, 1st ed.; Anderson, D.G., Maasch, K.A., Sandweiss, D.H., Eds.; Elsevier: London, UK, 2007; pp. 229-264
- Kennett, D.J.; Kennett, J.P. Early state formation in Southern Mesopotamia: Sea levels, shorelines, and climate change. *The Journal of Island and Coastal Archaeology*. **2006**, *1(1)*, 67–69. [doi:10.1080/15564890600586283]
- Kidder, T.R.; Liu, H. Bridging theoretical gaps in geoarchaeology: archaeology, geoarchaeology, and history in the Yellow River valley, China. *Archaeological and Anthropological Sciences*. **2017**, *9*, 1585-1602. [doi:10.1007/s12520-014-0184-5]
- Kleinans, M.G.; Ferguson, R.I.; Lane, S.N.; Hardy, R.J. Splitting rivers at their seams: bifurcations and avulsion. *Earth Surface Processes and Landforms*. **2013**, *38*, 47–61. [doi:10.1002/esp.3268]
- Kleiven, H.E.; Kissel, C.; Laj, C.; Ninnemann, U.S.; Richter, T.O.; Cortijo, E. Reduced North Atlantic Deep Water Coeval with the Glacial Lake Agassiz Freshwater Outburst. *Science*. **2008**, *316(5859)*, 60-64. [doi:10.1126/science.1148924]
- Knighton, D. *Fluvial Forms and Processes: A New Perspective*, 1st ed.; Hodder Education: London, UK, 1998
- Kuper, R.; Kröpelin, S. Climate-Controlled Holocene Occupation in the Sahara: Motor of Africa's Evolution. *Science*. **2006**, *313(5788)*, 803-807. [doi:10.1126/science.1130989]
- L3 Harris Geospatial. Calculate Confusion Matrices. Available online: <https://www.harrisgeospatial.com/docs/CalculatingConfusionMatrices.htm> (accessed on 29 August 2020)
- L3 Harris Geospatial. Classification. Available online: <https://www.harrisgeospatial.com/docs/Classification.html#ClassSupervised> (accessed on 19 August 2020)
- L3 Harris Geospatial. DEM Extraction from Radarsat-2 Data in SARscape. Available online: <https://www.l3harrisgeospatial.com/Support/Self-Help-Tools/Help-Articles/Help-Articles-Detail/ArtMID/10220/ArticleID/15704/DEM-Extraction-from-Radarsat-2-Data-in-SARscape> (accessed on 22 August 2020)
- L3 Harris Geospatial. Spectral Indices. Available online: <https://www.harrisgeospatial.com/docs/spectralindices.html> (accessed on 20 August 2020)
- L3 Harris Geospatial. Vegetation Indices Background. Available online: <https://www.harrisgeospatial.com/docs/backgroundvegetationindices.html> (accessed on 20 August 2020)
- Lambeck, K. Shoreline reconstructions for the Persian Gulf since the last glacial maximum. *Earth and Planetary Science Letters*. **1996**, *142(1-2)*, 43–57. [doi:10.1016/0012-821X(96)00069-6]
- Lawrence, D.; Philip, G.; Hunt, H.; Snape-Kennedy, L.; Wilkinson, T.J. Long Term Population, City Size and Climate Trends in the Fertile Crescent: A First Approximation. *PLoS ONE*. **2016**, *11(3)*, e0157863. [doi:10.1371/journal.pone.0157863]

- Leeder, M. *Sedimentology and Sedimentary Basins*. Wiley-Blackwell 2nd Edition: Oxford, 2011
- Leenman, A.; Eaton, B. Mechanisms for avulsion on alluvial fans: insights from high-frequency topographic data. *Earth Surface Processes and Landforms*. 2021. [doi:10.1002/esp.5059]
- Li, C.H.; Li, Y.X.; Zheng, Y.F.; Yu, S.Y.; Tang, L.Y.; Li, B.B.; Cui, Q.Y. A high-resolution pollen record from East China reveals large climate variability near the Northgrippian-Meghalayan boundary (around 4200 years ago) exerted societal influence. *Palaeogeography, Palaeoclimatology, Palaeoecology*. **2018**, *512*, 156-165. [doi:10.1016/j.palaeo.2018.07.031]
- Liu, J.G.; Mason, P.J. Image classification. In *Essential Image Processing and GIS for Remote Sensing*, 1st ed.; Wiley-Blackwell: Oxford, UK, 2009; pp. 91–103
- Ljung, K.; Björk, S.; Renssen, H.; Hammarlund, D. South Atlantic island record reveals a South Atlantic response to the 8.2 kyr event. *Climate of the Past*. **2008**, *4(1)*, 35-45. [doi:10.5194/cp-4-35-2008]
- Lombardi, N.; Lorusso, R.; Fasano, L.; Milillo, G. Interferometric COSMO-SkyMed© Spotlight DEM generation. In Proceedings of the 2016 IEEE International Geoscience and Remote Sensing Symposium (IGARSS), Beijing, China, 10–15 July 2016; pp. 6495-6498
- Macklin, M.G.; Jones, A.F.; Lewin, J. River response to rapid Holocene environmental change: evidence and explanation in British catchments. *Quaternary Science Reviews*. **2010**, *29(13-14)*, 1555-15-76. [doi:10.1016/j.quascirev.2009.06.010]
- Macklin, M.G.; Lewin, J. The rivers of civilization. *Quaternary Science Reviews*. **2015**, *114*, 228-244. [doi:10.1016/j.quascirev.2015.02.004]
- Macklin, M.G.; Lewin, J.; Woodward, J.C. The fluvial record of climate change. *Philosophical Transactions of the Royal Society A*. **2012**, *370*, 2143-2172. [doi:10.1098/rsta.2011.0608]
- Macklin, M.G.; Woodward, J.C.; Welsby, D.A.; Duller, G.A.T.; Williams, F.M.; Williams, M.A.J. Reach-scale river dynamics moderate the impact of rapid Holocene climate change on floodwater farming in the desert Nile. *Geology*. **2013**, *41(6)*, 965-698. [doi:10.1130/G34037.1]
- Magri, D.; Parra, I. Late Quaternary western Mediterranean pollen records and African winds. *Earth and Planetary Science Letters*. **2002**, *200(3-4)*, 401-408. [doi:10.1016/S0012-821X(02)00619-2]
- Mangerud, J.; Andersen, S.T.; Berglund, B.E.; Donner, J.J. Quaternary stratigraphy of Norden, a proposal for terminology and classification. *Boreas*. **1974**, *3(3)*, 109-127. [doi:10.1111/j.1502-3885.1974.tb00669.x]
- Mann, M. Large-scale Climate Variability and Connections with the Middle East in Past Centuries. *Climate Change*. **2002**, *55*, 287-314. [doi:10.1023/A:1020582910569]
- Manning, J.G.; Ludlow, F.; Stine, A.R.; Boos, W.R.; Sigl, M.; Marlon, J.R. Volcanic suppression of Nile summer flooding triggers revolt and constrains interstate conflict in ancient Egypt. *Nature Communications*. **2017**, *8*, 900. [doi:10.1038/s41467-017-00957-y]
- Mayer, L.; Menichetti, M.; Nesci, O.; Savelli, D. Morphotectonic approach to the drainage analysis in the North Marche region, central Italy. *Quaternary International*. **2003**, *101-102*, 157-167. [doi:10.1016/S1040-6182(02)00098-8]
- Menounos, B.; Clague, J.J.; Osborn, G.; Luckman, B.H.; Lakeman, T.R.; Minkus, R. Western Canadian glaciers advance in concert with climate change circa 4.2 ka. *Geophysical Research Letters*. **2008**, *35(7)*, L07501. [doi:10.1029/2008GL033172]
- Mercuri, A.M.; Sadori, L.; Uzquiano Ollero, P. Mediterranean and north-African cultural adaptations to mid-Holocene environmental and climatic changes. *The Holocene*. **2011**, *21(1)*, 189-206. [doi:10.1177/0959683610377532]
- Miall, A.D. *The Geology of Fluvial Deposits*, 4th ed.; Springer: Berlin/Heidelberg, Germany, 2006; pp. 172–176

- Millard, C.; Hajek, E.A.; Edmonds, D.A. Evaluating controls on crevasse-splay size: Implications for floodplain-basin filling. *Journal of Sedimentary Research*. **2017**, *87*, 722–739. [doi:10.2110/jsr.2017.40]
- Miller, J.R.; House, K.; Germanoski, D.; Tausch, R.J.; Chambers, J.C. Fluvial Geomorphic Responses to Holocene Climate Change. In: Great Basin Riparian Ecosystems. Ecology, Management and Restoration. Chambers, J.C., Miller, J.R., Eds.; Island Press, Washington, USA, 2004; pp. 49-87
- Milli, S.; Forti, L. Geology and palaeoenvironment of Nasiriyah area/southern Mesopotamia. In *Abu Tbeirah Excavations I. Area 1*, 1st ed.; Romano, L., D'Agostino, F., Eds.; Sapienza Università Editrice: Roma, Italy, 2019; pp. 19–33
- Mock, C.J. Paleoclimate. In *Encyclopedia of Quaternary Science*; Elias, S.A., Ed.; Elsevier: Amsterdam, The Netherlands, 2006; Volume 1, pp. 1867-1823
- Mohney, D. Terabytes From Space: Satellite Imaging is Filling Data Centers. Available online: <https://datacenterfrontier.com/terabytes-from-space-satellite-imaging-is-filling-data-centers/> (accessed on 25 September 2020)
- Morozova, G.S. A Review of Holocene Avulsions of the Tigris and Euphrates Rivers and Possible Effects on the Evolution of Civilizations in Lower Mesopotamia. *Geoarchaeology: An International Journal*. **2005**, *20(4)*, 401-423. [doi:10.1002/gea.20057]
- Mudd, S.M. Topographic data from satellites. In *Remote Sensing of Geomorphology*; Developments in Earth Surface Processes; Tarolli, P., Mudd, S.M., Eds.; Elsevier: Amsterdam, The Netherlands, 2020; Volume 23, pp. 91–128
- NASA and METI Science Team. NASA EARTHDATA. Available online: <https://lpdaac.usgs.gov/news/nasa-and-meti-release-aster-global-dem-version-3/> (Accessed on 5 August 2020)
- NASA Earth Observatory. World of change: Mesopotamia Marshes. Available online: <https://earthobservatory.nasa.gov/world-of-change/Iraq> (accessed on 18 August 2020)
- Nesci, O.; Savelli, D.; Troiani, F. Types and development of stream terraces in the Marche Apennines (central Italy): a review and remarks on recent appraisals. *Géomorphologie: relief, processus, environment*. **2012**, *2*, 215-238. [doi:10.4000/geomorphologie.9838]
- New Version of the ASTER GDEM. Available online: <https://earthdata.nasa.gov/learn/articles/new-aster-gdem> (accessed on 05 August 2020)
- Nienhuis, J.H.; Törnqvist, T.E.; Esposito, C.R. Crevasse splays versus avulsions: a recipe for land building with levee breaches. *Geophysical Research Letters*. **2018**, *45(9)*, 4058-4067. [doi:10.1029/2018GL077933]
- NOAA National Centers for Environmental Information. North Atlantic Oscillation (NOA). Available online: <https://www.ncdc.noaa.gov/teleconnections/nao/> (accessed on 13 August 2020)
- Olariu, C.; Bhattacharya, J.P. Terminal distributary channels and delta front architecture of river-dominated delta systems. *Journal of Sedimentary Research*. **2006**, *76*, 212-233. [doi:10.2110/jsr.2006.026]
- Overbank Deposits - Available online: <https://www.nationalgeographic.org/encyclopedia/overbank-deposits/> (accessed on 21 January 2021)
- Palmisano, A.; Lawrence, D.; de Gruchy, M.W.; Bevan, A.; Shennan, S. Holocene regional population dynamics and climatic trends in the Near East: A first comparison using archaeo-demographic proxies. *Quaternary Science Reviews*. **2021**, *252*, 106739. [doi:10.1016/j.quascirev.2020.106739]
- Palmisano, A.; Woodbridge, J.; Roberts, N.; Bevan, A.; Fyfe, R.; Shennan, S.; Cheddadi, R.; Greenberg, R.; Kaniewsky, D.; Langgut, D.; et al. Holocene landscape dynamics and long-term population trends in the Levant. *The Holocene*. **2019**, *29(5)*, 708-727. [doi:10.1177/0959683619826642]

- Pearce, R. How satellites are used to monitor climate change. Available online: <https://www.carbonbrief.org/interactive-satellites-used-monitor-climate-change> (accessed on 25 September 2020)
- Penck, A.; Brückner, E. *Die Alpen im Eiszeitalter*. Tauchnitz, Leipzig; 1909
- Pontius, R.G., Jr.; Millones, M. Death to Kappa: Birth of quantity disagreement and allocation disagreement for accuracy assessment. *International Journal of Remote Sensing*. **2011**, *32*, 4407–4429. [doi:10.1080/01431161.2011.552923]
- Rateb, A.; Scanlon, B.R.; Kuo, C. Multi-decadal assessment of water budget and hydrological extremes in the Tigris-Euphrates Basin using satellites, modelling, and in-situ data. *Science of The Total Environment*. **2021**, *766*, 144337. [doi:10.1016/j.scitotenv.2020.144337]
- Rice, J.A.; Simms, A.R.; Buzas-Stephens, P.; Steel, E.; Livsey, D.; Reynolds, L.C.; Yokoyama, Y.; Halihan, T. Deltaic response to climate change: The Holocene history of the Nueces Delta. *Global and Planetary Change*. **2020**, *191*, 103213. [doi:10.1016/j.gloplacha.2020.103213]
- Richards, J.A.; Jia, X. Sources and Characteristics of Remote Sensing Image Data. In *Remote Sensing Digital Image Analysis. An Introduction*. 4th ed.; Richards, J.A., Jia, X., Eds.; Springer: Berlin, Germany, 2006; pp. 1-25
- Roberts, N. Boon or curse? Climate change and its consequences for the Mediterranean civilizations. Webinar presented during the #DSTNonSiFerma seminars of the Dipartimento di Scienze della Terra - Università di Pisa, June 18th, 2020
- Roberts, N. *The Holocene. An Environmental History*, 3rd ed.; Wiley-Blackweel: Oxford, UK, 2014
- Roberts, N.; Eastwood, W.J.; Kuzucuoglu, C.; Fiorentino, G.; Caracuta, V. Climatic, vegetation and cultural change in the eastern Mediterranean during the mid-Holocene environmental transition. *The Holocene*. **2011**, *21(1)*, 147-162. [doi:10.1177/0959683610386819]
- Rost, S. Water management in Mesopotamia from the sixth till the first millennium B.C. *Wires Water*. **2017**, *4(5)*, e1230. [doi:10.1002/wat2.1230]
- Roy, D.P.; Wulder, M.A.; Loveland, T.R.; Woodcock, E.; Allen, R.G.; Anderson, M.C.; Helder, D.; Irons, J.R.; Johnson, D.M.; Kennedy, R.; et al. Landsat-8: Science and product vision for terrestrial global change research. *Remote Sensing of Environmental*. **2014**, *145*, 154–172. [doi:10.1016/j.rse.2014.02.001]
- Russel, J.; Talbot, M.R.; Haskell, B.J. Mid-holocene climate change in Lake Bosumtwi, Ghana. *Quaternary Research*. **2003**, *60(2)*, 133-141. [doi:10.1016/S0033-5894(03)00065-6]
- Sadori, L.; Giraudi, C.; Masi, A.; Magny, M.; Ortu, E., Zanchetta, G., Izdebski, A. Climate, environment and society in southern Italy during the last 2000 years. A review of the environmental, historical and archaeological evidence. *Quaternary Science Reviews*. **2016**, *136*, 173-188. [doi:10.1016/j.quascirev.2015.09.020]
- Santillan, J.R.; Makinano-Santillan, M.; Makinano, R.M. Vertical accuracy assessment of ALOS World 3D-30M Digital Elevation Model over northeastern Mindanao, Philippines. In Proceedings of the 2016 IEEE International Geoscience and Remote Sensing Symposium (IGARSS), Beijing, China, 10–15 July 2016; pp. 5374–5377
- Sarkar, A.; Mukherjee, A.D.; Bera, M.K.; Das, B.; Juyal, N.; Morthekai, P.; Deshpande, R.D.; Shinde, V.S.; Rao, L.S. Oxygen isotope in archaeological bioapatites from India: Implications to climate change and decline of Bronze Age Harappan civilization. *Scientific Reports*. **2016**, *6*, 26555. [doi:10.1038/srep26555]
- SARmap. Getting started with SARscape for Windows. Available online: http://www.sarmap.ch/tutorials/Getting_started.pdf (accessed on 22 August 2020)
- SARscape. User Guide. Available online: https://www.harrisgeospatial.com/docs/pdf/sarscape_5.1_help.pdf (accessed on 22 August 2020)

- Schumm, S.A. Evolution and response to the fluvial system, sedimentologic implications. In *Recent and Ancient Nonmarine Environments: Models for Exploration*, SEPM Special Publication 31, Ethridge, F.G., Flores, R.M., Eds.; 1981, pp. 19-29
- Schumm, S.A. Quaternary palaeohydrology. In *The Quaternary of the United States*; Wright, H.E., Frey, D.G., Eds; Princeton University Press: Princeton, New Jersey, USA, 1965; pp. 783-794
- Sekandari, M.; Masoumi, I.; Pour, A.B.; Muslim, A.M.; Rahmani, O.; Hashim, M.; Zoheir, B.; Pradhan, B.; Misra, A.; Aminpour, S.M. Application of Landsat-8, Sentinel-2, ASTER and WorldView-3 spectral imagery for exploration of carbonate-hosted Pb-Zn deposits in the CENTRAL IRANIAN TERRANE (CIT). *Remote Sensing*. **2020**, *12*(8), 1239. [doi:10.3390/rs12081239]
- Selli, R. Il Bacino del Metauro. *Giornale di Geologia*. **1954**, *24*, 1-268.
- Sepehr, M.; Cosgrove, J.W. Structural framework of the Zagros Fold–Thrust Belt, Iran. *Marine and Petroleum Geology*. **2004**, *21*(7), 829-843. [doi:10.1016/j.marpetgeo.2003.07.006]
- Shackelton, N. Oxygen Isotope Analyses and Pleistocene Temperatures Re-assessed. *Nature*. **1967**, *215*, 15-17. [doi:10.1038/215015a0]
- Sissakian, V.K. Geological evolution of the Iraqi Mesopotamia Foredeep, inner platform and near surroundings of the Arabian Plate. *Journal of Asian Earth Sciences*. **2013**, *72*, 152-163. [doi:10.1016/j.jseaes.2012.09.032]
- Sissakian, V.K.; Al-Ansari, N.; Adamo, N.; Al-Azzawi, M.K.; Abdullah, M.; Laue, J. Geomorphology of the Mesopotamian Plain: A Critical Review. *Journal of Earth Sciences and Geotechnical Engineering*. **2020(a)**, *10*(4), 1-25
- Sissakian, V.K.; Al-Ansari, N.; Adamo, N.; Al-Azzawi, M.K.; Abdullah, M.; Laue, J. Stratigraphy of the Mesopotamian Plain: A Critical Review. *Journal of Earth Sciences and Geotechnical Engineering*. **2020(b)**, *10*(4), 27-56
- Slingerland, R.L.; Smith, N.D. River avulsions and their deposits. *Annual Review of Earth and Planetary Sciences*. **2004**, *32*, 255–283. [doi:10.1146/annurev.earth.32.101802.120201]
- Smith, N.D.; Cross, T.A.; Dufficy, J.P.; Clough, S.R. Anatomy of an avulsion. *Sedimentology*. **1989**, *36*, 1–23. [doi:10.1111/j.1365-3091.1989.tb00817.x]
- Smith, N.D.; Pérez-Arlucea, M. Fine-grained splay deposition in the avulsion belt of the lower Saskatchewan River, Canada. *Journal of Sedimentary Research*. **1994**, *64*, 159–168. [doi:10.1306/D4267F7D-2B26-11D7-8648000102C1865D]
- Stauwbasser, M.; Sirocko, F.; Grootes, P.M.; Segl, M. Climate change at the 4.2 ka BP termination of the Indus valley civilization and Holocene south Asian monsoon variability. *Geophysical Research Letters*. **2003**, *30*(8), 1425. [doi:10.1029/2002GL016822]
- Stevens, L.R.; Ito, E.; Schwalb, A.; Wright Jr., H.E. Timing of atmospheric precipitation in the Zagros Mountains inferred from a multi-proxy record from Lake Mirabad, Iran. *Quaternary Research*. **2006**, *66*(3), 494-500. [doi:10.1016/j.yqres.2006.06.008]
- Stevens, L.R.; Wright, H.E.; Ito, E. Proposed changes in seasonality of climate during the Lateglacial and Holocene at Lake Zeribar, Iran. *The Holocene*. **2001**, *11*(6), 747-755. [doi:10.1191/09596830195762]
- Syvitski, J.M.P.; Overeem, I.; Brakenridge, G.R.; Hannon, M. Floods, floodplains, delta plains — A satellite imaging approach. *Sedimentary Geology*. **2012**, *267-268*, 1-14. [doi:10.1016/j.sedgeo.2012.05.014]
- Tachikawa, T.; Kaku, M.; Iwasaki, A.; Gesch, D.; Oimoen, M.; Zhang, Z.; Danielson, J.; Krieger, T.; Curtis, B.; Haase, J.; et al. ASTER Global Digital Elevation Model Version 2—Summary of Validation Results. Available online: https://ssl.jspacesystems.or.jp/ersdac/GDEM/ver2Validation/Summary_GDEM2_validation_report_final.pdf (accessed on 19 April 2020)

- Talebi, T.; Ramezani, E.; Djamali, M.; Lahijani, H.A.K.; Naqinezhad, A.; Alizadeh, K.; Andrieu-Ponel, V. The Late-Holocene climate change, vegetation dynamics, lake-level changes and anthropogenic impacts in the Lake Urmia region, NW Iran. *Quaternary International*. **2016**, *408*, 40-51. [doi:10.1016/j.quaint.2015.11.070]
- Tebbens, L.A.; Veldkamp, A.; Westerhoff, W.; Kroonenberg, S.B. Fluvial incision and channel downcutting as a response to Late-glacial and Early Holocene climate change: the lower reach of the River Meuse (Maas), The Netherlands. *Journal of Quaternary Science*. **1999**, *14*(1), 59-75. [doi:10.1002/(SICI)1099-1417(199902)14:1<59::AID-JQS408>3.0.CO;2-Z]
- Teller, J.T.; Glennie, K.W.; Lancaster, N.; Singhvi, A.K. Calcareous dunes of the United Arab Emirates and Noah's Flood: the postglacial reflooding of the Persian (Arabian) Gulf. *Quaternary International*. **2000**, *68-71*, 297-308. [doi:10.1016/S1040-6182(00)00052-5]
- Terra Mission. eoPortal Directory. Available online: <https://directory.eoportal.org/web/eoportal/satellite-missions/t/terra#sensors> (accessed on 05 August 2020)
- TERRA. The EOS Flagship. Available online: <https://terra.nasa.gov/about/terra-instruments/aster> (accessed on 05 August 2020)
- The Marshlands of Iraq Inscribed on UNESCO's World Heritage List. Available online: <http://www.unesco.org/new/en/member-states/single-view/news/the-marshlands-of-iraq-inscribed-on-unescos-world-heritag/> (accessed on 18 August 2020)
- Thompson, L.G.; Mosley-Thompson, E.; Davis, M.E.; Henderson, K.A.; Brecher, H.H.; Zagorodnov, V.S.; Mashiotta, T.A.; Lin, P.; Makhlenko, V.N.; Douglas, R.H.; et al. Kilimanjaro Ice Core Records: Evidence of Holocene Climate Change in Tropical Africa. *Science*. **2002**, *298*(5593), 589-593. [doi:10.1126/science.1073198]
- Törnqvist, T.E. Responses to Rapid Environmental Change. In *Encyclopedia of Quaternary Science*; Elias, S.A., Ed; Elsevier: Amsterdam, The Netherlands, 2006; Volume 1, pp. 686-694
- Troiani, F.; Della Seta, M. Geomorphological response of fluvial and coastal terraces to Quaternary tectonics and climate as revealed by geostatistical topographic analysis. *Earth Surface Processes and Landforms*. **2011**, *36*, 1193-1208. [doi:10.1002/esp.2145]
- Troiani, F.; Della Seta, M. The use of the Stream Length-Gradient Index in morphotectonic analysis of small catchments: a case study from central Italy. *Geomorphology*. **2008**, *102*, 159-168. [doi:10.1016/j.geomorph.2007.06.020]
- UNESCO. The Ahwar of Southern Iraq: Refuge of Biodiversity and the Relict Landscape of the Mesopotamian Cities. Available online: <https://whc.unesco.org/en/list/1481/> (accessed on 10 August 2020)
- Urey, H.C. Oxygen Isotopes in Nature and in the Laboratory. *Science*. **1948**, *108*(2810), 489-496. [doi:10.1126/science.108.2810.489]
- USGS Landsat Missions. Available online: <https://www.usgs.gov/land-resources/nli/landsat/landsat-8?qtscience-support-page-related-con=0#qt-science-support-page-related-con> (accessed on 20 May 2020).
- Van Tooreneburg, K.A.; Donselaar, M.E.; Weltje, G.J. The life cycle of crevasse splays as a key mechanism in the aggradation of alluvial ridges and river avulsion. *Earth Surface Processes and Landforms*. **2018**, *43*, 2409-2420. [doi:10.1002/esp.4404]
- Verheyden, S.; Nader, F.H.; Cheng, H.J.; Edwards, L.R.; Swennen, R. Paleoclimate reconstruction in the Levant region from the geochemistry of a Holocene stalagmite from the Jeita cave, Lebanon. *Quaternary Research*. **2008**, *70*(3), 368-381. [doi:10.1016/j.yqres.2008.05.004]
- Verhoeven, K. Geomorphological Research in the Mesopotamian Flood Plain. In *Changing Watercourses in Babylonia. Towards a Reconstruction of the Ancient Environment in Lower Mesopotamia, Vol. I*, Gasche, H., Tanret, M., Eds.; University of Chicago Press: Chicago, USA, 1998; pp. 159-245

- Von Suchodoletz, H.; Faust, D. Late Quaternary fluvial dynamics and landscape evolution at the lower Shulaveris Ghele River (southern Caucasus). *Quaternary Research*. **2018**, *89(1)*, 254-269. [doi:10.1017/qua.2017.80]
- Von Suchodoletz, H.; Menz, M.; Kühn, P.; Sukhishvili, L.; Faust, D. Fluvial sediments of the Algeti River in southeastern Georgia — An archive of Late Quaternary landscape activity and stability in the Transcaucasian region. *Catena*. **2015**, *130*, 95-107. [doi:10.1016/j.catena.2014.06.019]
- Walker, M.; Head, M.J.; Berkelhammer, M.; Björck, S.; Cheng, H.; Cwynar, L.; Fisher, D.; Gkinis, V.; Long, A.; Lowe, J.; et al. Formal ratification of the subdivision of the Holocene Series/Epoch (Quaternary System/Period): two new Global Boundary Stratotype Sections and Points (GSSPs) and three new stages/subseries. *Episodes*. **2018**, *41(4)*, 213-223. [doi:10.18814/epiugs/2018/018016]
- Walker, M.J.C.; Berkelhammer, M.; Björck, S.; Cwynar, L.C.; Fisher, D.A.; Long, A.J.; Lowe, J.J.; Newnham, R.M.; Rasmussen, S.O.; Weiss, H. Formal subdivision of the Holocene Series/Epoch: a Discussion Paper by a Working Group of INTIMATE (Integration of ice-core, marine and terrestrial records) and the Subcommittee on Quaternary Stratigraphy (International Commission on Stratigraphy). *Journal of Quaternary Science*. **2012**, *27(7)*, 649-659. [doi:10.1002/jqs.2565]
- Wanner, H.; Beer, J.; Bütikofer, J.; Crowley, T.J.; Cubasch, U.; Flückiger, J.; Goosse, H.; Grosjean, M.; Joos, F.; Kaplan, J.O.; et al. Mid- to Late Holocene climate change: an overview. *Quaternary Science Reviews*. **2008**, *27*, 1791-1828. [doi:10.1016/j.quascirev.2008.06.013]
- Wasylikowa, K.; Witkowski, A.; Walanus, A.; Hutorowicz, A.; Alexandrowicz, S.W.; Langer, J.J. Palaeolimnology of Lake Zeribar, Iran, and its climatic implications. *Quaternary Research*. **2006**, *66(3)*, 477-493. [doi:10.1016/j.yqres.2006.06.006]
- Waterman, R. What's new in World Imagery (June 2020). Available online: <https://www.esri.com/arcgis-blog/products/arcgis-living-atlas/mapping/whats-new-in-world-imagery-june-2020/> (accessed on 10 September 2020)
- Waterman, R. What's New in World Imagery Basemap (July 2017 through June 2018). Available online: <https://www.esri.com/arcgis-blog/products/arcgis-living-atlas/imagery/whats-new-in-world-imagery-basemap-july-2017-through-june-2018/> (accessed on 13 August 2020)
- Weiss, H. Global megadrought, societal collapse and resilience at 4.2-3.9 ka BP across the Mediterranean and west Asia. *PAGES Magazine*. **2016**, *24(2)*, 62-63. [doi:10.22498/pages.24.2.62]
- Weiss, H. The Northern Levant during the Intermediate Bronze Age: altered trajectories. In *The Oxford Handbook of the Archaeology of the Levant: c. 8000–332 BCE*. Steiner, M.L., Killebrew, A.E., Eds.; Oxford University Press: Oxford, UK, 2013; pp. 367–387
- Wick, L.; Lemcke, G.; Sturm, M. Evidence of Lateglacial and Holocene climatic change and human impact in eastern Anatolia: high-resolution pollen, charcoal, isotopic and geochemical records from the laminated sediments of Lake Van, Turkey. *The Holocene*. **2003**, *13(5)*, 665-675. [doi:10.1191/0959683603hl653rp]
- Wiener, M.H. The interaction of climate change and agency in the collapse of civilizations ca. 2300–2000 BC. *Radiocarbon*. **2014**, *56(4)*, S1-S16. [doi:10.2458/azu_rc.56.18325]
- Wilkinson, T.J.; Philip, G.; Bradbury, J.; Dunford, R.; Donoghue, D.; Galiatsatos, N.; Lawrence, D.; Ricci, A.; Smith, S.L. Contextualizing Early Urbanization: Settlement Cores, Early States and Agro-pastoral Strategies in the Fertile Crescent During the Fourth and Third Millennia BC. *Journal of World Prehistory*. **2014**, *27*, 43-109. [doi:10.1007/s10963-014-9072-2]
- Wilkinson, T.J.; Rayne, L.; Jotheri, J. Hydraulic landscapes in Mesopotamia: the role of human niche construction. *Water History*. **2015**, *7*, 397-418. [doi:10.1007/s12685-015-0127-9]

- Xiao, J.; Zhang, S.; Fan, J.; Wen, R.; Xu, Q.; Inouchi, Y.; Nakamura, T. The 4.2 ka event and its resulting cultural interruption in the Daihai Lake basin at the East Asian summer monsoon margin. *Quaternary International*. **2019**, 527, 87-93. [doi:10.1016/j.quaint.2018.06.025]
- Yacoub, S.Y. Geomorphology of the Mesopotamia plain. *Iraqi Bulletin of Geology and Mining*. **2011**, 4, 7–32
- Yang, T.-N.; Lee, T.-Q.; Meyers, P. A.; Song, S.-R.; Kao, S.-J.; Löwemark, L.; Chen, R.-F.; Chen, H.-F.; Wei, K.-Y.; Fan, C.-W.; et al. Variations in monsoonal rainfall over the last 21 kyr inferred from sedimentary organic matter in Tung-Yuan Pond, southern Taiwan. *Quaternary Science Reviews*. **2011**, 30(23-24), 3413-3422. [doi:10.1016/j.quascirev.2011.08.017]
- Yuill, B.T.; Khadka, A.K.; Pereira, J.; Allison, M.A.; Meselhe, E.A. Morphodynamics of the erosional phase of crevasse-splay evolution and implications for river sediment diversion function. *Geomorphology*. **2016**, 259, 12–29. [doi:10.1016/j.geomorph.2016.02.005]
- Zanchetta, G.; Bar-Matthews, M.; Drysdale, R.N.; Lionello, P.; Ayalon, A.; Hellstorm, J.C.; Isola, I.; Regattieri, E. Coeval dry events in the central and eastern Mediterranean basin at 5.2 and 5.6 ka recorded in Corchia (Italy) and Soreq caves (Israel) speleothems. *Global and Planetary Change*. **2014**, 122, 130-139. [doi:10.1016/j.gloplacha.2014.07.013]
- Zhang, D.; Chen, X.; Li, Y.; Zhang, S. Holocene vegetation dynamics and associated climate changes in the Altai Mountains of the Arid Central Asia. *Palaeogeography, Palaeoclimatology, Palaeoecology*. **2020**, 550, 1097447. [doi:10.1016/j.palaeo.2020.109744]
- Zhao, X.; Thomas, I.; Salem, A.; Alassal, S.E.; Liu, Y.; Sun, Q.; Chen, J.; Ma, F.; Finlayson, B.; Chen, Z. Holocene climate change and its influence on early agriculture in the Nile Delta, Egypt. *Palaeogeography, Palaeoclimatology, Palaeoecology*. **2020**, 547, 109702. [doi:10.1016/j.palaeo.2020.109702]
- Zielhofer, C.; Bussmann, J.; Ibouhouten, H.; Fenech, K. Flood frequencies reveal Holocene rapid climate changes (Lower Moulouya River, northeastern Morocco). *Journal of Quaternary Science*. **2010**, 25(5), 700-714. [doi:10.1002/jqs.1347]
- Zielhofer, C.; Faust, D.; Linstädter, J. Late Pleistocene and Holocene alluvial archives in the Southwestern Mediterranean: Changes in fluvial dynamics and past human response. *Quaternary International*. **2008**, 181, 39-54. [doi:10.1016/j.quaint.2007.09.016]